NUMERICAL MODELLING OF TIME-DEPENDENT NEGATIVE SKIN FRICTION ON SINGLE PILE AND PILE GROUP IN SOFT SOILS

LIANG RUI

PhD

The Hong Kong Polytechnic University

2025

The Hong Kong Polytechnic University

Department of Civil and Environmental Engineering

Numerical modelling of time-dependent negative skin friction on single pile and pile group in soft soils

LIANG Rui

A thesis submitted in partial fulfilment of the requirements for the degree
of Doctor of Philosophy

March 2025

CERTIFICATE OF ORIGINALITY

I hereby declare that this thesis is my own work and that, to the best of my knowledge and belief, it reproduces no material previously published or written, nor material that has been accepted for the award of any other degree or diploma, except where due acknowledgement has been made in the text.

____________________________(Signed)

_________LIANG Rui_________(Name of student)

To my family for their love and support

ABSTRACT

Over the past few decades, increasingly taller and larger structures have been constructed, making piles a crucial foundation solution. However, the adoption of pile foundations in consolidating soil can pose significant design challenges, particularly the mobilization of the negative skin friction (NSF). NSF induces additional axial forces on the pile, imposing a detrimental rather than a beneficial load. While empirical methods derived from field observations for estimating NSF can be applied in preliminary foundation design, some design codes remain overly simplistic. Moreover, the creep effect on NSF is often ignored in these design methods. The soft soil creep effect on the long-term development of NSF has remained poorly understood. This thesis aims to incorporate the elasto-viscoplastic model into the NSF analysis using the rigorous finite element method (FEM) for both single pile and pile groups, providing insights into current design methods while refining them through parametric studies.

In this study, the two-dimensional axisymmetric single pile-soil interaction model is first established and calculated to examine various degrees of creep effects on the variation of NSF and neutral plane (NP) during and after the primary consolidation periods. According to the findings, a high creep coefficient of the soil results in an increase in NSF and a descending trend of the NP. The creep induced delay of NSF is observed attributed to the increase in excess pore pressure during the early stage of consolidation. The NP position varies drastically at the commencement of consolidation when taking creep into consideration. An exponential prediction model to reflect the time dependence of the location of the NP is proposed.

Subsequently, numerical investigations further extend to three-dimensional analysis, validated through centrifuge tests, are conducted to examine the effect of sacrificial piles on the dragload reduction in the center pile (termed as group effect) at varying pile spacings. A parametric investigation is conducted to quantify the group effect under different variables, including pile spacing, end-bearing layer stiffness and creep coefficient. Results reveal that beyond the spacing of 7 d (where d is the diameter of sacrificial piles), the group effect can be neglected. Furthermore, the group effect is highly dependent on the site-specific creep behavior, becoming less significant under high creep conditions. The reduction in effective stress of soil within a pile group is identified as the primary cause of the NSF pile group effect.

Pile penetration in soft ground involves complex mechanisms, including significant alterations to the surrounding soil state, which influence NSF over time. However, pile penetration is often excluded from finite element analysis. The impact of pile penetration on the NSF generation is thus analyzed. A novel stable node-based smoothed particle finite element method (SNS-PFEM) framework is introduced for two-dimensional axisymmetric conditions and coupled consolidation, incorporating the ANICREEP model for soft soil with a modified cutting-plane algorithm. A field case study with penetration process is simulated to verify the numerical model's performance, followed by a parametric analysis on the effect of penetration rate on NSF during consolidation. Results indicate that excluding pile penetration from NSF analysis can result in an unsafe underestimation of NSF and dragload magnitudes. The penetration rate affects dragload only at the initial consolidation stage. As consolidation progresses, dragload converges to nearly the same magnitude across different rates. Additionally, current design methods inadequately predict the β value (where β is an empirical factor correlating vertical effective stress of soil with the pile skin friction) and its time dependency, for which a new empirical formula for the time-dependent β value is proposed and successfully applied to other field cases.

Finally, conclusions are drawn, and future work is outlined.

LIST OF PUBLICATIONS

Journal articles

Liang, R., Yin, Z. Y., Yin, J. H., Wu, P. C., and Chen, Z. J. (2025). Numerical Assessment of Negative Skin Friction on Pile Groups in Soft Ground. *Computers and Geotechnics,* 187, 107450.

Liang, R., Yin, Z. Y., Wu, P. C., Chen, Z. J., and Yin, J. H. (2025). Numerical Assessment of Negative Skin Friction on Piles in Soft Soils Considering Pile Penetration Effects. *Computers and Geotechnics*, 185, 107315.

Liang, R., Yin, Z. Y., Yin, J. H., Wu, P. C., and Chen, Z. J. (2024). An Enhanced Micromechanical Rock–pile Interface Model with Application to Rock socketed Pile Modeling. *International Journal for Numerical and Analytical Methods in Geomechanics*. 48(11), 2971-2995.

Liang, R., Yin, Z. Y., Yin, J. H., and Wu, P. C. (2023). Numerical Analysis of Time-dependent Negative Skin Friction on Pile in Soft Soils. *Computers and Geotechnics*, 155, 105218.

ACKNOWLEDGMENTS

This thesis would not have been possible without the support of numerous individuals. First and foremost, I extend my deepest gratitude to my supervisors, Prof. Jian-Hua YIN and Prof. Zhen-Yu YIN, for their invaluable guidance and encouragement. Their meticulous reviews of my thesis and research papers have greatly enhanced my academic development. Over the past three years, Prof. YIN has consistently provided insightful advice, for which I am sincerely grateful. I also wish to express my profound respect to Prof. Run LIU of Tianjin University, whose mentorship and selfless help during my master's studies inspired my pursuit of academia. I am grateful to my thesis examiners, Prof. Li-Min ZHANG and Dr. Ying-Hui TIAN, as well as the chair of BoE, Prof. Chao ZHOU, for their valuable feedback and constructive suggestions.

I sincerely appreciate Prof. Dao-Yuan TAN, Prof. Wen-Bo CHEN, Prof. Kai LIU, Dr. Pei-Chen WU, Dr. Ze-Jian CHEN, Dr. Ding-Bao SONG for their generous support within Prof. YIN’s big group. I am also grateful to Dr. Huang-Cheng FANG and Dr. Mao-Zhu PENG for their invaluable guidance on constitutive modeling and finite element method. I extend my gratitude to my colleagues in ZS960, Mr. Shao-Jie LIU, Mr. Min-Hao ZHANG, Dr. Yu ZHANG and Mr. Xian-Han WU, for their friendship.

I am deeply grateful to my parents and family for their support and encouragement. Words cannot fully convey my appreciation for their endless care. Finally, I extend my heartfelt thanks to Laura for her love and patience during a very demanding period for me.

CONTENTS

LIST OF FIGURES

LIST OF TABLES

CHAPTER 1 INTRODUCTION

1.1 Overview and background

Hong Kong is a coastal city with limited flat land, where land is considered as precious as gold. To accommodate the growing housing and economic demands, large marine reclamation has been undertaken since the 1980s, particularly in areas with soft soil such as Hong Kong marine deposits (HKMD). Many tall buildings in Hong Kong are supported by piles installed through recently or newly reclaimed soils and founded on or into rock mass (some on stiff soils), as seen in past reclamation projects in Tseung Kwan O and Ma On Shan. In new marine reclamation areas, such as “Tung Chung New Town Extension” (130 hectares for 144,000 people), the majority of piles will be installed through fills and settling marine soils into rock-sockets, with a small portion in stiff soils, to support nearly all tall buildings. Normally, the positive skin friction (PSF) along the pile, combined with the pile toe resistance, supports the load imposed by the superstructure. However, the time-dependent compression of the soft soils including creep may lead to substantial settlement, as reported by several scholars (Jiang and Lin 2010, Feng 2016, Wu et al. 2020, Chen et al. 2021). This excessive downward movement of the soil relative to the pile changes the shear force direction at the pile-soil interface, inducing the negative skin friction (NSF), which acts in the same direction as gravity. The foundational terms related to NSF, as defined by Fellenius (1972, 1989, 1998), are as follows:

(a) Negative Skin Friction (NSF): The downward-acting soil resistance along the pile shaft resulting from downdrag, which induces compression in the pile.

(b) Downdrag: The downward movement of a deep foundation unit caused by NSF, typically expressed in terms of settlement.

(c) Dragload: The load transferred to a deep foundation unit due to NSF.

(d) Neutral plane (NP) or refer to neutral point: The position where the pile and surrounding soil move equally. This point serves as the boundary between positive and negative skin friction, and is where the axial force in the pile reaches its maximum. As for the end-bearing pile, the NP is generally located near the pile toe.

The dragload is regarded as a detrimental load that reduces the pile's axial capacity and is likely to exceed the pile's structural strength (Poulos 1997). Furthermore, NSF can lead to excessive downdrag settlement due to axial shortening and additional pile penetration on account of the increased axial load, severely compromising the serviceability of the superstructure.

Both long-term field test schemes and small-scale model tests have been conducted on the development of dragload and downdrag of piles and the results show that the NSF can generally be caused by four main factors: surcharge loading over soft soil deposits (Johannessen and Bjerrum 1965, Bjerrum et al. 1969, Fellenius 1972, Okabe 1977, Clemente 1981, Leung et al. 1991, Indraratna et al. 1992, Premchitt et al. 1994, Hong et al. 2015, Zhang et al. 2022); lowering of the groundwater table, which causes ground subsidence (Endo et al. 1969, Inoue 1977, Yen et al. 1989, Lee et al. 1998); soil re-consolidation after pile driving, which generates significant excess porewater pressure (Fellenius 1972); and pile foundations in collapsible loess areas, such as the Loess Plateau in China (Zhao et al. 2022). Furthermore, the results showed that during consolidation, the change of the effective stress of the soils governs the load transfer from the soil to the pile, thereby controlling the magnitude of the dragload, downdrag as well as the position of the neutral plane. In addition, only a few millimeters of relative displacement are needed to fully mobilize the skin friction in both negative and positive directions.

In addition, numerical simulations have been conducted using various soil constitutive models (Lee et al. 2002, Ng et al. 2008, Lam et al. 2009, 2013, Liu et al. 2012, Yan et al. 2012, Sun et al. 2015, Chiou and Wei 2021, Zhao et al. 2022) and pile-soil interface models (Alonso et al. 1984, Jeong et al. 2004, Chen et al. 2009, Yan et al. 2012, Cao et al. 2014) to study the NSF on piles. Chen et al. (2009) developed a hyperbolic interface model and investigated the distribution of the NSF and axial force considering the nonlinear consolidation. Yan et al. (2012) proposed a modified algorithm in subroutine which can consider the effect of excess pore pressure in the pile-soil interface behavior. Chiou and Wei (2021) used the modified Cam Clay model to simulate soft soil and verified their findings by field test results. The influence of pile head loading, surcharge pressure and different types of bearing layers on the dragload were analyzed properly.

Although the consolidation of soft soil has been considered in simulations of the time-dependent development of the dragload, the existing literature has overall neglected the viscous behavior of soft soil, such as creep. Nevertheless, the creep deformation of clay is intrinsic to soft soils and should be considered in engineering design (Yin and Graham 1994, Yin and Zhu 1999, Chen et al. 2021). Creep induced settlements can influence the development of dragload, especially over the entire course of design life, for example, 50 years (HKIE 2017). Notably, even assuming that the settlement due to creep accounts for a small percentage of the total settlement, it should be noted that only a few millimeters could fully mobilize the NSF as mentioned earlier. Furthermore, the creep deformation may also generate excess pore pressure (Yin and Graham 1994, Yin and Zhu 1999), influencing the load transfer from the soil to the pile. The creep effect on the development of dragload and the location of the NP is not fully understood, and research on the magnitude of dragload after long-term consolidation remains limited.

In practice, applying a thin coat of bitumen, approximately 1-2 mm thick, can reduce the NSF along a pile surface (Bjerrum et al. 1969, Walker 1973, Indraratna et al. 1992). However, this coating also decreases the load bearing capacity and safety factor of the pile, restricting its application to end-bearing piles. Furthermore, the bitumen becomes brittle and detaches under dynamic loading during pile driving, posing environmental risks including groundwater pollution and soil contamination.

Another potential method involves adopting sacrificial pile to form a pile group, thereby reducing the dragload (Okabe 1977, Lee and Chen 2003, Ng et al. 2008). Okabe (1977) conducted a field test on a group of 38 piles to examine the mobilization of NSF induced by dewatering and surcharge loading. The results indicated a group effect of approximately 87% for the internal piles and 51% for the external protective piles. The group effect, defined as the reduction in maximum dragload compared to a single pile under identical site conditions, was significant. Ng et al. (2008) conducted the centrifuge tests and reported group effects of 53% and 34% at pile spacings of 5.0 and 6.0 times the shield pile diameter, respectively. GEOHK (2006) suggested a group effect of 10-20% for groups of more than five piles based on field observations. However, to date, experimental research on the effect of pile spacing on the development of NSF and dragload still remains limited, particularly concerning the critical pile spacing beyond which no group effects occur. Despite the significant attention this topic has received in recent years, reported critical pile spacing varies, ranging from 2.5*D* (Koerner and Mukhopadhyay 1972) to 3.5*D* (Thomas et al. 1998) to 6*D* (Lee and Chen 2003), where *D* represents the pile diameter.

A series of numerical analyses on pile groups concerning NSF have been conducted (Lee et al. 2002, Lee and Ng 2004, Comodromos and Bareka 2005, Lam et al. 2013). Factors such as pile spacing, axial pile head loading, group configuration, relative pile-soil stiffness, surcharging loading, and soil slip have been examined to assess group effects on NSF. However, the existing literature has largely overlooked the creep behavior of soft soils, which may lead to an underestimation of NSF in practice and result in potentially risky designs. The creep deformation in clay is intrinsic to soft soils and should be considered in engineering design (Yin and Graham 1994, Chen et al. 2021). Although settlement due to creep may constitute only a small percentage of the total settlement, even a few millimeters of relative displacement can fully mobilize the NSF (Fellenius 2006, Yan et al. 2012). The impact of creep on the group effect of NSF is not yet fully understood and the development of dragload within a group involves complex pile-soil-pile interactions. Therefore, further research is highly desirable.

Although the time- and cost-effective numerical analysis on NSF have been extensively studied, the pile penetration process has often been ignored, with a so-called 'wished-in-place pile' assumption for simplicity. However, the change in stress state and the generation of excess porewater pressure in the soil around the pile tip and shaft during pile installation significantly affect the skin friction throughout the service of a pile after penetration. Randolph (2003) identified the three key phases that occur during pile penetration into saturated soil: pile installation, equilibration of the excess porewater pressure and pile head loading. During pile penetration, the soil surrounding the pile tip is squeezed outwards to accommodate the pile volume. The adjacent soil is severely distorted and under large normal stress and shear stress. Meanwhile, the excess pore pressure is generated around the pile. Following the penetration procedure, the dissipation of excess pore pressure with consolidation increases the effective stress, leading to the increase in both shaft friction (PSF) and pile capacity over time (Basu et al. 2014). However, the effect of pile penetration on NSF is not well considered, which may result in an underestimation of the dragload magnitude.

Previous numerical analyses focusing on the pile installation in clay have been conducted using the cavity expansion theory (Randolph et al. 1979, Yu 2000) and strain-path method (Baligh 1985, Sagaseta et al. 1997, Whittle and Sutabutr 1999). In the last 20 years, the finite element method (FEM) has gained prominence due to increasing computing power. It possessed a comprehensive mathematical theory and superior computational performance, making it extensively applied in engineering practice. Particularly, the simulations of pile penetration from ground level to the desired embedment length fall within the large deformation finite element category, which involves geometric distortion and often geomaterial nonlinearity (Abu-Farsakh et al. 2015). Various methods have been proposed to solve the LDFE analyses. Wang et al. (2015) investigated and summarized the performance and limitations of three widely used LDFE methods within the Arbitrary Lagrangian-Eulerian (ALE) framework: the remeshing and interpolation technique by small strain (RITSS) method (Hu and Randolph 1998), an efficient ALE (EALE) method (Nazem et al. 2006) and the Coupled Eulerian-Lagrangian (CEL) approach (Dassault Systèmes 2020). Using the remeshing and interpolation strategy, the RITSS method is relatively robust and versatile among other techniques and can be integrated with other commercial FE packages. The RITSS method divided the large strain problem into multiple small Lagrangian increments. At the end of each increment, the deformed geometry is remeshed with new undistorted elements. Solution variables, including stresses, pore pressure, and void ratio, are then interpolated from the old mesh to the new mesh. However, the accuracy and convergence of the FEM solution can be significantly affected by mesh distortion.

To address this issue, the particle-based finite element method (PFEM) is proposed, utilizing the Delaunay triangulation technique to avoid mesh distortion through frequent remeshing (Monforte et al. 2017, Fang et al. 2024a). The features of the PFEM allow it to combine the flexibility of the meshless particle method for handling large deformation problems with the rigorous mathematical theory of the traditional FEM (Wang et al. 2022). However, during each remesh process, solution variables stored at the Gaussian points, such as stress, pore pressure, and void ratio, are interpolated from the old mesh to the new mesh, inevitably introducing interpolation errors into the numerical results (Jin et al. 2021). To overcome this obstacle, a stable node-based gradient smoothing approach was implemented within the PFEM framework, referred to as SNS-PFEM (Jin et al. 2021, Wang et al. 2022, Fang et al. 2023). This method has been rigorously validated for solving large deformation problems in geotechnical calculations.

1.2 Objectives and scope

This thesis aims to investigate the creep effect on the behavior of single piles and pile groups subject to dragload. The 2D axisymmetric numerical model for a single pile and 3D quarter numerical model for a pile group are developed to quantify the creep effect on the development of NSF and NP during consolidation. Additionally, the pile penetration effect on the development of NSF is examined in detail. The tasks performed to achieve the objectives of this research included the following:

- Implemented an elasto-viscoplastic model with an enhanced time integration algorithm to account for the creep behavior of soft soil within the finite element software.
- Investigated the NSF and NP of a single pile embedded in soft soil, focusing on the influence of varying degrees of creep on the changes in NSF and NP during both the primary and secondary consolidation phases.
- Proposed an exponential prediction model to capture the time-dependent behavior of the NP location.
- Examined the creep effect of group shielding on dragload and quantified the contribution of sacrificial piles to the group effect, considering various soil parameters and pile spacing.
- Developed a novel hydro-mechanical coupled SNS-PFEM framework to explore the effect of pile penetration on the development of NSF.
- Proposed an empirical model for the time-dependent behavior of the β value and verified its applicability to similar cases reported in the literature.

1.3 Thesis organizations

These tasks are addressed across three technical chapters, with a primary focus on numerical research, within a total of six chapters:

- Chapter 1 introduces the background of this research, outlining its objectives and scope.
- Chapter 2 reviews the current understanding of NSF and identifies the research gap in the numerical analysis on NSF and NP.
- Chapter 3 investigates the NSF of a single pile embedded in soft soil, considering both the presence and absence of soft soil creep.
- Chapter 4 explores the creep effect on the group shielding of dragload and quantifies the contribution of sacrificial piles to the group effect.
- Chapter 5 examines the influence of pile penetration on dragload development within the novel SNS-PFEM framework.
- Chapter 6 summarizes the conclusions drawn from the numerical study and provides recommendations for future research.

Furthermore, a schematic illustration of the development of the research from Chapter 3 to Chapter 5 is presented in Figure 1-1.

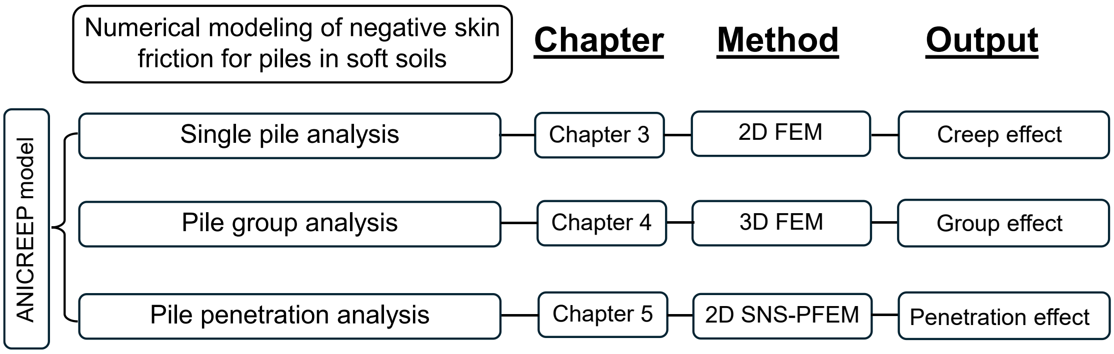

Figure 1-1 Overview of Chapters 3-5

CHAPTER 2 LITERATURE REVIEW

2.1 Drawback of NSF

Generally, the development of NSF can be illustrated in Figure 2-1. The term "negative" in negative skin friction refers not only to the friction direction, which opposes positive skin friction, but also to its adverse impact on engineering projects. As discussed above, the NSF can apply the additional axial force on the pile which may exceed the structural load of the pile and cause the pile structural failure because of overstress (Poulos 1997). Additionally, the NSF will cause the additional settlement of the pile, which may severely compromise the serviceability of the superstructure due to the differential settlement.

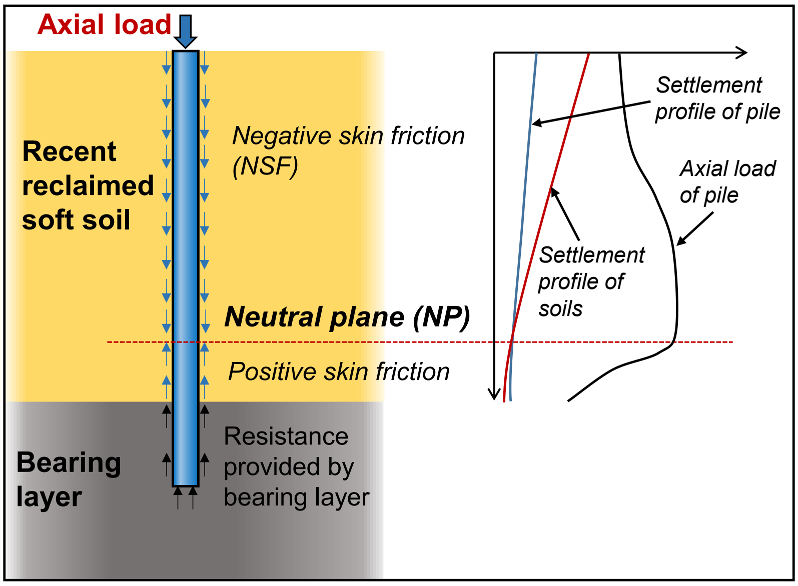

Figure 2-1 Illustration of negative skin friction on a pile

The first instance of NSF was recorded by Terzaghi and Peck (1948), noting that many buildings on the coastal plains of Holland required piles to be driven through very soft soil layers until reaching an end-bearing sand stratum. When a thick layer of fill was placed over the site before pile installation, these pile-supported buildings experienced excessive settlement. Milner (1957) presented a case in which the settlement of a pile supporting the concrete tunnel was induced by the increasing load above the tunnel. Furthermore, field histories also reported the excessive settlement of piles caused by the geotechnical engineers' failure to consider the NSF, which led to the differential settlement of the superstructure (Bozozuk 1981, NAVFAC 1986, Hansbo 1994, Jacob and Kenneth 1996).

Aside from failures caused by downdrag, case histories have also convincingly reported that the pile structural failure due to the dragload results from overstress. Kog (1987, 1990) documented pile structural failure caused by the additional mobilization of NSF after 6 years of service. Davisson (1993) presented case histories involving the timber piles, where dragload led to pile failure, even though the NSF had been identified as a concern by the geotechnical engineers.

The above observation presents a significant challenge for the geotechnical engineers in understanding the mobilization mechanism of NSF and addressing potential risks to the upper structure, particularly when the pile is installed through the soft clays.

2.2 NSF development on single pile

Subsequently, particularly in the 1960s, there was a notable increase in field case research focused on the mechanistic behavior of NSF on piles. Over time, Fellenius (1998) referred to this period as the "golden age" of NSF studies, which contributed significantly to the development of current design methods. Some representative field test histories are provided below.

Bjerrum et al. (1969) presented a case study in Heröya, Oslo Harbor, Norway, on a steel closed-toe driven pile that penetrated approximately 20 m of silty clay, with a fill layer approximately 10 m thick fill on the top, ultimately reaching the bedrock. Two piles were primarily examined: the first was a standard pile, and the second was coated with a 1-mm thick layer of bitumen. Prior to this test, the top fill had been in place for over 70 years, and the consolidation of the underlying silty clay had nearly been completed. Ground settlement was minimal, measuring only a few millimeters per year. After 14 months of field monitoring, the ground surface at the site settled by approximately 160 mm and the pile head settled by approximately 30 mm, with a pile shortening of 10 mm and a dragload of up to 1000 kN for the normal pile. In contrast, the maximum dragload for the bitumen coated pile was around 100 kN, with a pile shortening of 1 mm. The author found that the design load for a single pile would be reduced by half due to the NSF. Therefore, it is recommended to use bitumen coated piles with an end bearing pile toe embedded into rock to avoid doubling the number of piles.

Bjerrum et al. (1969) also summarized the results of other studies conducted by Norwegian Geotechnical Institute (NGI), indicating that the maximum dragload for the steel piles ranged from 1200 kN to 4000 kN for piles with an embedment length of 30 to 60 m. Minor soil settlement was observed in these cases on account of reconsolidation after pile driving and continued secondary compression. It was concluded that only small relative movements were required to fully mobilize the maximum NSF value.

In the same year, Endo et al. (1969) conducted field measurements on NSF using steel-driven piles with open-ended and close-ended pile toe types in Fukagawa, Tokyo, Japan, over a three-year period. The piles had an embedded length of 43 m and a diameter of 0.609 m. The soil profile consisted of a 2 m thick fill layer, followed by an 8 m thick of silty sand layer, a 32 m thick of silt layer, and a fine sand layer at greater depth. The downward gradient of groundwater caused by pumping induced the consolidation of the soft soil layers. After approximately two years of monitoring (from June 1964 to April 1966), the maximum dragload mobilized along the closed-ended pile reached about 3200 kN. The pile head settlement was around 60 mm, while the soil surface settlement reached 175 mm. Notably, an upward movement of the NP position was observed during the monitoring period.

Fellenius (1972) and Bjerin (1977) conducted a field monitoring case study focusing on dragload development in precast driven concrete piles installed through 40 m of clay and 12 m of sand layers in Sweden. The field observations were generally divided into three scenarios: Scenario A – After pile installation, dragload development was measured over 1.5 years using three load cells embedded in the pile. Scenario B – A load of 440 kN was applied to the pile head to simulate upper structure loading, which was increased to 800 kN after one year. Scenario C – A fill was placed on the soil surface, continuing until the end of the test. In Scenario A, rapid dragload accumulation was observed attributed to the dissipation of excess porewater pressure caused by pile driving and soil reconsolidation. Despite soil settlement being less than 1 mm and relative displacement between the soil and pile was lower than 1 mm, the dragload reached 465 kN by the end of this phase. In Scenario B, the dragload was mitigated rather than amplified following the application of dead load on the pile head. A reversal from negative skin friction to positive skin friction was monitored after a loading of 800 kN. However, a substantial amount of NSF reaccumulated along the pile shaft during subsequent consolidation. By the end of Scenario C, the soil surface settlement reached about 1000 mm, while the pile head settlement was 8 mm, comprising 4 mm of pile shortening and 4 mm induced by penetration into the end-bearing sand layer. The final measured dragload on the pile NP position was approximately 2650 kN. Furthermore, the results indicate that the applied axial load and the locked-in dragload (i.e., the amount of NSF developed on a pile shaft before the application of the external axial load) cannot occur simultaneously on piles.

Walker (1973) reported on a driven 760 mm-diameter closed-ended pipe pile driven to an embedment depth of 27 m through a 6 m-thick silty sand overlaying a 15.5 m-thick stiff silty clay layer, followed by 3 m of sandy silt resting on dense sand and gravel at greater depths. The pile extended 2.5 m into the sand and gravel. A similar pile, coated with 1.5 mm of bitumen along its entire length, was driven to a depth of 24.5 m. A 3 m-thick fill was constructed following the installation of the pile. After 238 days of monitoring, the maximum dragload on the uncoated pile reached around 1800 kN, while the coated pile experienced a dragload of less than 100 kN. During this period, the final measured settlement was approximately 25 mm, and the ground surface settlement exhibited a linear relationship with the logarithm of time, identifying that the soil settlement resulted from soil creep due to the over-consolidated nature of the silty clay layer.

Clemente (1981) documented field studies in Hawaii involving three driven, instrumented piles (No. 6, No. 7 and No. 8) with penetration depths of 40 m, 49.7 m and 49.7m, respectively. Pile No. 7 was coated with a thin layer of asphalt and a 1 mm thin layer of bitumen. The site consisted of a 4 m thick sand fill, placed long before the study, overlaying a 36 m thick deposit of soft clay, which was followed by 16 m of stiff silty clay. Below 56 m, the soil transitioned into a mixture of medium-dense to dense coral sand transforming and firm to stiff silty coral clay. Subsequently, a 6 m-high embankment was constructed on the ground. After 180 days of field monitoring, the ground settlement measured around 450 mm, with majority of settlement occurring in the upper soil layers. This resulted in minimal relative displacement between the soil and piles at greater depths. The maximum dragload on the bitumen-coated pile No. 7 was 375 kN, compared to 1770 kN for the uncoated Pile No. 8, demonstrating a significant reduction in dragload due to the thin bitumen coating.

Indraratna et al. (1992) carried out a field test in stratified soils to investigate the development of NSF in driven piles and settlement of the soil surface after the construction of an embankment. The test site was located in Bangkok city. The sub-soils were mainly thick layered marine clay, including a weathered clay layer with a thickness of approximately 2-4 m, a thick soft clay layer with a thickness of approximately 16 m, a medium stiff to still clay layer with a thickness of about 6-8 m and then following the sand layer. The groundwater table was located at 1.5-2 m below the original ground surface. The soft clay was slightly over consolidated whereas the top layer of soil had an overconsolidation ratio (OCR) of 3. Through the field investigation, the coefficient of earth pressure at rest ranged from 0.6 to 0.75. Two types of instrumented piles, coated pile (pile treated with bitumen coated thin layer) and uncoated pile (pile without bitumen coated thin layer), were tested. The length of the piles was 27 m, while the outer and inner diameters of the piles were 0.4 and 0.25 m, respectively. After the piles were installed by drop hammer, there remained 2 m of pile length above the ground surface. Then an embankment of 2 m height was built within

3 days. The long-term monitoring of ground surface settlement and pile axial loading was performed for 265 days.

Ho and Mak (1994) conducted field measurements on a driven pile penetrating into the saprolites (soft and friable rock) beneath a reclamation fill placed over 20 years earlier in Hong Kong. The test pile was classified as a friction pile. The measurements revealed no significant NSF development in the long term after the completion of the building. Ho and Mak (1994) attributed this observation to the completion of the primary consolidation of marine deposits and alluvium beneath the reclamation fill prior to the pile installation.

Hong et al. (2015) reported a field case involving four bored piles installed in consolidating ground in Zhejiang's coastal region, China in 2003. The piles consisted of PT piles (PT1 and PT2) with an embedded length of 37 m, and PC piles (PC1 and PC2) with an embedded length of 28 m. The subsurface soils comprised 4 m of fill, placed over 10 years, overlaying 5 m of soft clay, 13 m of silty clay, and 10 m of clay gravel atop completely to moderately decomposed tuff. Before pile installation, the first 2.5 m of surcharge was applied. Following the installation of piles, an additional 2.5 m of surcharge was added. To enhance drainage conditions and reduce consolidation time, prefabricated vertical drains (PVDs) were installed through the soft clay layer. Monitoring of field conditions after 75 days showed that the measured excess porewater pressure indicated approximately 80% of consolidation degree. The maximum dragload mobilized along the shaft was 1200 kN for the PT piles and 900 kN for the PC piles, as shown in Figure 2-2. It is noted that the ratio L_{NP}/L_0 (where the L_{NP} is the depth from the NP to the soil surface, L_0 is the pile embedded length) was around 0.4 for both PT and PC piles. The measured NP position was located in the upper part of the pile, despite the PT piles being founded on stiffer soil. This observation may be attributed to the short monitoring period, which resulted in incomplete consolidation of soil.

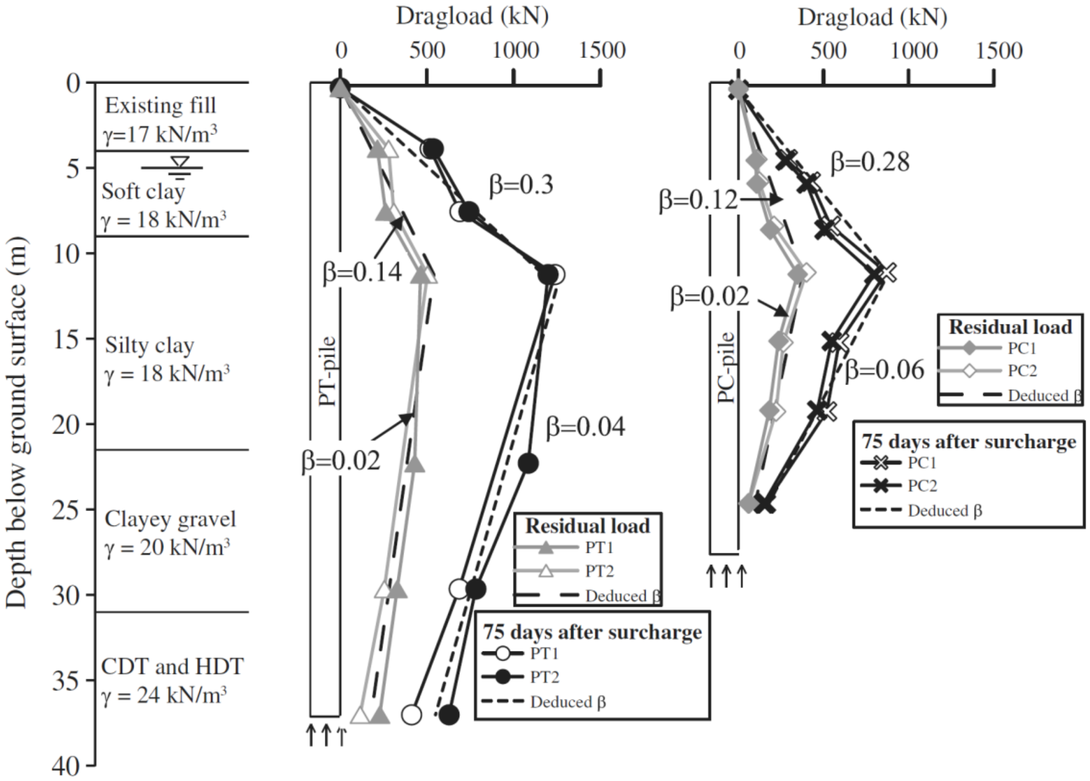

Figure 2-2 Comparison between field measured dragload and the dragload estimated by the β methods (Hong et al. 2015)

Zhang et al. (2022) reported a field case in which over 60 precast PHC piles, each with a diameter of 0.5 m and spaced 3 m apart, were used for ground improvement. Although the field case involves a pile group, Zhang et al. (2022) monitored only the four isolated piles located far apart. Consequently, the site monitoring can be treated as a NSF/NP problem on a single pile. The site consisted of approximately 13 m of soft soil layers underlain by clay, silty clay, and silt resting on bedrock. After the piles were installed through the soft soils into the supporting layer, a load of 110 kPa was applied using fill surcharge. The settlement of piles and surrounding soil was monitored over a period of 103 days. The NP position was back-calculated, revealing an upward movement from the pile toe over time, as shown in Figure 2-3. This behavior contrasts with the observations from other sites, as reported by Indraratna et al. (1992), who documented the downward movement of NP when the piles were supported by stiff soil.

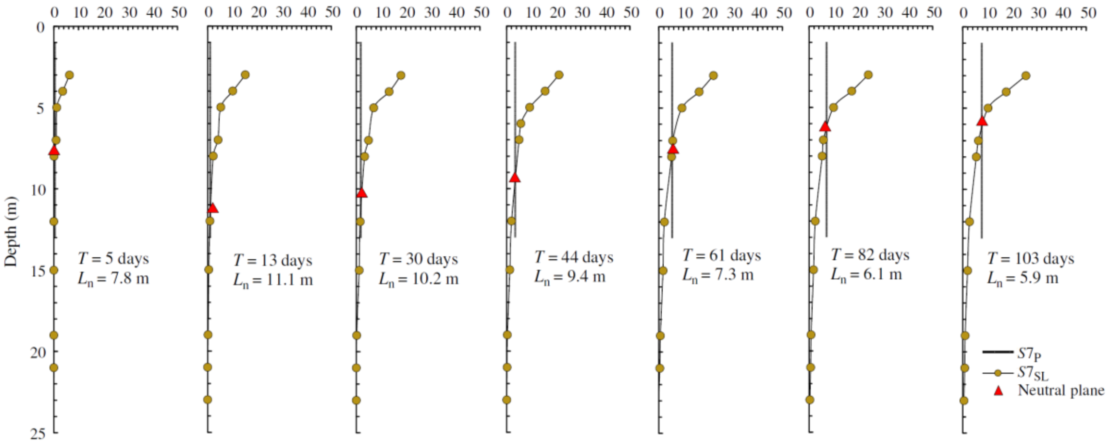

Figure 2-3 Development of soil and pile settlement and the NP position (Zhang et al. 2022)

Except for the field test, the centrifuge tests were also conducted focusing on NSF problems. Leung et al. (2004) presented centrifuge model tests on the self-weight consolidation of soft soil, which induced the mobilization of NSF on a single pile over a period of 83 months. The single pile had a diameter of 1.6 m, was installed through 16 m of soft clay, and socketed 2.5 m into the underlying dense sand layer (all dimensions are given in prototype scale). After the end of test, the measured soil settlement was approximately 1060 mm, and the dragload on the pile reached about 780 kN. It was observed that after reaching a significant soil settlement at 30 months, both pile downdrag and NSF peaked. Although the soil continued to settle by an additional 100 mm, this further settlement did not lead to any additional dragload or downdrag on the pile. During the axial pile head loading test, it was concluded that the applied load needs to exceed three times the maximum locked-in dragload to fully cancel the NSF, as shown in Figure 2-4.

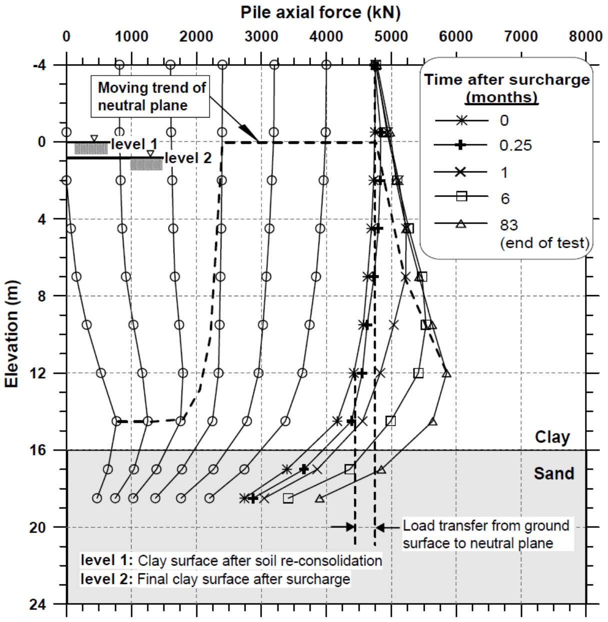

Figure 2-4 Pile head loading effect on NSF and NP following Leung et al. (2004)

From the above-mentioned field measurement and model tests, the following conclusions can be summarized:

1. The mobilization of NSF requires only a few millimeters of relative displacement between the pile and the surrounding soil. Despite the completion of primary consolidation in the soft soil, a significant NSF may still develop due to soil creep. Therefore, the potential for creep-induced NSF must be carefully considered in the pile foundation design.

2. Pile head loading significantly influences the mobilization of NSF, particularly for friction piles where large pile settlements caused by pile head loading can reverse NSF to PSF. Over time, NSF continues to accumulate as long as soil settlement persists. However, for end-bearing piles on a rigid base, such as the rock-socketed piles, NSF is partially relieved due to the limited settlement of the pile (see the example in Leung et

al. (2004) that the applied load needs to exceed three times the maximum locked-in dragload to fully cancel the NSF), primarily resulting from elastic compression. Consequently, NSF poses a greater concern for the structural capacity of rigid-base piles than for friction piles, particularly for longer piles.

3. The pile installation method will influence the NSF mobilization such as the driven pile. Fast increment of NSF due to the dissipation of the pile penetration induced excess porewater pressure.

4. To determine the amount of negative skin friction, it is essential to estimate the position of the NP. For friction piles, the NP is located 60-80 % down the pile length, whereas for end-bearing piles, it is positioned near the pile toe. The NP also represents the equilibrium position where the sustained load on the pile head, combined with the dragload, is balanced by the positive shaft resistance below the NP and the pile toe resistance.

5. The design of NSF should account for both the structural and geotechnical capacity of the pile, as well as the downdrag caused by the dragload. Generally, NSF is evaluated in conjunction with dead loads and sustained live loads, excluding transient live loads or superimposed loads (Fellenius 1998). Transient live loads are typically resisted by positive shaft friction through the pile's elastic compression (Fellenius 2006).

6. A thin coat of bitumen, approximately 1-2 mm thick can reduce the NSF along a pile surface. However, this coating also decreases the loading capacity and the safety factor of the pile. This approach can be considered only for end-bearing piles and presents several limitations. Furthermore, the bitumen becomes brittle and detaches

under dynamic loading during pile driving. Its use also raises environmental concerns, as it consists of harmful organic compounds that can contribute to groundwater pollution and soil contamination.

Furthermore, Briaud (1997) recommended considering dragload in specific site conditions, including: total ground settlement exceeding 100 mm, ground settlement exceeding 10 mm after pile installation, embankment heights higher than 2 m, soft layer thickness exceeding 10 m, water table drawndowns of more than 4 m, and the pile lengths exceeding 25 m.

2.3 Current design method on NSF

To accurately estimate the dragload in a single pile, two parameters are typically required: the distribution and magnitude of unit skin friction, and the location of the neutral plane. Various empirical methods have been proposed for the evaluation of NSF and NP.

2.3.1 Estimation of skin friction

The developed NSF on the pile shaft can be calculated using either the total stress-based α method or the effective stress-based β method:

$$f_s = \alpha s_u \tag{2-1}$$

$$f_s = \beta \sigma'_v \tag{2-2}$$

where f_s is the shaft friction, s_u is the undrained shear strength of the clay and σ'_V is the effective vertical stress. α and β are the adhesion factor and empirical factor, respectively.

In the α method, the α parameter is normally less than 1. However, in cases where surcharges induced a sharp increase in NSF, α can exceed 1. For example, Endo et al. (1969) observed that the mobilized NSF aligned with the undrained shear strength, indicating an α value of 1. Similarly, Lam et al. (2009) reported an α value of 1.08 for the single pile in the centrifuge tests at a consolidation degree of 90%. Shen (2008) reported an α value as high as 1.9 in the centrifuge tests. The wide variation in reported α values can be stemmed from the improper use of the initial shear strength before the pile installation and surcharge application to back-calculate α. To address this issue, Canadian Geotechnical Society (2006) recommended using the s_u after soil consolidation under the new load and proposed an α value range from 0.5 to 1.0.

Although the use of α method is convenient since the ease of obtaining soil strength data in practice, this method fails to account for critical factors, such as stress changes induced by pile penetration as well as the time-dependent behavior of NSF. Lam et al. (2009) also noted that relying on a single α value is insufficient to account for the reduction of NSF below the NP for the friction pile.

The β method (Johannessen and Bjerrum 1965, Endo et al. 1969, Burland 1973) is based on the effective stress theory, which better aligns with engineering conditions. The β method has been shown to provide significantly better agreement with field observations of NSF compared to the α method (Lee 2001). Since NSF is a long-term issue related to consolidation, it is more reasonable to account for changes in effective stress when estimating shear stress at the interface.

The β value is recognized as a critical parameter for estimating the NSF, and it is influenced by multiple factors. Field test reported in Section 2.2 indicate that the β value ranges from 0.18 to 0.25 for the soft soil case studies and centrifuge tests (Johannessen and Bjerrum 1965, Burland 1973, Clemente 1981, Indraratna et al. 1992, Leung et al. 2004). However, some variations show higher values, such as 0.5 for the marine clay (Leung et al. 1991). For silt clay, silt and sand, the β value is generally higher (Endo et al. 1969, Walker 1973). NAVFAC (1986) primarily recommended the β method for calculating unit skin friction, depending on soil type: 0.20-0.25 for clay, 0.25-0.35 for silt and 0.35-0.50 for sand. Similarly, Canadian Geotechnical Society (2006) suggested a β value range of 0.20-0.30.

2.3.2 Estimation of NP

As discussed above, the boundary between PSF and NSF is termed as the neutral plane (NP) or neutral point, as shown in Figure 2-5(a). There is a transition zone around the NP, where the NSF transitions into the PSF, indicating that both NSF and PSF are partially mobilized in this region. The NP is also the point where the pile's axial force reaches its maximum, as indicated in Figure 2-5(b), and where the pile and surrounding soil move equally, as illustrated in Figure 2-5(c). The dragload mobilized at the NP, $P_{\text{drag, NP}}$, can be expressed as:

$$P_{\text{drag, NP}} = \pi D \int_0^{L_{\text{NP}}} f_s dz \tag{2-3}$$

where L_{NP} and D are the distance from the pile top to the NP and the pile diameter, respectively. Notably, the position of the NP is critical for accurately determining the distribution of skin friction in the soil. An inaccurate estimation of the NSF and NP can lead to either uneconomical or risky designs. For convenience, the position of the NP is commonly expressed as its relative position L_{NP}/L_0, where L_0 represents the pile length within the soft soil.

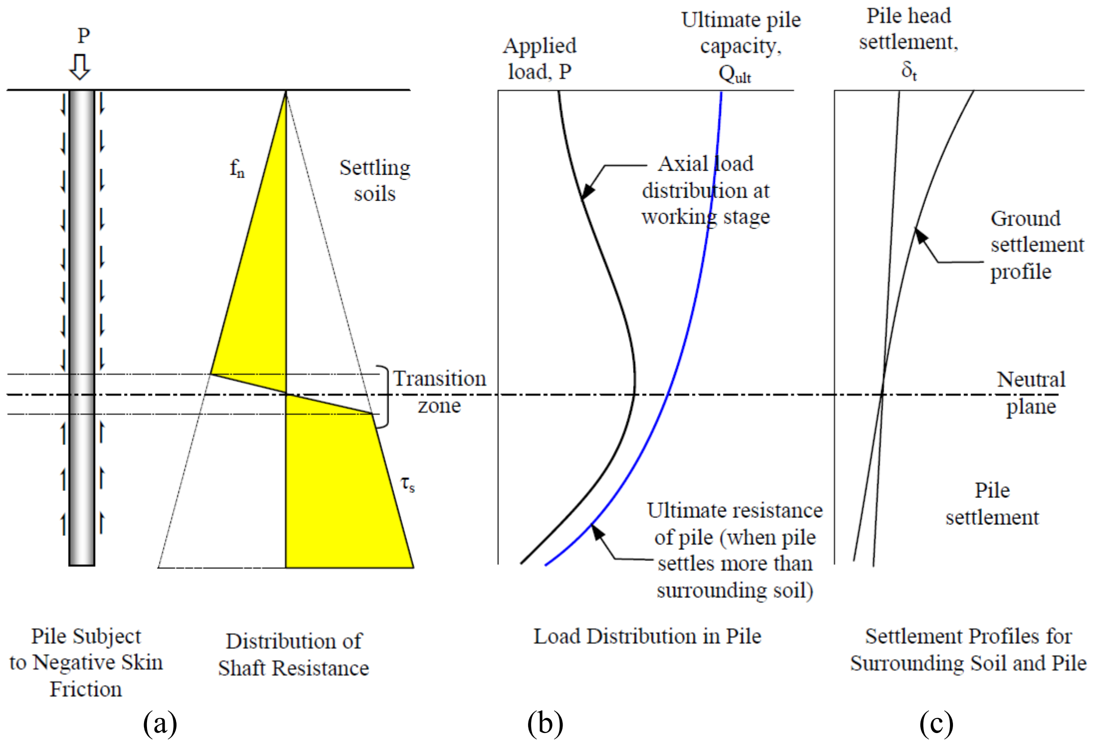

Figure 2-5 NSF estimation with effective stress method (BD 2017)

Alonso et al. (1984) developed a stress-transfer method to describe the interaction between the pile and soil induced by NSF. They proposed a design chart for determining the NP position under various conditions. The NP is located at $L_{NP}/L_0=0.7$, with zero pile toe resistance and no pile head loading. NAVFAC (1986) suggested that the value of L_{NP}/L_0 can be roughly estimated as 0.75 for floating piles in a compressible soil layer. Bowles (1997) presented a simple design method to locate the NP, considering the surcharge load, with a calculated value of approximately 0.67. The Chinese national standard (Ministry of Housing and Urban-Rural Development of the People's Republic of China 2008) provided empirical values for the NP based on the surrounding soil type at the pile tip. The suggested NP location L_{NP}/L_0 is 0.5-0.6 for the clay or silt, 0.7-0.8

for medium or dense sand, and 0.9 or 1.0 for gravel and bedrock. Alternatively, in Hong Kong, the NP can be conservatively taken as the base of the lowest compressible layer (BD, 2004a).

Instead of a simple suggestion based on soil conditions, the Japanese Architectural Institute (AIJ 2001) proposes a formula that offers a reasonable estimation by considering various controlled factors:

$$L_{NP} = \frac{K_v S_0 + \bar{\tau} U L_0 - P}{\left(K_v S_0\right) / L_0 + 2\bar{\tau} U} \tag{2-4}$$

where K_v is the vertical spring coefficient of the pile-tip soil; S_0 is the settlement of the surface soil; U is the circumference of the pile; $\bar{\tau}$ is the unit skin force; P is the stress acting on the pile head.

However, the previously discussed methods failed to account for the time dependency of the NP. To address this limitation, Zhang et al. (2022) proposed an exponential function describing the time-dependent NP position, as presented below:

$$L_{\mathrm{NP}} / L_0 = A e^{Ct} + B \tag{2-5}$$

where A, B and C are the fitting controlling factors with practical meanings, illustrated in Figure 2-6. A represents the movement trend of the NP; B denotes the ultimate NP position; the sum of A and B corresponds to the initial NP position. The absolute value of C indicates the curvature of the proposed curve, reflecting the initial changing rate of the NP position.

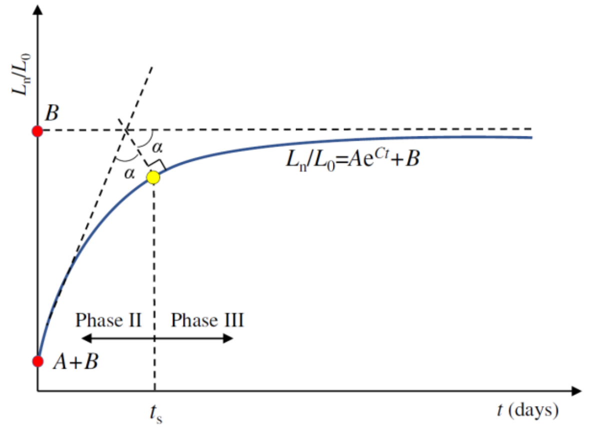

Figure 2-6 Exponential model for time dependent NP position after Zhang et al. (2022)

Generally, these methods can reflect the NP position measured in field tests, such as L_{NP}/L_0 = 0.9 (Kog 1990, Leung et al. 2004) and 1 (Johannessen and Bjerrum 1965, Ng et al. 2008) for end-bearing/friction end-bearing piles, and 0.84 (Indraratna et al. 1992), 0.7 (Endo et al. 1969) and 0.76 (Ng et al. 2008) for friction piles. Most of these suggestions neglect the time dependence of the NP position, except for the method proposed by Zhang et al. (2022). However, the empirical method proposed by Zhang et al. (2022) also faces challenges in estimating the values of parameters A, B and C. These fitting parameters are influenced by site conditions such as surcharge load, pile head loading, the properties of consolidation, end bearing layer, creep effect, pile size and pile-soil interface friction. Moreover, the site conditions vary between projects.

As for the regional technical codes, such as those from NAVFAC (1986) and BD (2017), are generally appliable but do not account for specific site conditions. The Japanese foundation code (AIJ 2001) suggests an empirical formula; however, this requires further investigation to determine the soil parameters.

2.4 NSF development on piles inside a group

Although the NSF on single pile has been extensively investigated through various methods, including field tests, centrifuge tests and 1g tests, field studies examining NSF on pile groups are rare due to the prohibitively high costs and complexity involved. A review of the literature reveals limited test data from previous studies on NSF in pile groups, which are briefly presented herein.

Okabe (1977) observed the development of NSF within a pile group induced by dewatering and surcharge loading. The pile group comprised 38 piles, including 14 external protection piles without head connections and 24 internal end bearing piles with pile heads connected to a rigid pile cap. The pile spacing was 2.1 times pile diameter. The test results revealed a group effect of approximately 87 % for the internal piles and 51% for the external protection piles.

Keenan and Bozozuk (1985) reported the full-scale measurements of dragload on a pile group consisting of three piles spaced at four times the pile diameter. The site was underlain by a compressible silt clay. They concluded that no group effect was observed within this pile group.

Little (1994) reported field measurements for a 3 × 3 free-headed pile group with a spacing of four times the pile diameter. The site consisted of a 15 m thick deposit of soft to firm clay. The study investigated two types of pile groups: friction piles and end-bearing piles. Group effects of approximately 10 % for the friction pile group and 20 % for the end-bearing pile group were observed.

Except for the time and labor consuming field test, the geotechnical centrifuge is also a powerful tool to study NSF problems. Lee and Chen (2003) investigated the NSF on pile groups in centrifuge tests, considering 2-pile, 4-pile and 5 pile configurations with pile spacings ranging from 2 to 6 times the pile diameter. NSF was induced by self-weight consolidation and groundwater lowering. The study indicated that NSF mobilization decreased with reduced pile spacing and fewer piles in the group. Additionally, center piles experienced smaller NSF compared to edge piles. However, when the pile spacing exceeded six times the pile diameter, the NSF on center piles equaled that of an isolated pile.

Ng et al. (2008) conducted the centrifuge test to investigate the shielding effects on the NSF and dragload for the pile groups. An instrumented center pile with a diameter D of 1.2 m (all mentioned scales in this section refer to prototype size) was surrounded by eight sacrificial piles with a diameter d of 0.6 m, forming a 3×3 pile group with pile spacings of $5.0d$ and $6.0d$ for different test configurations. Both the center pile and sacrificial piles were embedded in the 17.7 m thick saturated soft clay layer, with the pile tip location of the group positioned 0.3 m above the bottom stiff sand stratum. All model piles were constructed from aluminum tubes with a Young's modulus of 70 GPa. Leighton Buzzard sand and Speswhite China clay were utilized to form the bottom sand layer and soft soil layer for the test. After the clay reached an undrained shear strength of 18 kPa, boreholes were created using augers to install the model piles in 1g conditions. Subsequently, sand fill was rained on the top of the clay layer to generate an equivalent surcharge loading of 45 kPa at 60 g. During the test, the centrifuge was spun up to 60 g, and the variations in the excess porewater pressure, soil surface settlement, dragload on piles were continuously monitored until the clay achieved a consolidation degree of 90%.

The measured maximum dragload of the center pile in the group was found to be 53% and 75% of that of an unprotected single pile at pile spacings of 5.0 and 6.0 times the pile diameter, respectively. Similarly, the downdrag settlement of the center pile was measured to approximately 57% and 80% of the settlement was recorded for an isolated pile. These results were further validated through FEM package ABAQUS, with the Cam-Clay model employed to simulate the soft soil and the Mohr-coulomb model used for the end-bearing sand.

The small scale tests under 1g condition were conducted by Koerner and Mukhopadhyay (1972), Shibata et al. (1982) and Ergun and Sönmez (1995). These test results indicated that when the pile spacing exceeds 2.5 times (Koerner and Mukhopadhyay 1972) / 5 times (Ergun and Sönmez 1995) the pile diameter, the group effect on NSF becomes negligible. However, due to the inability to replicate the correct stress levels at the prototype scale, the results of these 1g model tests must be interpreted with caution and remain challenging to extrapolate to the field scale.

From the above-mentioned field measurement and model tests, the following conclusions can be summarized:

1. To date, experimental research on the effect of pile spacing on the development of NSF and dragload remains limited, particularly regarding the critical pile spacing beyond which no group effects occur. Despite the significant attention this topic has received in recent years, the critical pile spacing has been reported to vary, ranging from 2.5*D* (Koerner and Mukhopadhyay 1972) to 3.5*D* (Thomas et al. 1998) to 6*D* (Lee and Chen 2003), where *D* represents the pile diameter. Moreover, the pile group effect on

NSF may also be influenced by the stiffness of the end bearing stratum (Lee and Ng 2004).

2. The existing literature has largely neglected the soft soil creep behavior, potentially leading to an underestimation of NSF in practical designs. The creep deformation of clay is intrinsic to soft soils and should be considered in engineering design (Yin and Graham 1994, Chen et al. 2021). Notably, although settlement due to creep may account for a small percentage of the total settlement, it is important to note that only a few millimeters of relative displacement could fully mobilize the NSF (Fellenius 2006, Yan et al. 2012). The creep effect on the development of dragload and NP remains insufficiently understood, making further research essential.

2.5 Design method for evaluating the dragload within pile group

Several design methods have been proposed for estimating the developed dragload within the pile groups. Both empirical and analytical design methods are summarized in Table 2-1.

Table 2-1 Summary of design methods for dragload evaluation in pile group

No.	Reference	Design methods	Description
Empirical methods			
1	Terzaghi and Peck (1948)	$P_{\text{avg}}=(AP_s+p_g L_c s_u)/n$	where P_{avg} is the average ultimate dragload on the pile within the pile group, A represents the area of a horizontal section within the pile group boundary, enclosed by the perimeter p_g, L_c and γ_c' denote the thickness and effective unit weight of the clay layer, s_u is the average shear resistance of the clay, which can be estimated using $s_u=\frac{M}{2}p'\left(\frac{R_i}{2}\right)^{\frac{\lambda-\kappa}{\kappa}}$, where p' is the mean effective normal stress and R_i is the isotropic over consolidation ratio, P_s is the surcharge loading magnitude, L_{NP} is the distance of the NP from the ground surface, which can be estimated using $L_{NP}=\frac{L}{L_{NP}}\left(\frac{L}{2}+\frac{P_s}{\gamma_c'}\right)-\frac{2P_s}{\gamma_c'}$.
2	NAVFAC (1986)	$P_{\text{avg}}=A\ (P_s+\gamma_c' L_c)/n$	
3	Bowles (1997)	$P_{\text{avg}}=(AP_s+A\gamma_c' L_{NP}+f_s L_{NP} p_g)/n$	

Analytical method			
4	Zeevaert (1959)	$f_s = \beta P_s e^{-n'C'\beta z} + \frac{\gamma_c'}{n'\pi D\beta}(1 - e^{-n'\pi D\beta z})$ $P = \pi D\int_0^{L_{NP}} f_s\,dz$	where n' is the pile number per unit surface area, C' is the perimeter of one pile, D is the pile diameter, z is the depth below the soil surface.
5	Zeevaert (1972)	$P = \frac{\pi D\beta}{1+\frac{\pi D\beta}{3}-\frac{L_{NP}}{\bar{a}}}\int_0^{L_{NP}} \sigma_{0z}^{\backslash\text{primedz}}$	where $\bar{a}$ represents the nominal tributary area and σ'_{0z} is the initial vertical effective stress.
6	Shibata et al. (1982)	$f_s = \frac{\gamma_c' A}{s}[1 - exp(-\chi)] + \beta P_s exp(-\chi)$ $\chi = \frac{4\pi\beta(z/D)n}{16(S/D)^2 - \pi n}$ $P = \pi D\int_0^{L_{NP}} f_s dz$	where s is the sum of pile perimeters in the 2 $S \times 2$ S section, S is the pile spacing, $s = n\pi D, A = 4L^2 - \frac{n\pi D^2}{4}$. The n represents the effective pile number, which can be determined in Figure 2-7.

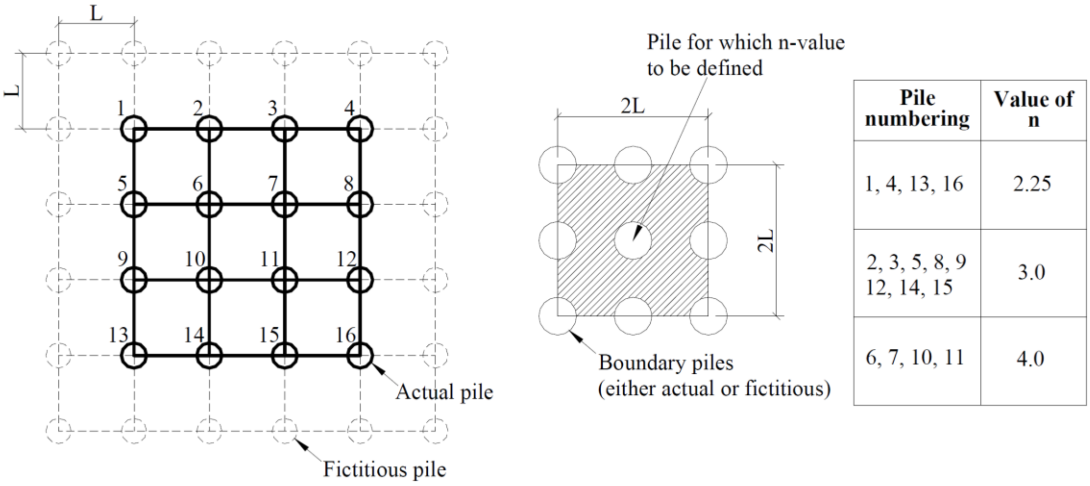

(a) (b) (c)

Figure 2-7 Definition of effective pile number (Shibata et al. 1982): (a) example of pile group; (b) elementary section; and (c) list of n-values

Generally, both the empirical method and analytical methods tend to overestimate the dragload, as reported by Lee et al. (2002) and Shen (2008). Although the reduction in vertical effective stress of soil within a pile group is considered in the models by Zeevaert (1972) and Shibata et al. (1982), the dragload mobilization remains complex, influenced by various factors, such as surcharge loading, pile spacing, soft soil creep effect, pile installation method.

2.6 Numerical study on NSF

Numerical study on NSF starts to bloom on account of the time and economic friendly compared with field test. Some numerical studies on single pile and group pile on NSF had been briefly introduced in this section.

2.6.1 Numerical study on single pile

Indraratna et al. (1992) employed a purely undrained model and a Biot-coupled consolidation model within the FE code to predict the NSF. The MCC (Modified Cam-Clay model) was used to simulate soft clay consolidation, while the deeper, stiffer soil was treated as elastic. A thin solid element represented the pile-soil interface. A relative displacement of 3 mm was considered sufficient to fully mobilize skin friction. The development of NSF was found to be closely associated with the behavior of the thin layer elements at pile-soil interface.

Yan et al. (2012) pointed out that both the built-in contact algorithm and the contact subroutine FRIC in ABAQUS failed to correctly account for excess porewater pressure, indicating that the total stress was used instead of effective stress when handling the pile-soil interaction problem, particularly in coupled fluid-mechanics analysis. Therefore, the subroutines URDFIL and POSFIL were employed to extract excess porewater pressure during each calculation step. Bilinear and hyperbolic shear stress displacement behaviors were introduced to model the development of NSF in soft soil.

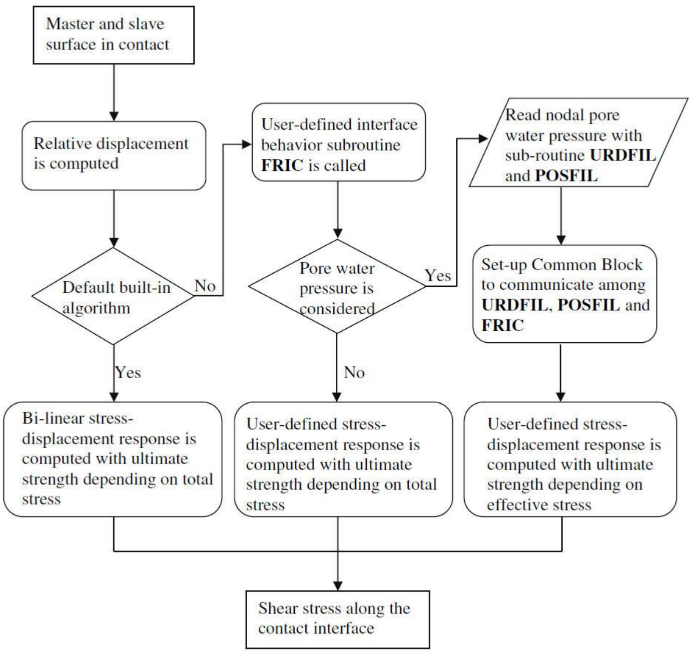

Figure 2-8 Modified interface shear algorithm after Yan et al. (2012)

Liu et al. (2012) adopted a two-dimensional axisymmetric model in ABAQUS to analyze the NSF development in a single pile. The soil was modeled using the Mohr-Coulomb criterion. After calibration with a field case, a parametric study was conducted, considering factors such as consolidation time, the pile-soil interface properties, lateral earth pressure coefficient, pile-soil limiting displacement, surcharge magnitude, and soil stiffness analysis. Similarly, Chiou and Wei (2021) used a 3D effective stress-based coupled fluid-mechanics analysis. The neutral plane position and dragload magnitude for two different types of piles, friction pile and friction end-bearing pile, were calculated under various pile head loadings.

2.6.2 Numerical study on pile group

The soil slip effect within pile group has been extensively examined through numerical analysis by Lee et al. (2002), Jeong et al. (2004) and Lee and Ng (2004). Their studies concluded that the NSF is overestimated if soil slip behavior is not considered. It was recommended that installing piles in relatively stiff soil layers is an economical method to enhance pile group efficiency by reducing negative skin friction and pile settlement. Differential settlement between the center and the perimeter piles in friction pile may induce significant tensile loads at the pile head, as demonstrated by the field case shown in Figure 2-9. Eliminating the dragload requires approximately 125 to 325% of the maximum dragload, depending on the stiffness of the bearing layer. Additionally, the influence of interface friction coefficient, surface loading and axial loading on NSF was fully examined.

Figure 2-9 Field case of piles dragged down from the pile cap due to negative skin friction (after Su et al. 2020)

Comodromos and Bareka (2005) investigated the development of NSF within the pile groups using a three-dimensional finite difference method. They examined the effects of construction, specifically whether the working load was applied before or after embankment construction, on NSF. The results indicated that the smaller NSF occurred when the embankment was constructed prior to the application of the working load, and larger NSF was observed when the working load was applied first. Additionally, the mobilization of dragload in fixed-head friction pile groups was found to be significantly greater than in free-head end-bearing pile groups.

Ng et al. (2008) and Lam et al. (2009, 2013) employed the finite element package ABAQUS to analyze the development of NSF within pile groups. The 3D numerical simulation results, presented as stress contour plots, showed that the reduction in NSF is due to the stress transfer between the consolidating soft soil within the pile group and its surrounding sacrificing piles. This effect is referred to as the “hang-up” effect in pile groups. The sacrificial sleeves were simulated and compared with sacrificial piles within the pile groups. The simulation results indicated that sacrificial sleeves provide a more effective shielding configuration than sacrificial piles.

2.7 Summary

NSF causes the pile to move further downward, adding the additional load on the pile, referred to as dragload. The dragload is considered a detrimental load and has attracted engineering attention since last century. Over several decades, numerical site monitoring studies, centrifuge tests and 1g small scale tests have documented the NSF development in both single piles and pile groups. Design methods for estimating the NSF and NP have been proposed. Although moderate success has been achieved in these studies, several notable drawbacks have been identified, as outlined below:

1. The existing numerical analysis has largely overlooked the viscous behavior of soft soil, particularly creep. The potential for creep-induced NSF must be carefully considered in the pile foundation design, as the mobilization of NSF requires only a few millimeters of relative displacement between the pile and the surrounding soil.

2. Regional technical codes have proposed empirical methods for calculating the NSF and estimating the NP position. However, most studies fail to account for the time dependence of NSF and NP calculations. The consolidation of soft soil typically takes many years, during which the NSF magnitude and NP position gradually evolve. Nevertheless, relatively few studies have qualitatively examined the time-dependent effects on NSF and NP.

3. Experimental research on the effect of pile spacing on the development of NSF and dragload remains limited, particularly regarding the critical pile spacing beyond which no group effects occur. Existing conclusions on the critical pile spacing vary widely, ranging from 2.5D (Koerner and Mukhopadhyay 1972) to 3.5D (Thomas et al. 1998) to 6D (Lee and Chen 2003). Thus, the existing findings are not universally applicable, highlighting the need for further study on this issue.

4. The pile penetration process is often ignored in numerical assessments, where a so-called ‘wished-in-place pile’ assumption is adopted for simplicity. However, the pile installation significantly influences the NSF mobilization throughout the service of a pile. Further analysis is required to investigate this effect.

CHAPTER 3 NUMERICAL ANALYSIS OF TIME-DEPENDENT NEGATIVE SKIN FRICTION ON PILE IN SOFT SOILS

3.1 Introduction

The generation of negative skin friction (NSF) induces the additional axial force on the pile, which exerts a detrimental load rather than a beneficial one. However, the effect of soil creep on the long-term development of NSF has remained poorly understood. The study uses numerical analysis to investigate this effect. This section aims to investigate the NSF of a single pile embedded in soft soil with and without considering creep. Firstly, an elasto-viscoplastic model is used to consider the creep behavior of the soft soil, and with the enhanced time integration algorithm the model is implemented into the finite element code ABAQUS. Then, the numerical model is established and calculated. The creep effects on NSF and NP, as well as settlement and excess pore pressure of the soil in and after the primary consolidation are examined.

3.2 Finite element modeling

3.2.1 Elasto-viscoplastic model with enhanced time integration algorithm

In this section, the finite element software ABAQUS (Dassault Systemes, 2020) is employed to simulate the behavior of the pile-soil system. Although the modified Cam Clay model (MCC) is one of the most popular models for simulating soft soil behavior in ABAQUS (Roscoe and Burland, 1968), the MCC model takes no account of the viscous behavior, such as creep. Therefore, the ANICREEP model that is extended from overstress theory of Perzyna proposed by Yin et al. (2011), has been selected as a representative elasto-viscoplastic model for soft clays in this study.

The main constitutive equations for the ANICREEP model are listed as follows and definitions for the model are presented in Figure 3-1:

$$\dot{\varepsilon}_{ij} = \dot{\varepsilon}_{ij}^{e} + \dot{\varepsilon}_{ij}^{vp} \tag{3-1}$$

$$\dot{\varepsilon}_{ij}^{vp} = \mu \left(\frac{p_m^d}{p_m^r} \right)^{\beta} \frac{\partial f_d}{\partial \sigma'_{ij}} \tag{3-2}$$

$$f_r = \frac{3/2\left(\sigma_d'^r - p'^r \alpha_d\right) : \left(\sigma_d'^r - p'^r \alpha_d\right)}{\left(M^2 - \frac{3}{2}\alpha_d : \alpha_d\right) p'^r} + p'^r - p_m^r = 0 \tag{3-3}$$

$$d\alpha_d = \omega \left[\left(\frac{3\sigma_d}{4p'} - \alpha_d \right) \left\langle d\varepsilon_v^{vp} \right\rangle + \omega_d \left(\frac{\sigma_d}{3p'} - \alpha_d \right) d\varepsilon_d^{vp} \right] \tag{3-4}$$

$$p_m^r = \left(1 + \chi\right) p_{mi} \tag{3-5}$$

$$dp_{mi} = p_{mi} \left(\frac{1 + e_0}{\lambda_i - \kappa} \right) d\varepsilon_v^{vp} \tag{3-6}$$

$$d\chi = -\chi \xi \left(\left| d\varepsilon_v^{vp} \right| + \xi_d d\varepsilon_d^{vp} \right) \tag{3-7}$$

where $\dot{\varepsilon}_{ij}$ denotes the (*i* , *j*) component of the total strain rate tensor, and the superscripts *e* and *vp* represent, the elastic and the viscoplastic components, respectively. The p_m^d is the size of the dynamic loading surface. The p_m^r and p_{mi} are the size of the reference and the intrinsic yield surfaces respectively. The initial reference preconsolidation pressure σ'^{r}_{p0} obtained from an oedometer test can be used as an input to calculate the initial size p_{m0} using Eq. (3-3).

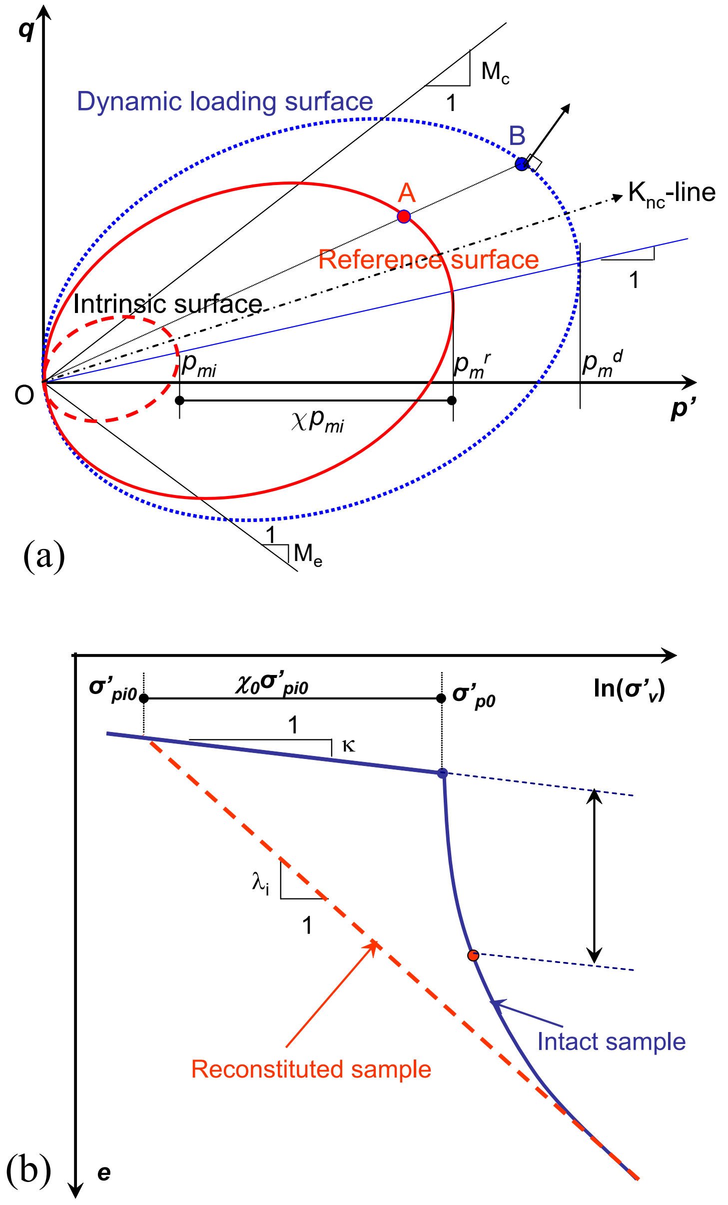

Figure 3-1 Definitions for the model in (a) *p*'- *q* space; and (b) one-dimensional compression condition

The slope of the critical state line M is expressed as follows:

$$M = M_c \left[\frac{2c^4}{1 + c^4 + \left(1 - c^4\right)\sin 3\theta} \right]^{\frac{1}{4}} \tag{3-8}$$

where $c = \left(3 - \sin\phi_c\right) / \left(3 + \sin\phi_c\right)$ according to the Mohr-Coulomb yield criterion (ϕ_c is the friction angle); $-\pi/6 \le \theta = \left(1/3\right)\sin^{-1}\left(-3\sqrt{3}\bar{J}_3 / 2\bar{J}_2^{3/2}\right) \le \pi/6$ using $\bar{J}_2 = \left(1/2\right)\bar{s}_{ij} : \bar{s}_{ij}$, $\bar{J}_3 = \left(1/3\right)\bar{s}_{ij}\bar{s}_{jk}\bar{s}_{ki}$ with $\bar{s}_{ij} = \sigma_d - p'\alpha_d$.

Soil constants and state variables are summarized in Table 3-1 with their recommended methods of determination.

Table 3-1 State parameters and soil constants of elastic viscoplastic model

Group	Parameter	Definition	Determination
Modified Cam Clay parameters	σ'^{r}_{p0}	Initial reference preconsolidation pressure	From a selected oedometer test whose loading-rate is used as reference strain-rate
	e_0	Initial void ratio (state parameter)	From oedometer test
	υ	Poisson's ratio	From initial part of stress-strain curve (Typically varying from 0.15 to 0.35)
	κ	Slope of the swelling line	From 1D or isotropic consolidation test
	λ	Intrinsic slope of the compression line	From 1D or isotropic consolidation test
	M	Slope of the critical state line	From triaxial shear test
Anisotropy parameters	α_0	Initial anisotropy (state parameter for calculating initial components of the fabric tensor)	$\alpha_0 = \alpha_{K0} = \eta_{K0} - \frac{M^2 - \eta_{K0}^2}{3}$ with $\eta_{K0} = \frac{3M}{6 - M}$
	ω	Absolute rate of yield surface rotation	$\omega = \frac{1 + e_0}{\left(\lambda_i - \kappa\right)} \ln \frac{10M_c^2 - 2\alpha_{K0}\omega_d}{M_c^2 - 2\alpha_{K0}\omega_d}$
Destructuration parameters	χ_0	Initial bonding ratio	$\chi_0 = S_t - 1$ (from shear vane test), or $\chi_0 = \sigma'_{p0} / \sigma'_{pi0} - 1$ (from oedometer tests)
	ξ	Absolute rate of bond degradation	From consolidation tests with two different stress ratios $\eta = q/p'$, e.g. oedometer test and isotropic consolidation test
	ξ_d	Relative rate of bond degradation	
Viscosity parameters	$C_{\alpha ei}$	Secondary compression coefficient	From 24h oedometer test on reconstituted sample
Hydraulic parameters	k_{v0}, k_{h0}	Initial vertical and horizontal permeability	From oedometer tests
	c_k	Permeability coefficient	From curve e-log(k)

This model is implemented into ABAQUS as a user-defined material via using the material subroutine UMAT. UMAT will be called at all Gauss integration points of elements through which the ANICREEP is implemented. For each calculation step, stresses and state variables have to be updated, and the material Jacobian matrix is calculated and provided for the stiffness matrix of the element.

Katona (1984) put forward an algorithm for elasto-viscoplastic models using a time integration scheme. To enhance the algorithm, the original Katona algorithm with adaptive substepping (OK-AS) is widely used. In one loading step with strain increment $\Delta\boldsymbol{\varepsilon}$ ($\Delta\boldsymbol{\varepsilon}=\boldsymbol{\varepsilon}_{\mathrm{n}+1}-\boldsymbol{\varepsilon}_n$) and time increment Δt ($\Delta t=t_{n+1}-t_n$), where the n denotes the number of loading steps, the effective stress increment $\Delta\boldsymbol{\sigma}'$ and hardening parameter $\Delta\boldsymbol{\zeta}$ of the ANICREEP model can be expressed as:

$$\Delta\boldsymbol{\sigma}' = \boldsymbol{D}(\Delta\boldsymbol{\varepsilon}-\Delta\boldsymbol{\varepsilon}^{vp}) \tag{3-9}$$

$$\Delta\boldsymbol{\zeta} = \Delta\lambda\boldsymbol{h} \tag{3-10}$$

$$\boldsymbol{\zeta} = \left[p_{ci}\ \ \chi\ \ \boldsymbol{\alpha}_{\mathrm{d}}\right]^T \tag{3-11}$$

$$\boldsymbol{h} = \begin{bmatrix} p_{ci}\dfrac{1+e_0}{\lambda_i-\kappa}\dfrac{\partial f_d}{\partial p'} \\ -\chi\xi\left(\left|\dfrac{\partial f_d}{\partial p'}\right| + \xi_d\dfrac{\partial f_d}{\partial q}\right) \\ \omega\left[\left(\dfrac{3\boldsymbol{\sigma}_d}{4p'}-\boldsymbol{\alpha}_d\right)\left\langle\dfrac{\partial f_d}{\partial p'}\right\rangle + \omega_d\left(\dfrac{\boldsymbol{\sigma}_d}{3p'}-\boldsymbol{\alpha}_d\right)\dfrac{\partial f_d}{\partial q}\right] \end{bmatrix} \tag{3-12}$$

where $\boldsymbol{\sigma}'$ and $\boldsymbol{\varepsilon}$ are the stress and strain vectors respectively, can be expressed as $\boldsymbol{\sigma}'=[\sigma_x',\sigma_y',\sigma_z',\tau_{xy},\tau_{yz},\tau_{zx}]^T$ and $\boldsymbol{\varepsilon}=[\varepsilon_x,\varepsilon_y,\varepsilon_z,\gamma_{xy},\gamma_{yz},\gamma_{zx}]^T$, $\Delta\boldsymbol{\varepsilon}^{vp}$ are the elasto-viscoplastic strain increment vectors, $\boldsymbol{D}$ is the elastic matrix, $\Delta\lambda$ is the viscoplastic multiplier.

In order to apply the ANICREEP model into the finite element software, the step-by-step time integration scheme proposed by Katona (1984) is used, the time dependent strain increment is determined by:

$$\Delta\boldsymbol{\varepsilon}^{vp} = \Delta t\left[(1-\theta)\dot{\boldsymbol{\varepsilon}}_0^{vp} + \theta\dot{\boldsymbol{\varepsilon}}^{vp}\right] \tag{3-13}$$

where $\dot{\boldsymbol{\varepsilon}}_0^{vp}$ are the known viscoplastic strain vectors, Δt is the time increment, θ is the adjustable integration parameter, in the range from $0 \leqslant \theta \leqslant 1$, when $\theta=0$ is the full explicit method, $0<\theta<1$ is the semi-implicit method, when $\theta=1$ is the implicit method. Submitting Eq. (3-9) into Eq. (3-13), the equation could be rearranged as:

$$\boldsymbol{P}(\boldsymbol{\sigma}', \dot{\boldsymbol{\varepsilon}}^{vp}) = \boldsymbol{Q}_0 \tag{3-14}$$

where

$$\begin{cases} \boldsymbol{P} = \boldsymbol{D}^{-1}\boldsymbol{\sigma}' + \Delta t\theta\dot{\boldsymbol{\varepsilon}}^{vp} \\ \boldsymbol{Q}_0 = \Delta\boldsymbol{\varepsilon} - \Delta t(1-\theta)\dot{\boldsymbol{\varepsilon}}_0^{vp} + \boldsymbol{D}^{-1}\boldsymbol{\sigma}' \end{cases} \tag{3-15}$$

The flow chart of original Katona algorithm with adaptive substepping (OK-AS) is shown in Figure 3-2, where the *TOL* represents the convergence criterion used to judge iterative convergence and the superscript *i* denotes the i^{th} iteration.

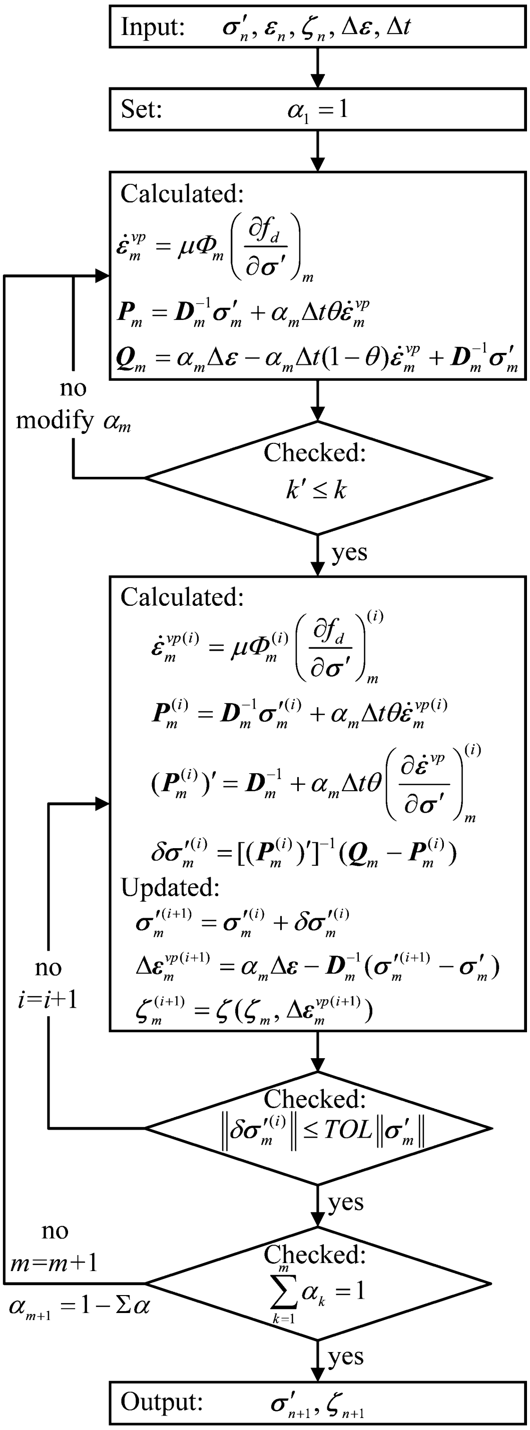

Figure 3-2 Flow chart of original Katona algorithm with adaptive substepping procedure

Since OK-AS failed to consider the hardening parameters changing with viscoplastic strain in the iterative procedure, the convergence rate is significantly reduced. Therefore, in order to improve the robustness of the ANICREEP model and calculation performance in the finite element analysis, the modified Katona algorithm with adaptive substepping (MK-AS) is applied for the stress-strain-time integration. Both the stress and the hardening parameters are changing with viscoplastic strain in the iterative procedure simultaneously. Submitting Eq. (3-9), Eq. (3-10) and Eq. (3-13), the equation could be rearranged as:

$$\bar{\boldsymbol{P}}(\boldsymbol{\sigma}^{'},\ \boldsymbol{\zeta}, \dot{\boldsymbol{\varepsilon}}^{vp}) = \bar{\boldsymbol{Q}}_0 \tag{3-16}$$

where

$$\begin{cases} \bar{\boldsymbol{P}} = \begin{bmatrix} \boldsymbol{D}^{-1}\boldsymbol{\sigma}^{'} + \Delta t\theta\dot{\boldsymbol{\varepsilon}}^{vp} \\ \boldsymbol{\zeta} - \Delta t\theta\dot{\lambda}\boldsymbol{h} \end{bmatrix} \\ \bar{\boldsymbol{Q}}_0 = \begin{bmatrix} \Delta\boldsymbol{\varepsilon} - \Delta t(1-\theta)\dot{\boldsymbol{\varepsilon}}_0^{vp} + \boldsymbol{D}^{-1}\boldsymbol{\sigma}_0^{'} \\ \boldsymbol{\zeta}_0 + \Delta t(1-\theta)\dot{\lambda}_0\boldsymbol{h}_0 \end{bmatrix} \end{cases} \tag{3-17}$$

where $\boldsymbol{\sigma}^{'}$ are the stress vectors, $\boldsymbol{\zeta}$ are the hardening parameters, $\dot{\boldsymbol{\varepsilon}}^{vp}$ is the viscoplastic strain rate, $\boldsymbol{D}$ is the elastic matrix, Δt is the time increment, $\dot{\lambda}$ is the viscoplastic multiplier, θ is the adjustable integration parameter, $\boldsymbol{h}$ are the hardening parameters.

The flow chart of MK-AS is shown in Figure 3-3. The modified viscoplastic strain rate $\dot{\boldsymbol{\varepsilon}}^{vp}$ is updated based on new stress $\boldsymbol{\sigma}^{'}$ and hardening parameters $\boldsymbol{\zeta}$. $\boldsymbol{\sigma}^{'}$ and $\boldsymbol{\zeta}$ can be calculated following the Newton-Raphson procedure. The MK-AS shows more rigorous procedures than OK-AS and can be applied in this study. Besides, different from Wang et al. (2022), the implicit integration scheme (i.e., $\theta = 1$) is used in this study, with the advantages of high accuracy, robust integration and unconditional stability of the implicit algorithm (Yin et al. 2019, Zhang et al. 2022). Substepping parameters *k* is set to 0.01. The convergence criterion *TOL* is given as 0.001, which is considered appropriate for most engineering calculations (Sloan 1987, Feng 2016).

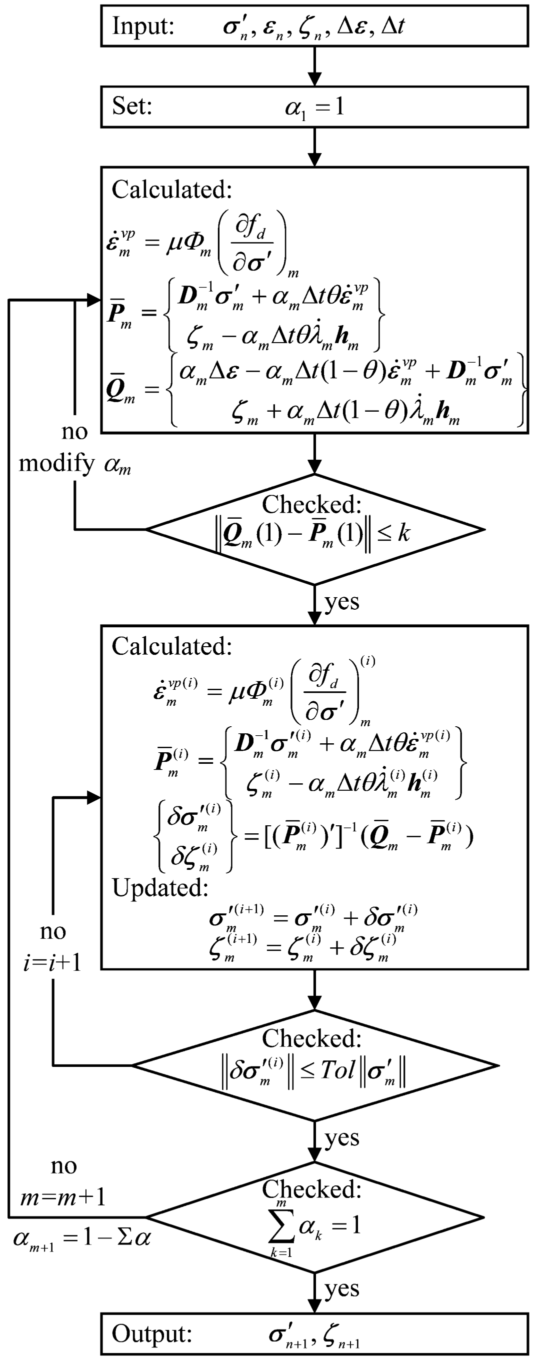

Figure 3-3 Modified Katona Algorithm with adaptive substepping procedure

3.2.2 Numerical analysis background

Indraratna et al. (1992) conducted the field tests to analyze the development of NSF on driven piles and soil settlement after the application of a surcharge embankment has been selected for the validation of the numerical model. The field test is situated in Bangkok City. The ground conditions primarily consisted of thick layered clay, including a weathered clay layer with a thickness of approximately 2-4 m, followed by an around 16-m-thick soft clay layer, succeeded by a medium stiff to still clay layer with a thickness of about 6-8 m overlaying on the sand layer. The groundwater table was located at 2 m below the original ground surface. The soft clay exhibited a slightly over-consolidated, while the upper layer of soil had an overconsolidation ratio (OCR) of 3. The parameters of these soil are detailed given in Indraratna et al. (1992).

Two types of hollow cylindrical instrumented concrete piles, one uncoated (T1) and the other with a 6 mm-thick bitumen coating (T2), were driven slowly into the ground. The outer and inner diameters of these piles were 0.4 and 0.25 m, respectively. Subsequently, a 2-m-high embankment was constructed as a surcharge to induce ground soil settlement within a 3-day period. Long-term monitoring of ground surface settlement and pile axial loading with consolidation was performed for nearly 265 days.

3.2.3 Model parameters

Based on the field tests conducted by Indraratna et al. (1992), the simplified single pile-soil interaction model is considered as two-dimensional axisymmetric in the numerical analysis. The sketch and mesh detail of the numerical model is shown in Figure 3-4. The solid pile with the diameter of 0.4 m and the length of 25 m is fully embedded in the consolidating layer. The bearing layer is 5 m high with the same soil property as the consolidating layer. The size of the model is 10 m × 30 m. The minimum distance from the pile to the boundary is more than 10 times the pile diameter, which is considered large enough to reduce the boundary effect (Sun et al. 2015). The four-node bilinear axis-symmetric finite elements (CAX4 for pile; CAX4P for soil under the groundwater level, which is assumed to be fully saturated) are adopted in mechanical-flow coupled consolidation analysis (Dassault Systèmes 2020). The mesh is denser near the pile and coarser far away from the pile to avoid the influence of the stress concentration and enhance the calculation efficiency. The vertical boundary on the left side is the symmetrical line, the roller boundary and the fixed boundary are applied on the side and bottom of the model, respectively. To simplify the numerical case, pile is assumed wished-in-place rather than being driven (Lee et al. 2002, Liu et al. 2012, Yan et al. 2012, Sun et al. 2015, Chiou and Wei 2021).

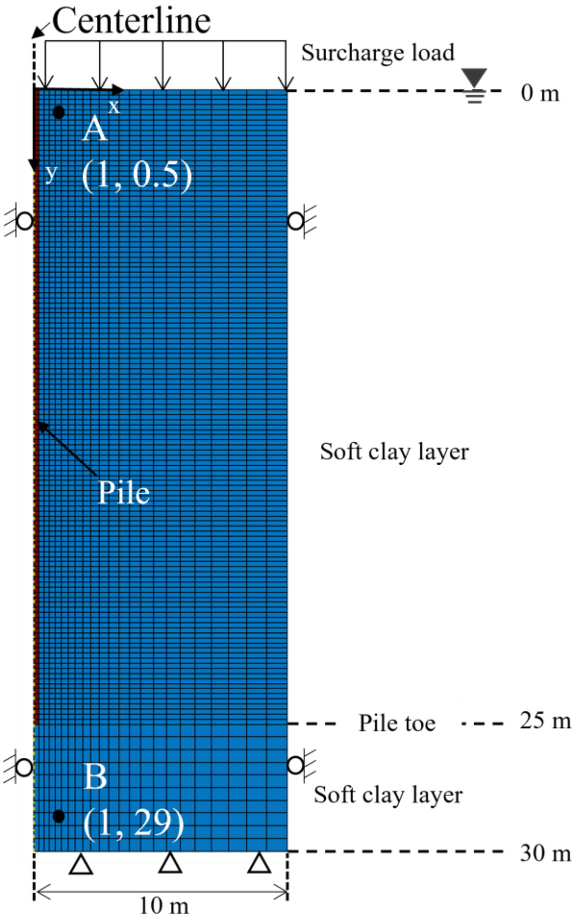

Figure 3-4 Sketch and mesh for the parametric study model (following the field tests conducted by Indraratna et al. (1992))

The friction behavior between soil and pile follows the Coulomb friction law, in which the shear stress is proportional to the relative shear displacement; additionally, the shear stress becomes stable after reaching the threshold displacement. The two governed parameters, are the frictional parameter, μ=0.3, estimated by μ=tan(2/3φ_c) where soil effective friction angle is, φ_c=25°, and threshold displacement, δ=3 mm, which are adopted following Lee et al. (2002) and Yan et al. (2012).

In the model calculation procedure, the geostatic step is calculated first to generate the initial stress of each stratum. After the geostatic equilibrium, the surcharge loading is applied on the top of ground surface in mechanical-consolidation coupled analysis step. Then the excess pore pressure will dissipate within the assigned time period in the consolidation stage. The drainage boundaries are placed at the ground water table.

The isotropic linear elastic model is applied for modeling the pile and end bearing sand layer. A solid pile rather than a hollow pile is used, the typical equilibrium elastic modulus of the solid pile is calculated equal to 30 GPa to maintain the same axial rigidity compared with the hollow steel pile. The ANICREEP model is used for capturing the creep behavior of soft soil. Compared with the modified Cam Clay model used in the previous studies (Indraratna et al. 1992, Liu et al. 2012, Yan et al. 2012, Chiou and Wei 2021), the additional parameters, such as creep coefficient $C_{\alpha e}$, initial bonding ratio χ_0, absolute rate of bond degradation ξ, relative rate of bond degradation ξ_d, need to be determined in the ANICREEP model. According to Yin et al. (2011), the initial bonding ratio χ_0 can be obtained by the oedometer test or shear vane test between the undisturbed and remolded soil; the absolute rate of bond degradation ξ and relative rate of bond degradation ξ_d can be determined based on the curve fitting from one-dimensional and isotropic compression test. The interparticle bonding and debonding effects in simulations are ignored in this study.

$C_{\alpha e}$ is the key parameter for the applicability of elasto-viscoplastic constitutive model in practical engineering, which can be determined by the oedometer test. Taking the massive experimental data collected by Jin et al. (2019), the relationship between the creep coefficient, $C_{\alpha e}$, and void ratio, e, of various types of clay is plotted in Figure 3-5. The $C_{\alpha e}$ is ranged from 0.001 to 0.02, except from some scattered data up to 0.023. In the parametric analysis part, the benchmark value of $C_{\alpha e}$ can be adopted as 0.01, estimated by the average $C_{\alpha e}$ of each clay layer in the verification case study.

Comparing with the benchmark value, $C_{\alpha e}$ =0.001 and $C_{\alpha e}$ =0.02, represent the lower and higher creep effect, respectively, elicited from Figure 3-5.

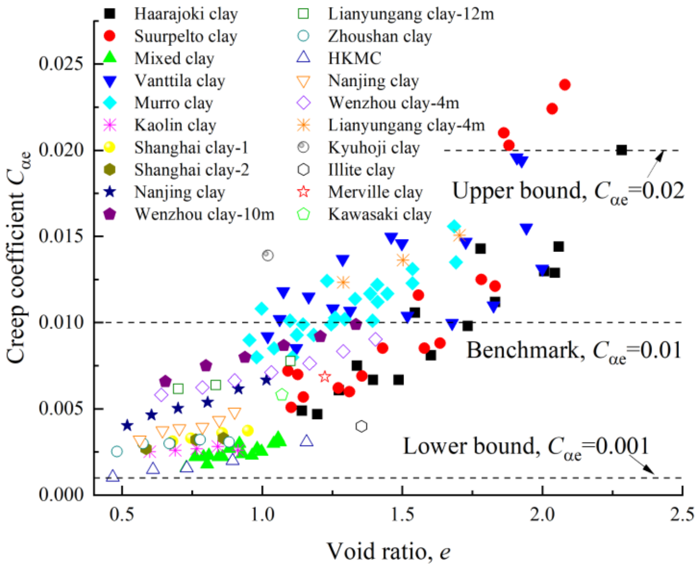

Figure 3-5 Creep coefficient of various clays

Due to the convergence problem during calculation, a very low value (i.e., 1% of the benchmark $C_{\alpha e}$) of $C_{\alpha e}$ is considered as the case without creep rather than directly setting $C_{\alpha e} = 0$ following Wu et al. (2020). For comparison, the $C_{\alpha e} = 0.00001$ (0.1% of the benchmark $C_{\alpha e}$) is selected to conduct the sensitivity analysis to verify the reliability of the no creep condition, as shown in Table 3-2.

Table 3-2 Values of creep coefficient

Influencing parameter	**Value**
Creep coefficient, $C_{\alpha e}$	0.00001 (sensitivity analysis), 0.0001 (no creep), 0.001, 0.01 (benchmark), 0.02

Other parameters, such as the saturated unit weight γ, swelling index κ, compression index λ, slope of critical state line in p'-q (mean effective stress - deviatoric stress) plane M, elastic modulus E are following the field measured typical soft clay adopted by Indraratna et al. (1992). The overconsolidation ratio OCR, coefficient of earth pressure K_0, Poisson’s ratio v, initial void ratio e_0 are obtained based on the interpretation of field measured data in Indraratna et al. (1992). The details of parameters for the verification case are summarized in Table 3-3.

Table 3-3 Parameters of soft clay and pile in parametric analysis model (following Indraratna et al. (1992))

	Depth m	γ kN/m^3	κ	λ	M	e_0	k (10^{-4}) m/day	OCR	K_0	v	$C_{\alpha e}$	E kN/m^2
Soil												
Soft clay	0-30	16.7	0.063	0.323	0.98	1.55	9	1	0.6	0.3	See Table 3-2	-
Pile												
Pile	0-25	14.7	-	-	-	-				0.3	-	30×10^6

3.3 Parametric analysis results

3.3.1 Creep effect on settlement

The development of ground settlement at point A (1m away from pile center line) with time is shown in Figure 3-6. The larger settlement is observed under higher creep effect, as expected. The settlement exceeds 3.7 m when $C_{\alpha e} = 0.02$, which is more than triple the results calculated without creep. In addition, the relationship between vertical strain ε_{yy} and vertical effective stress (log scale) $\log\sigma'_{yy}$ at point A with various $C_{\alpha e}$ is also depicted in Figure 3-7. The creep effect is observed compared with no creep. Greater $C_{\alpha e}$, is associated with a higher creep strain rate, resulting in a more significant creep behavior. Two tangent lines are utilized in Figure 3-6 to estimate the consolidation rate following Casagrande’s method (Casagrande 1936). As the figure demonstrates, consolidation rate of soft soil layer decreases with the increase of $C_{\alpha e}$. Furthermore, it should be noted that this method is used to reflect the creep effect on consolidation rate rather than indicating the time when creep occurred. Through the sensitivity analysis, it concludes that $C_{\alpha e} = 0.0001$ (1% of the benchmark $C_{\alpha e}$) has the same results compared with $C_{\alpha e}$ =0.00001 (0.1% of the benchmark $C_{\alpha e}$), indicating that a further reduction in creep coefficient does not affect the settlement results. Therefore, it is reasonable to choose the 1% of benchmark $C_{\alpha e}$ to represent the no creep condition.

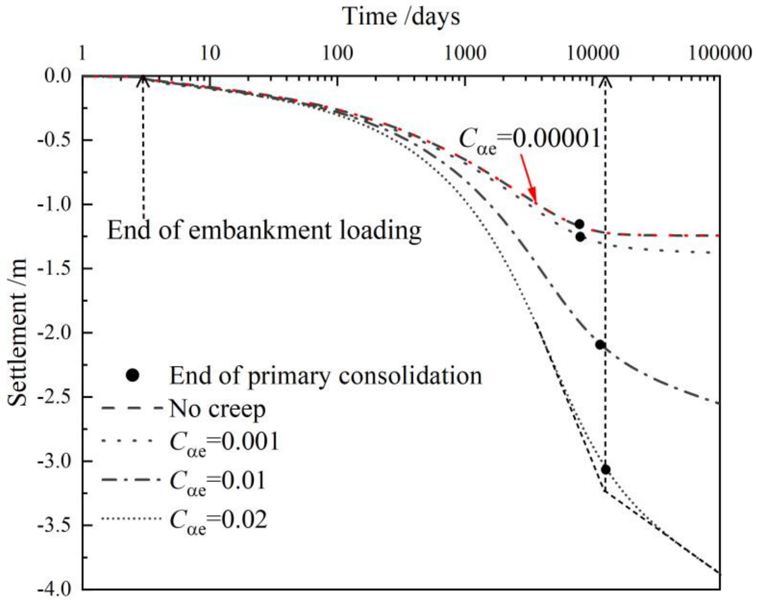

Figure 3-6 Development of ground settlement with various creep parameters versus time (No creep: 1% of the benchmark $C_{\alpha e}$)

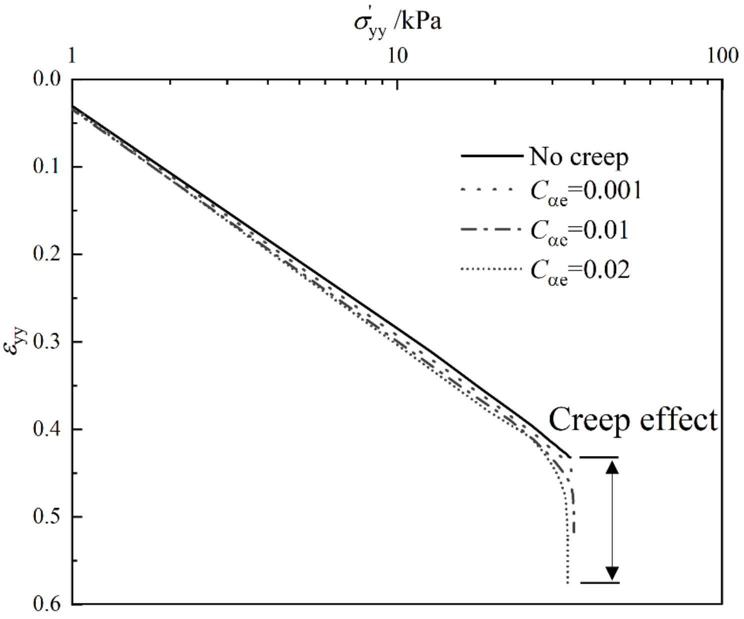

Figure 3-7 The relationship between vertical strain ε_{yy} and vertical effective stress $\log\sigma'_z$ with various $C_{\alpha e}$

3.3.2 Creep effect on excess pore pressure

Point B in Figure 3-4 is selected to observe the change in excess pore pressure (Δu). Figure 3-8 reflects the calculation results of Δu over time with and without creep. There shows a significant increase in Δu after the end of embankment load due to the creep effect compared with the calculation results excluding creep. This increase in Δu is due to the drainage of water from micropores in the microstructure into the macrostructure (Yin et al. 1994). As for the higher creep case, when consolidation begins, increasing rate of Δu induced by plastic volumetric strain on account of creep effect is higher than the decreasing rate of Δu due to dissipation, and hence the Δu shows the increasing trend. When the creep induced increasing rate of Δu is lower than the decreasing rate of Δu during the consolidation process, the Δu reaches the peak value and then gradually decreases until being totally dissipated.

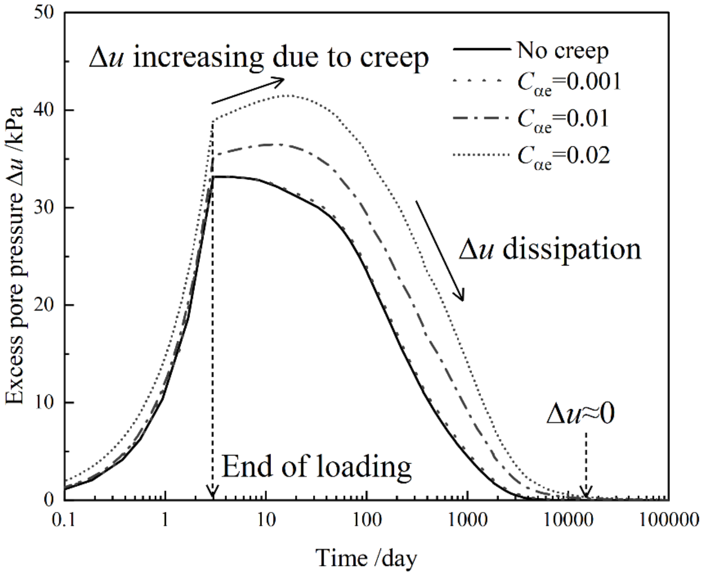

Figure 3-8 The changing of excess pore pressure over time at point B

3.3.3 Creep effect on negative skin friction

The creep effect on the development of dragload and skin friction along the pile with consolidation time up to 50 years is investigated and the results are presented in Figure 3-9. As expected, with the increasing of consolidation time, the dragload and NSF continue increasing and a higher dragload is observed with a greater creep coefficient. The fully mobilized NSF reveals the approximately linear variation with depth on account of the linear increase in vertical effective stress in this study.

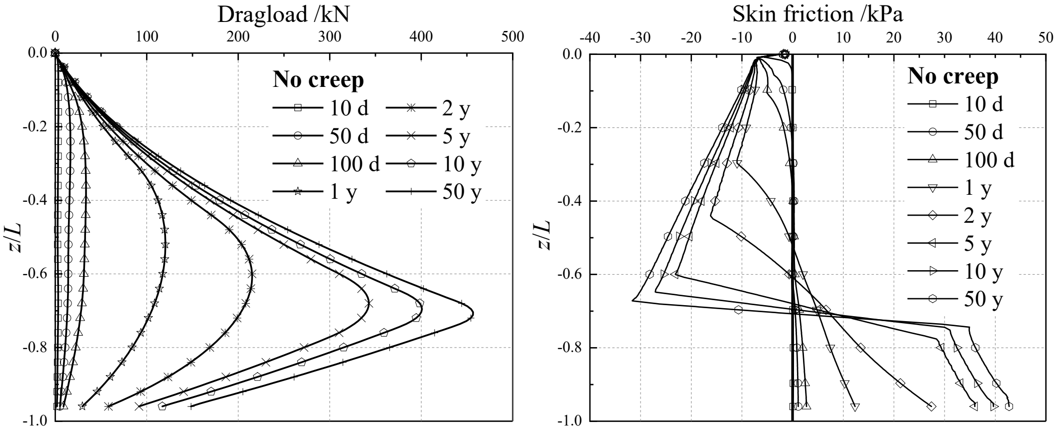

(a) No creep

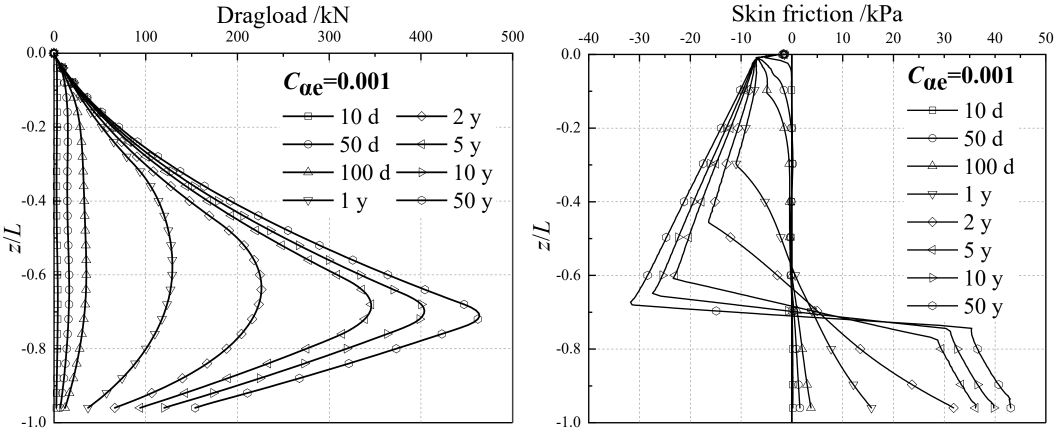

(b) $C_{\alpha e}$=0.001

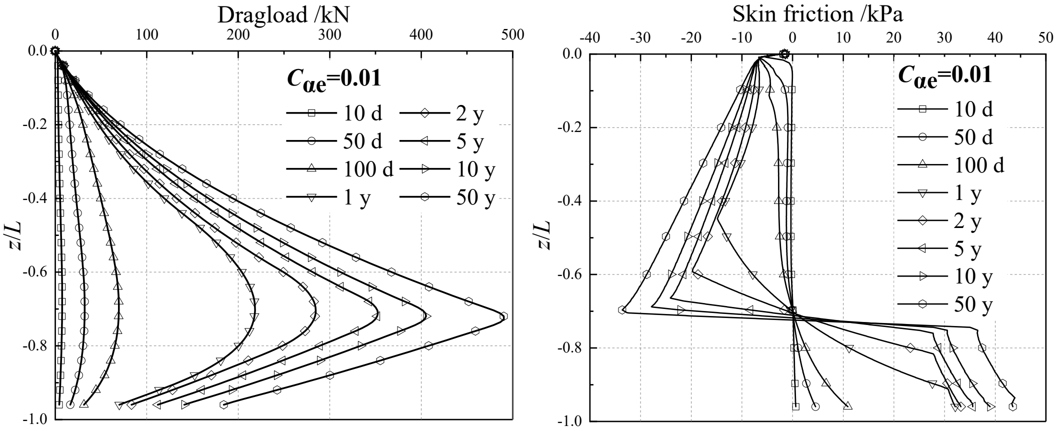

(c) $C_{\alpha e}$=0.01

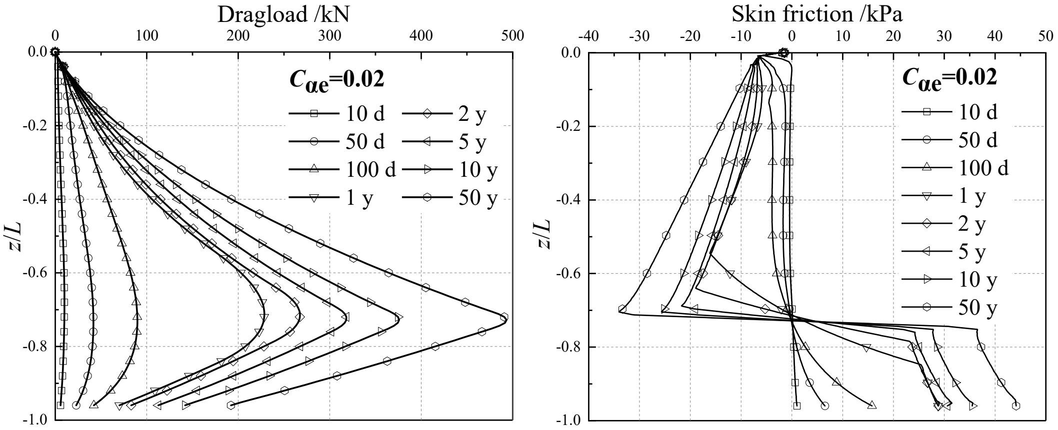

(d) $C_{\alpha e}$=0.02

Figure 3-9 Distribution of dragload and negative skin friction with time: (a) no creep; (b) $C_{\alpha e}$=0.001; (c) $C_{\alpha e}$ =0.01; (d) $C_{\alpha e}$ =0.02. ('d' and 'y' represent days and years, respectively)

In order to study the creep effect on NSF with consolidation, the dimensionless time T_{Uc} is used, in which the subscript U_c represents the degree of consolidation. For example, $T_{Uc}=1$ indicates the time when primary consolidation ($U_c=100\%$) is reached. When $0 \leqslant T_{Uc} \leqslant 1$ denotes the time period in primary consolidation, $T_{Uc}>1$ indicates the time in "secondary consolidation". A relationship between the normalized dragload

$P/P_{\mathrm{Tuc}=1}$ and T_{Uc} with or without creep is established, as shown in Figure 3-10, where P denotes the dragload at the NP, $P_{\mathrm{Tuc}=1}$ signifies the dragload after full dissipation of excess pore pressure.

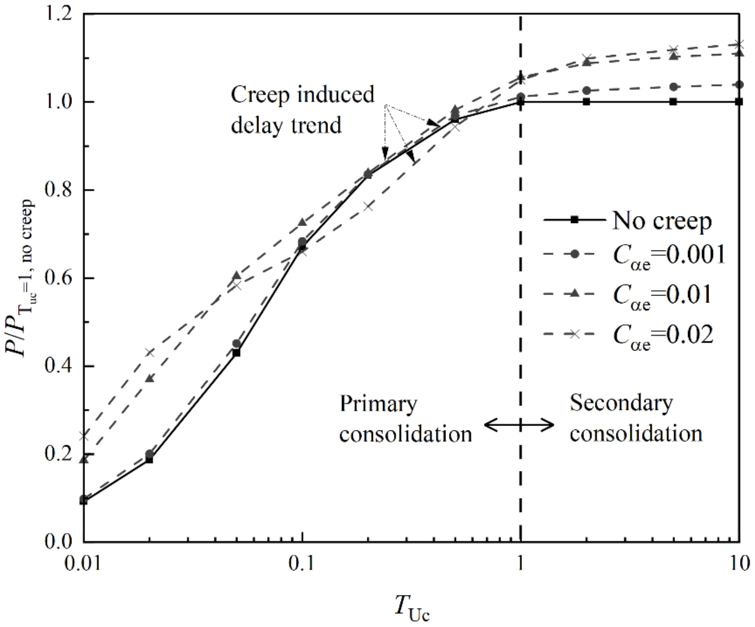

Figure 3-10 Changing of dragload with consolidation degree with or without creep

For the case where the creep effect is ignored, the dragload, P increases with time during the primary consolidation and then becomes stable. Whereas, for the cases considering creep, there will still be an increase in P due to the on-going settlement caused by creep. At the initial stage of consolidation, higher P is observed with the increase of creep coefficient. During the middle period of consolidation, the lower increasing rate of P is observed compared with no creep case, as well as a significant delay in P increment with higher creep effect. This phenomenon is mainly attributed to the creep induced excess pore pressure as explained in the previous section, which decreased the effective stress around the pile. According to the Coulomb friction interface model adopted in this study, the decrease of normal contact effective stress reduces the shear force at clay-pile interface. At the later period of consolidation, a higher increasing rate of P re-appears with a higher creep coefficient.

In practice, the effective stress related β method (Johannessen and Bjerrum 1965, Burland 1973) can be used to calculate the skin friction along the pile as follows:

$$f_{\mathrm{s}} = \beta\sigma_v' \tag{3-18}$$

where f_{s} is the shaft friction and σ_{v}' is the effective vertical stress. The dragload at the NP can be calculated based on the following equation:

$$P_{\text{drag, NP}} = \pi D\int_0^{L_{\mathrm{NP}}} f_s dz \tag{3-19}$$

where L_{NP} and D are the depth of the NP and the pile diameter, respectively. Therefore, the back-analyzed β can be calculated during the primary and secondary consolidation periods.

Figure 3-11 illustrates the development of the dimensionless β value ($\beta/\beta_{\text{Tuc=1, no creep}}$) where $\beta_{\text{Tuc=1, no creep}}$ is the back-calculated value after primary consolidation ignoring creep. At the beginning of consolidation, the no creep case shows the higher β value compared with creep cases because of the lower descending rate of the NP, where the effective stress is relatively low. With the development of consolidation, the β value increases until the end of primary consolidation. Similar findings were reported in both field tests (Indraratna et al. 1992, Hong et al. 2015) and centrifuge tests (Ng et al. 2008, Lam et al. 2013). When considering creep, a higher dimensionless β value is obtained, which increases to 1.05 after primary consolidation and to 1.13 when T_{uc}=10 for the case with the biggest creep coefficient.

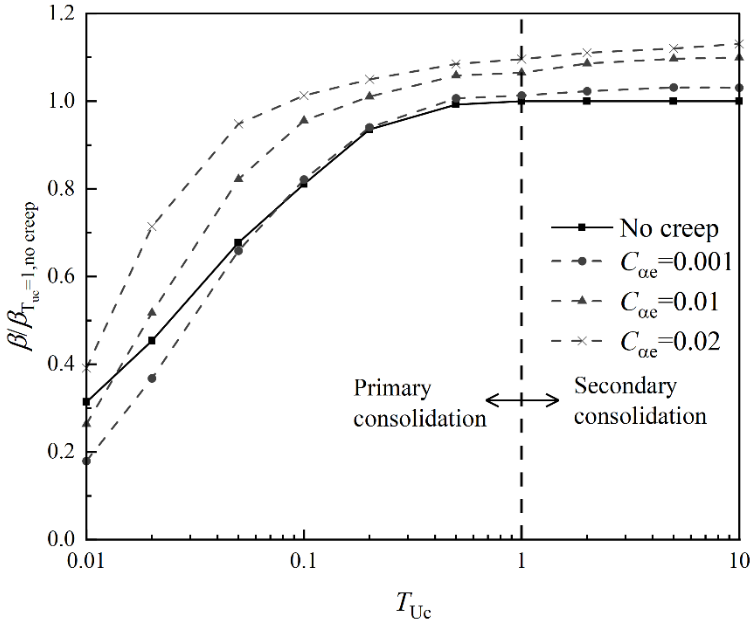

Figure 3-11 Change in dragload with consolidation degree with or without creep

3.3.4 Creep effect on neutral plane

The position of NP describes the depth where soil and pile settle equally, which is also the location where the maximum dragload is generated along the pile. The variation of NP position with consolidation time is inferred from skin friction as shown in Figure 3-12. For convenience, the NP depth is expressed as normalized depth L_{NP}/L_0, where the L_{NP} is the depth from the NP to the soil surface, L_0 is the pile embedded length. Observably, following the full dissipation of excess pore pressure, the NP position is stable in both the no creep and creep cases. Therefore, in the results, the study focused on NP variation in primary consolidation.

The variation tendency of NP position can be generally divided into two phases, namely Phase 1 and Phase 2. For the no creep case, in Phase 1, there is an upward trend in L_{NP}/L_0, the value of which reaches 0.64 within 10% degree of primary consolidation. In Phase 2, the value of L_{NP}/L_0 shows steady upward, which rises to 0.70 at the final stage. For the creep cases, a sharp increase in the NP position at the initial time can be found in Phase 1. The inflection time $T_{uc,s}$ (the definition is shown in Figure 3-13 and will be discussed later) also shows a great decrease with higher creep effect. In Phase 2, NP is much closer to a steady state but demonstrates a slight increase with time. Furthermore, an increase in creep coefficient shifts NP slightly downward.

For comparison, theoretical predictions of NP position based on different methods from the literature are presented in Figure 3-12. Alonso et al. (1984) developed a stress-transfer method to describe the interaction behavior between the pile and soil induced by NSF. The design chart for NP position with various conditions is proposed. The NP is located at L_{NP}/L_0=0.7, with zero pile toe resistance and no pile head loading. NAVFAC (1986) suggested that the value of L_{NP}/L_0 can be estimated as 0.75 if there is no available test data. Bowles (1997) presented a simple design method to locate the NP considering the surcharge load. The calculated NP is about 0.67. The Chinese national standard provided the empirical value for the NP in the light of pile tip surrounding soil. The suggested NP location L_{NP}/L_0 is 0.5-0.6 for the pile-tip soil in clay or silt.

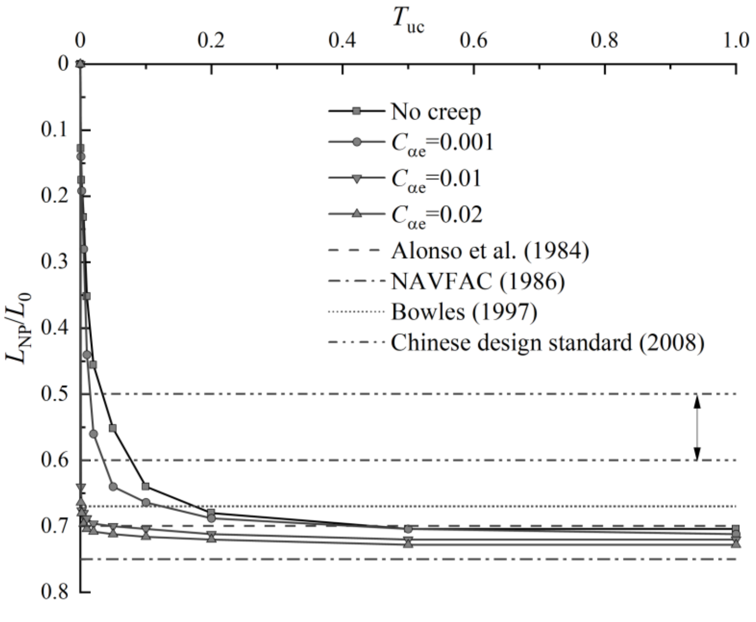

Figure 3-12 Relationship between the neutral plane position with time

It can be seen that the result provided by Alonso et al. (1984) shows consistency with the NP position ignoring creep, although it is a special case that neglects the toe resistance mobilization. Other empirical methods have yielded either overestimated or underestimated results, implying that these methods are uneconomical and conservative. These methods also failed to consider the time dependence of the NP. To address this issue, the exponential function to describe the variation of NP position with time was proposed by Zhang et al. (2022) and validated by field monitoring results. The prediction results show a higher correlation relationship compared with the hyperbolic model provided by Cao et al. (2014). Therefore, the improved exponential function is applied to analyze the creep effect on the NP position, as shown below:

$$\frac{L_{\mathrm{NP}}}{L_0} = a\left(1 - e^{-kT_{uc}^{b}}\right) \tag{3-20}$$

where L_{NP}/L_0 and T_{uc} are the normalized NP position and consolidation time as mentioned above; meanwhile, a, b and k are the fitting controlling factors, where a is the NP value at the steady state, k and b control the variation rate of the NP. Based on the variation rate of NP, Phase 1 and Phase 2 can be divided by $T_{\mathrm{uc,s}}$, where θ is half of the angle composed by the intersection of asymptotic line at the initial and end of the fitting curve, as shown in Figure 3-13.

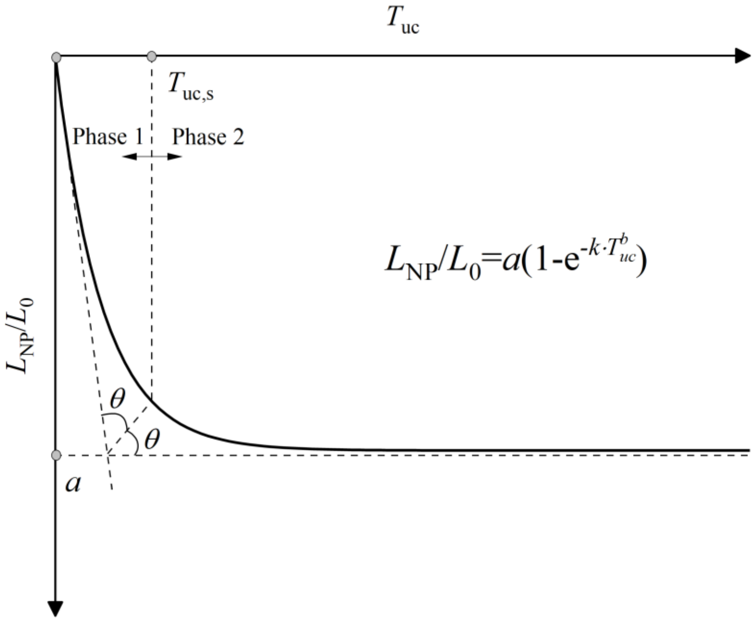

Figure 3-13 Exponential prediction model for NP position.

Figure 3-14 reveals the fitting results of the exponential model, as well as the fitting parameters and correlation coefficient, R^2. The adopted model is able to accurately predict the NP position with time considering creep. Nevertheless, these fitting parameters are controlled by site conditions, such as surcharge load, pile head loading, the properties of consolidation, end bearing layer, creep effect, pile size and pile-soil interface friction, etc.. Furthermore, the site condition varies from one project to another. Future work is needed to find a more sophisticated method to consider the coupling effect of all influencing parameters.

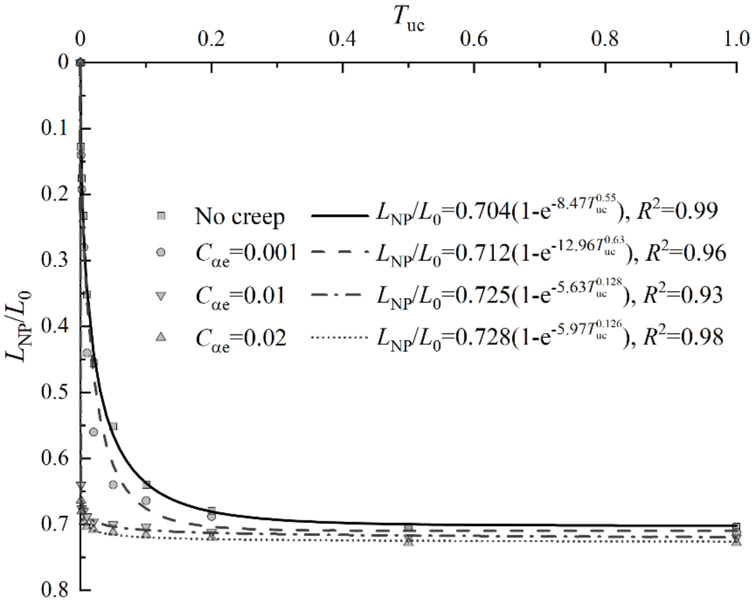

Figure 3-14 Fitting results of the exponential model

3.4 Summary

In this chapter, an elasto-viscoplastic model adopting an enhanced time integration algorithm with higher calculation robustness was successfully implemented into ABAQUS through user subroutine UMAT. This model was first employed to simulate a known field test with the verification. Then, an in-depth investigation of the creep effect on the NSF and NP in the primary and secondary consolidation period was thoughtfully conducted. The resulting detailed findings and conclusions are drawn as follows:

(1) When compared with the non-creep case, it shows a higher dragload as well as back-calculated β value after primary consolidation when considering creep, because more soil settlement results in higher relative displacement between the soil and pile, which further mobilizing the NSF.

(2) The creep induced delay trend on dragload is observed with higher creep effect during primary consolidation procedure. In line with the Coulomb-friction interface law, the skin friction is proportional to normal effective stress, and therefore, the generation of extra excess pore pressure caused by creep deformation impedes the development of effective stress in the clay-pile interface, leading to the lower dragload.

(3) The value of normalized NP position (L_{NP}/L_0) starts at 0 and increases to around 0.7 after consolidation when ignoring creep, which is similar to the special case calculated by Alonso et al. (1984). The location of NP moves downward when considering creep, though a limited downward trend is observed as the increasing of creep effect. A sharp descent of the NP position can be observed at the beginning of consolidation at a higher level of creep effect of the surrounding soil.

(4) The current empirical formula can neither predict the NP position well nor consider its time dependency. In contrast, an improved exponential prediction model with three controlling parameters is presented and applied to predict the variation of NP position with time considering creep effect.

In this section, the pile driven procedure is ignored. Pile driven causes significant disturbance within the soil around the pile shaft, which leads to the changes of stress state in the surrounding soil. The generation of the excess porewater pressure during pile penetration may take long time to entirely dissipate. Pile penetration effects on NSF are discussed in Chapter 5.

CHAPTER 4 DEVELOPMENT OF NEGATIVE SKIN FRICTION ON PILE GROUP

4.1 Introduction

The mobilization of negative skin friction (NSF) imposes a detrimental load, known as dragload, on piles by reducing their axial bearing capacity and inducing additional settlement. The adoption of sacrificial piles arranged in a group configuration can reduce this dragload. However, the understanding of NSF mobilization in pile groups, particularly in the context of soft soil creep, remains limited. The objective of this section is to examine the creep effect on the group shielding of dragload and to quantify the contribution of sacrificial piles to the group effect for various soil parameters and pile spacing. This section is organized as follows. First, an elastic viscoplastic model with a cutting plane algorithm is implemented in the finite element package ABAQUS to account for the time dependency of soft soil. Next, a quarter three-dimensional numerical model is established and verified through a well-documented centrifuge case study. An extensive numerical investigation is subsequently conducted to examine the group effect on dragload in light of pile spacing, end-bearing soil stiffness and creep effects.

4.2 Finite element modeling

4.2.1 Centrifuge test

Ng et al. (2008) conducted the centrifuge test to investigate the shielding effects on the NSF and dragload for the pile groups. An instrumented center pile with a diameter

D of 1.2 m (all scales mentioned in this section refer to the prototype size) was surrounded by eight sacrificial piles, each with a diameter *d* of 0.6 m, forming a 3×3 pile group. The pile spacings were 5.0 *d* and 6.0 *d* for different test configurations. Both the center pile and sacrificial piles were embedded in the 17.7 m thick saturated soft clay layer, with the group's pile tip located 0.3 m above the bottom stiff sand stratum. All model piles were made from aluminum tubes with a Young's modulus of 70 GPa. Leighton Buzzard sand and Speswhite China clay were utilized to form the bottom sand layer and soft soil layer, respectively. After the clay reached an undrained shear strength of 18 kPa, boreholes were drilled using augers to install the model piles in 1g conditions. Subsequently, sand fill was rained on the top of the clay layer to generate an equivalent surcharge loading of 45 kPa at 60 g. During the test, the centrifuge was spun up to 60g, and the variations in the excess porewater pressure, soil surface settlement, dragload on piles were continuously monitored until the clay achieved a consolidation degree of 90%. Further details of the experimental program and setup can be referred to in Ng et al. (2008).

4.2.2 Numerical model

The development of NSF over time in the aforementioned centrifuge test history is studied numerically by the FE package ABAQUS (Dassault Systèmes 2020). Owing to symmetry, only a quarter of the whole mesh is required in the 3D analyses to save computational cost. For simplicity, the piles are assumed to be wished-in-place, neglecting the effects of the pile installation (Liang et al. 2023). The schematic and FE mesh of the studied numerical centrifuge model are shown in Figure 4-1.

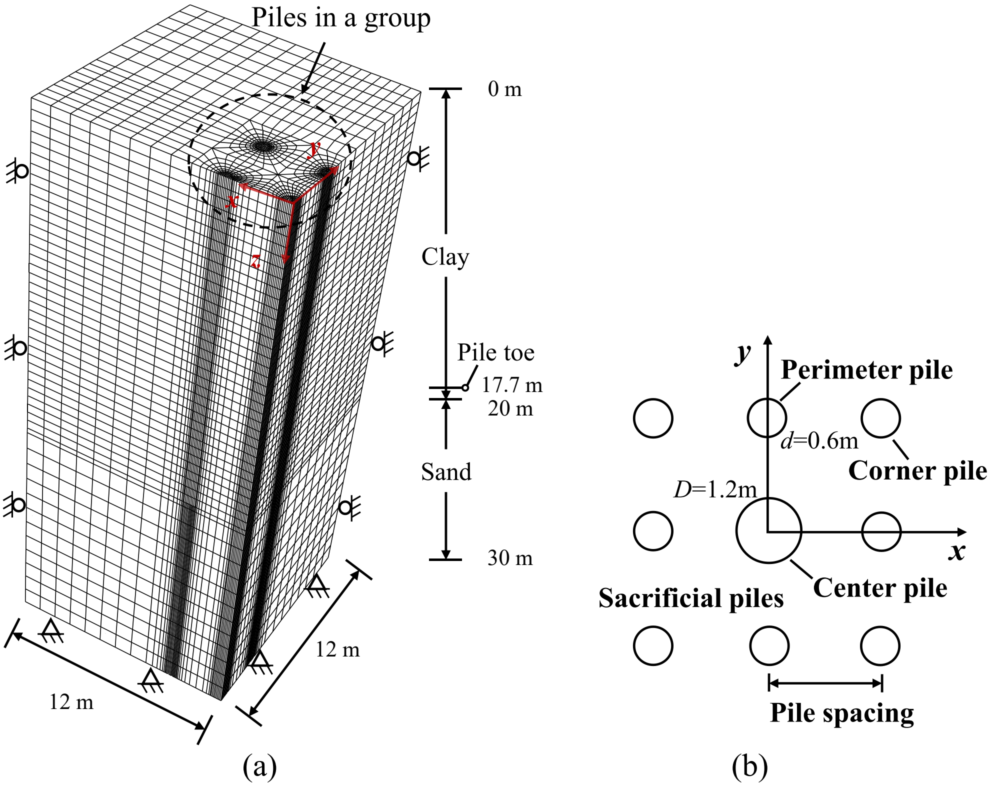

Figure 4-1 Schematic representation of the quarter centrifuge test verification model for the 5 *d* spacing (a) mesh details; (b) pile positions in a group (33855 elements for soil and 5705 elements for pile)

The minimum distance from the pile to the soil boundary is more than 10 times the pile diameter, which is considered sufficient enough to minimize the boundary effects (Sun et al. 2015, Liang et al. 2024). The eight-node hexagonal elements (C3D8 for pile and sand and C3D8P, which includes porewater pressure as a degree of freedom, for fully saturated clay) are adopted in the coupled mechanical-flow consolidation analysis. The mesh is refined near the pile and coarser farther away to mitigate stress concentration effects and enhance the calculation efficiency. The lateral and bottom boundaries of the model are assigned roller and the fixed conditions, respectively. The free drainage boundaries are placed at the top of the clay and sand layers. For comparison, an additional analysis is conducted adopting 20-node elements with a dense mesh for a pile group case with a pile spacing of 5.0 *d* under the same conditions. The results indicate that higher order elements and a dense mesh yield essentially the same outcomes as the eight-node proper mesh reported in this study, confirming mesh and element convergence in the present model.

The frictional behavior between soil and pile is described by the Coulomb friction law, where shear stress is proportional to the relative shear displacement. Once the threshold displacement is reached, shear stress stabilizes. The two key governing parameters are the frictional parameter, μ=0.3 and threshold displacement, δ=5 mm (Ng et al. 2008). In the model verification procedure, the geostatic step is first calculated to establish the initial stress of the soil stratum. Following geostatic equilibrium, surcharge loading is applied to the top surface of the clay in the mechanical-consolidation coupled analysis step. During the consolidation stage, excess porewater pressure dissipates within the assigned time period.

The isotropic linear elastic model is applied to simulate the pile and end-bearing sand layer, while the elasto-viscoplastic ANICREEP model with an enhanced time integration scheme is adopted to represent the soft soil stratum. Comparing with the modified Cam Clay soil model (MCC) used in the previous pile-soil interaction simulations focusing on the NSF development (Liu et al. 2012, Yan et al. 2012, Chiou and Wei 2021), the additional parameters, such as creep coefficient $C_{\alpha e}$, initial bounding ration χ_0, relative rate of bound degradation ξ and relative rate of bond degradation ξ_d, need to be determined in the ANICREEP model. The detailed explanation and determination of these parameters are given in Section 3.2. Although the structure of clays used in the selected centrifuge study was not reported, Speswhite Kaolin clay which was adopted in the calibrated centrifuge test is known to have low sensitivity (Cao et al. 2002). Additionally, centrifuge tests are idealized for homogenous soils strata, which justifies the omission of interparticle bonding and debonding effects in the simulations (i.e., $\chi_0 = \xi = \xi_d = 0$).

The parameter $C_{\alpha e}$ is essential for the practical applicability of the elasto-viscoplastic constitutive model and can be determined through the oedometer tests. However, no $C_{\alpha e}$ data were reported in previous centrifuge tests records. Jin et al. (2019) found that $C_{\alpha e}$ is highly correlated with void ratio, plasticity index and liquid limit, and proposed a reliable prediction method, which is adopted in this study, as shown in Eq. (4-1):

$$\ln(C_{\alpha e}) = \left(0.055\frac{1}{w_L^2 I_p} - 0.107\frac{1}{I_p} + 0.272\left(\frac{w_L}{I_p}\right)^2\right)e - 2.222 \tag{4-1}$$

where e is the void ratio, I_p is the plasticity index and w_L is the liquid limit.

Other parameters, such as the gradient of the swelling line, κ, the slope of the compression line, λ, initial void ratio, e_0, slope of the critical state line, M, Poisson's ratio, v, saturated unit weight, γ, elastic modulus, E and lateral earth pressure coefficient at rest, K_0 are the identical to those reported by Ng et al. (2008), where the soil parameters were obtained through the laboratory tests, including water content measurements, oedometer tests and triaxial tests. The permeability coefficient, k, for Speswhite Kaolin clay is estimated following Cao et al. (2002) due to the k was not reported by Ng et al. (2008). A comprehensive overview of the model parameters is provided in Table 4-1.

Table 4-1 Summary of parameters for centrifuge test history

Material type	Depth (m)	γ (kN/m^3)^a	κ^a	λ^a	M^a	e_0^a	k (×10^{-4} m/day)^b	K_0^a	ν^a	$C_{\alpha e}^c$	E (kPa)^a
Soil											
Clay	0-20	16.3	0.012	0.14	0.98	1.6	4.5	0.58	0.35	0.01	-
Sand	20-30	19.4	-	-	-	-	-	0.39	0.3	-	1.2×10^5
Pile											
Pile	0-17.7	27	-	-	-	-	-	-	0.35	-	7×10^7

[a] The same parameter values were adopted by Ng et al. (2008). The soil parameters were obtained through the laboratory tests, including water content measurements, oedometer tests and triaxial tests.

[b] Following Cao et al. (2002).

[c] Estimated using Eq. (1). The liquid limit, w_L and plasticity index, I_p for Speswhite Kaolin clay are estimated to be 0.58 and 0.3, respectively (Holtz et al. 1981).

4.2.3 Simulation results

The FE simulation results for pile groups with 5 *d* and 6 *d* spacing are computed and compared with historical data, as shown in Figure 4-2. For clarity, the depth, z, is normalized as z/L, where L represents the pile embedded length within the compressible soils. The calculated dragload generally captures the variation of measured dragload with depth and accurately reflects the NP position in both cases. The pile group with a 5 *d* spacing exhibits a lower magnitude of dragload compared to the 6 *d* spacing, with both cases predicting a NP position at approximately 0.77 L. However, the calculated maximum dragload (i.e., dragload at the NP position) slightly underestimates the test results. This discrepancy may be attributed to the pile installation process in centrifuge tests, which generates excess porewater pressure and prolongs the time required to achieve the consolidation degree of 90%. Additionally, pile installation distorts the adjacent soil. Results from Ng et al. (2008) are also plotted in Figure 4-2 for comparison. Since the numerical analysis by Ng et al. (2008) assumed the completion of consolidation through the drained analysis, both the NP position and the maximum dragload were overestimated.

To analyze the creep effect on the mobilization of the NSF, the case without considering the creep effect is also conducted. The results indicate that neglecting the creep effect can yield an underestimation of both the maximum dragload and the NP position, potentially resulting in a risky design for the pile group. This underscores the necessity of accounting for soft soil creep when estimating dragload magnitude and NP position, as even a few millimetres of relative displacement can fully mobilize the NSF, as previously discussed.

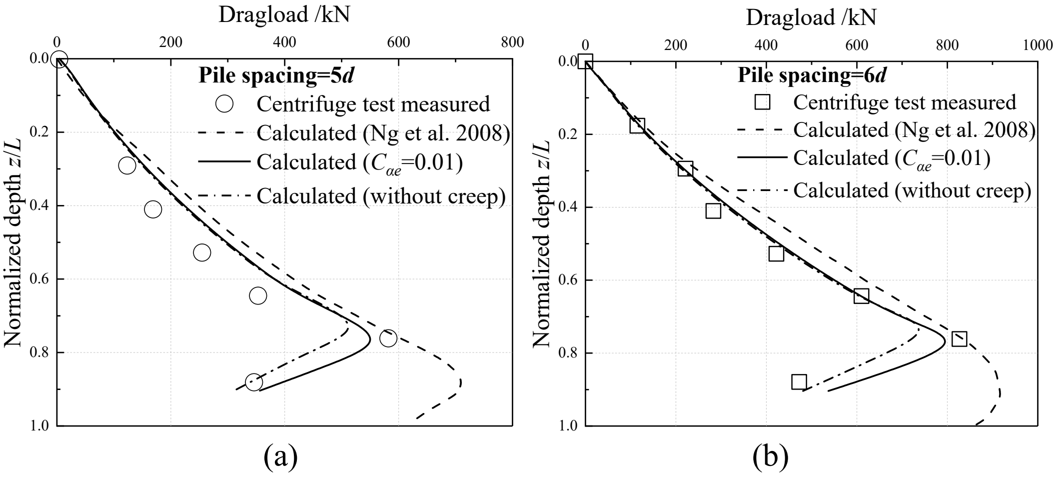

Figure 4-2 Comparisons of the numerical calculated and centrifuge measured dragload with: (a) pile spacing=5*d*; (b) pile spacing=6*d*

4.3 Model for parametric analysis

Based on the comparison results discussed earlier, the established 3D quarter verification model effectively captures the NSF of the center pile within a pile group. Consequently, further investigations into the creep effects, pile spacing and elastic modulus of the end-bearing layer on NSF within pile groups are pursued by constructing a simplified numerical model for parametric analysis. This simplified model, derived from the aforementioned model, is shown in Figure 4-3(a). A slight modification has been made that the end-bearing layer has a thickness of 12.3 m and the clay strata has a thickness of 17.7 m, indicating the pile toe is located at the top sand layer, while all other parameters remained unchanged. Furthermore, the single pile model is also established and calculated for comparison, as shown in Figure 4-3(b).

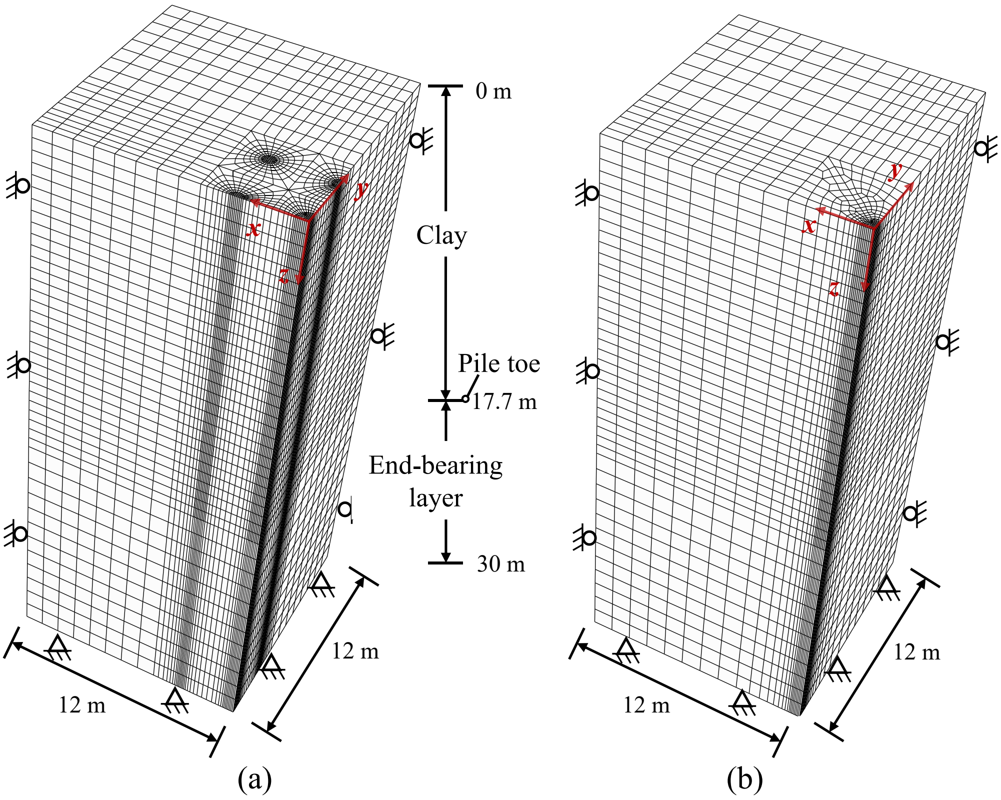

Figure 4-3 Schematic representation for the parametric study model: (a) pile group; (b) single pile

The extensive experimental dataset on the relationship between the $C_{\alpha e}$ and e, collected by Jin et al. (2019), is shown in Figure 3-5. These data indicate that the $C_{\alpha e}$ typically ranges from 0.001 to 0.02, with some scattered values extending up to 0.023. Therefore, it is reasonable to adopt a benchmark value of $C_{\alpha e}$ as 0.01, while $C_{\alpha e}$=0.02 represents a higher creep effect and $C_{\alpha e}$=0 indicates no creep, as illustrated in Figure 3-5. In addition to $C_{\alpha e}$, the elastic modulus of the end-bearing layer, E_b, also influences the pile-soil relative displacement, further affecting the dragload development. Therefore, E_b, which ranges from 1e4 to 1e5 kPa and represents an end-bearing layer composed of stiff clays to dense sands, is included in the parametric analysis (Canadian Geotechnical Society 2006). Additionally, pile spacing varies from 3 *d* to 7 *d* and Table 4-2 summarizes the parameters used in the parametric study.

Table 4-2 Influencing parameters used in the parametric study

Influencing parameter	Value
Creep coefficient, $C_{\alpha e}$	0 (no creep), 0.01 (benchmark), 0.02
Pile spacing, *S*	3 *d*, 4 *d*, 5 *d*, 6 *d*, 7 *d*
Elastic modulus of end-bearing layer, E_b (kPa)	1e4, 2e4, 5e4, 1e5

4.4 Parametric analysis and results

4.4.1 Settlement and excess porewater pressure

Figure 4-4 shows the temporal development of ground settlement at point with coordinates (12, 12, 0), representing the far-field ground settlement. As expected, the largest settlement occurs under higher creep effect. The settlement exceeds 0.5 m when $C_{\alpha e}$=0.02, more than four times the result calculated without considering creep. In addition to its significant impact on settlement, creep also influences the dissipation of excess porewater pressure, Δu. The change of Δu at monitoring point with coordinates (12, 12, 8.85) is selected to represent Δu variation of the far field middle clay layer, as depicted in Figure 4-5. A delayed dissipation of Δu is observed at the onset of consolidation following embankment loading, which is attributed to the creep effect, in comparison to the results from calculation excluding creep. Additionally, the consolidation rate of the soft soil layer decreases as $C_{\alpha e}$ increases. Yin et al. (1994), Zhu and Yin (2001) indicate that the plastic volumetric strain caused by creep can lead to an additional increase in Δu. This increase is more pronounced with higher values of $C_{\alpha e}$, contributing to an overall delay in Δu dissipation.

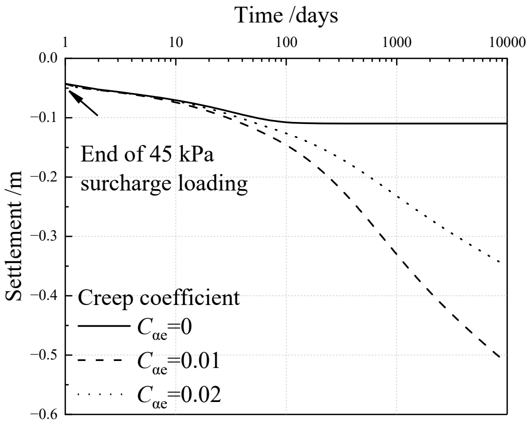

Figure 4-4 Development of ground settlement with various creep parameters versus time

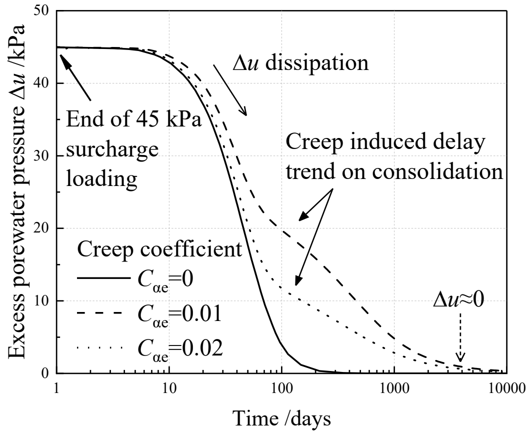

Figure 4-5 Changes in excess porewater pressure over time

4.4.2 Dragload development and group effect

The development of the dragload along the center pile for various pile spacings and E_b values at $C_{\alpha e}$=0.01 is presented in Figure 4-6, with the dragload for the single pile case included for comparison. The dragload is measured at the end of the primary consolidation (i.e., approximately 98% of Δu has dissipated). As shown in Figure 4-6(a), the single pile experiences the largest maximum dragload (i.e., dragload at the NP) compared to the pile group. An increasing trend in the maximum dragload is observed with larger pile spacings, as expected. A maximum 16% reduction in dragload is achieved at a pile spacing of 3 *d* compared to the single pile case. This finding indicates that smaller pile spacings of the sacrificial piles provide a better shielding effect, while larger spacings reduce this effect. The NP is consistently located at approximately 0.83 *L* for all cases, indicating that pile spacing does not influence the NP location. Similar NP position was reported by Indraratna et al. (1992), who identified an NP location of 0.84 *L* through field monitoring. The effective shielding depth, marked by a dashed line, highlights the dragload reduction below this depth due to the group shielding. Above this depth, the mobilized dragload in the pile group aligns with that calculated for a single pile. The effective shielding depth ranges from 0.58 *L* to 0.75 *L* for the pile spacing of 3 *d* to 7 *d*.

As the E_b value increases, the dragload becomes further mobilized and the NP positions shift downward until reaching the pile toe, as shown in Figure 4-6(b)-(d). This downward movement of the NP shows a transition of the pile from a friction pile to an end-bearing pile. The effective shielding depth nearly extends to the pile toe and the group effect becomes less pronounced with increasing bearing layer stiffness, even for the 3 *d* pile spacing. This behavior is attributed to the limited pile settlement under higher bearing layer stiffness and the full mobilization of NSF along the pile.

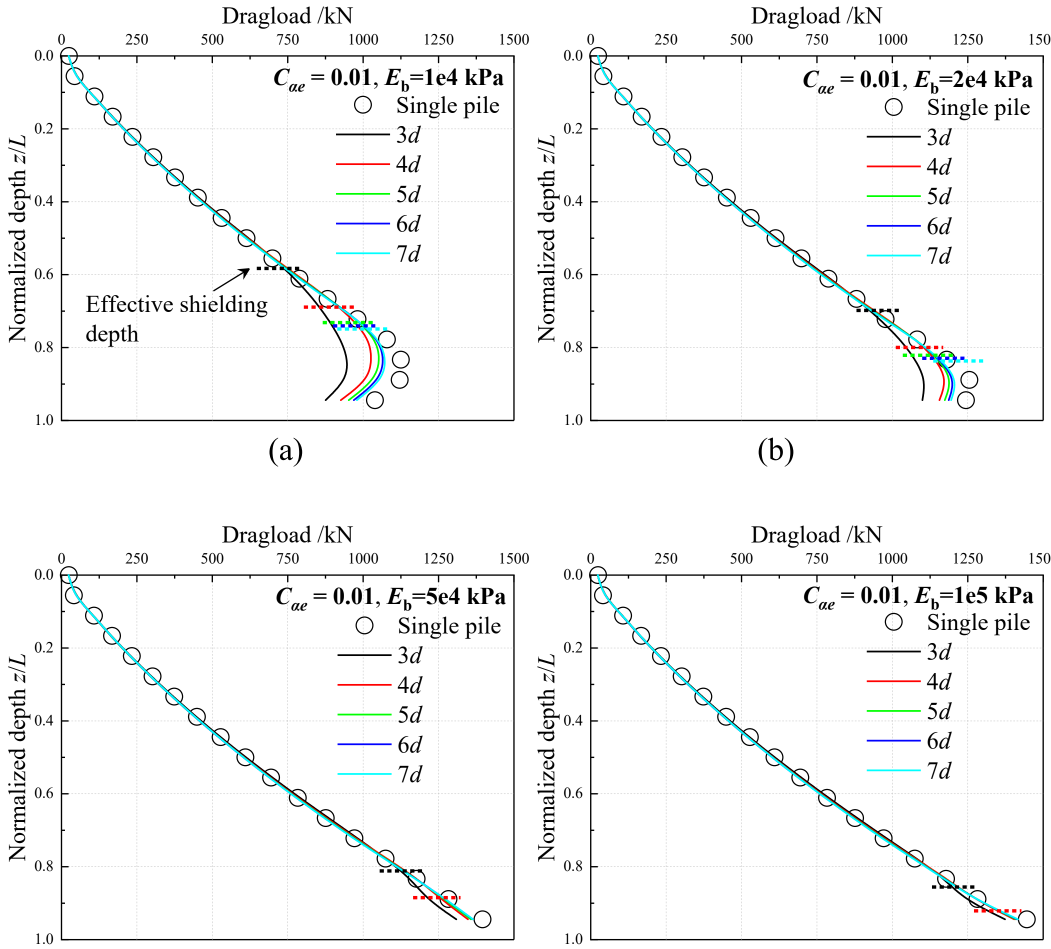

(a) (b)

(c) (d)

Figure 4-6 Variations in dragload with various pile spacing and end-bearing layer stiffness at $C_{\alpha e}$=0.01

To further evaluate the shielding on dragload within a pile group, the nondimensional parameter P_r is introduced in this study to quantify the group effect:

$$P_r = \left(P_{\max,s} - P_{\max,g}\right) / P_{\max,s} \tag{4-2}$$

where $P_{\max}$ represents the maximum dragload, and the subscript s and g denote a single pile and the center pile in a group, respectively. Therefore, $P_r = 0$ indicates no shielding, while P_r=1 represents perfect shielding on dragload. The variation of P_r with respect to $C_{\alpha e}$, S/d and E_b is presented in Figure 4-7. P_r decreases with increasing pile spacing due to reduced shielding by the pile group, as previously discussed. As the *S*/*d* increases up to 7, the sacrificial piles provided negligible shielding to the dragload of the center pile. Therefore, a 7*d* spacing can be recommended as the maximum shielding distance between the center and sacrificial piles.

However, the critical pile spacing proposed in this study differs from those reported in previous research (Koerner and Mukhopadhyay 1972, Thomas et al. 1998, Lee and Chen 2003). Koerner and Mukhopadhyay (1972) conducted small-scale tests on NSF development within pile groups under 1g conditions and identified a critical pile spacing of 2.5 *d*. This smaller spacing may result from the inability of 1g tests to replicate prototype stress levels accurately. Therefore, the results of such tests must be interpreted with caution, as they are difficult to extrapolate to field conditions. Thomas et al. (1998) investigated NSF in pile groups using centrifuge testing and reported a critical pile spacing of 3.5 *d*. In their study, surface settlement of 1.3 m occurred in an 18m-thick clay layer (dimensions are in full-scale), which was large enough to fully mobilize NSF, resulting in a relatively small critical spacing. A similar trend is also observed in the present study, where critical pile spacing decreases with increased soft soil creep effects due to greater soil settlement. Lee and Chen (2003) also conducted centrifuge tests on pile groups in clay and reported a critical spacing of 6 *d*. However, their tests involved a 5-pile configuration, differing from the 3×3 configuration used in this study. The smaller number of sacrificial piles led to reduced group effects, which in turn yielded a smaller critical pile spacing. A more detailed discussion on the mechanism of critical pile spacing is provided in Section 3.4, along with an illustration of vertical effective stress distribution within pile groups.

In cases where $C_{\alpha e}$=0, P_r ranges from 0.04 to 0.29 and decreases with increasing E_b when S/d is less than 4.5, while it increases with E_b when $S/d > 4.5$. Generally, the variation of P_r with E_b is not significant when $S/d > 4.5$. Similar findings were reported by Chow et al. (1990) and Lee and Ng (2004), who observed that the group effect on dragload is comparable for friction pile groups and end-bearing pile groups. However, these studies did not account for the creep effect of the soft soil. When $C_{\alpha e}$ increases to 0.01, P_r decreases to a range of 0.02 to 0.16 and gradually stabilizes once S/d exceeds 4. As E_b increases, P_r generally decreases to below 0.05, indicating a minimal shielding effect for the end-bearing piles with a higher creep coefficient. Similarly, as $C_{\alpha e}$ increases to 0.02, P_r further decreases to a range of 0.02 to 0.09. Additionally, the relationship between P_r and S/d can be fitted using an exponential function, as shown in Figure 4-7.

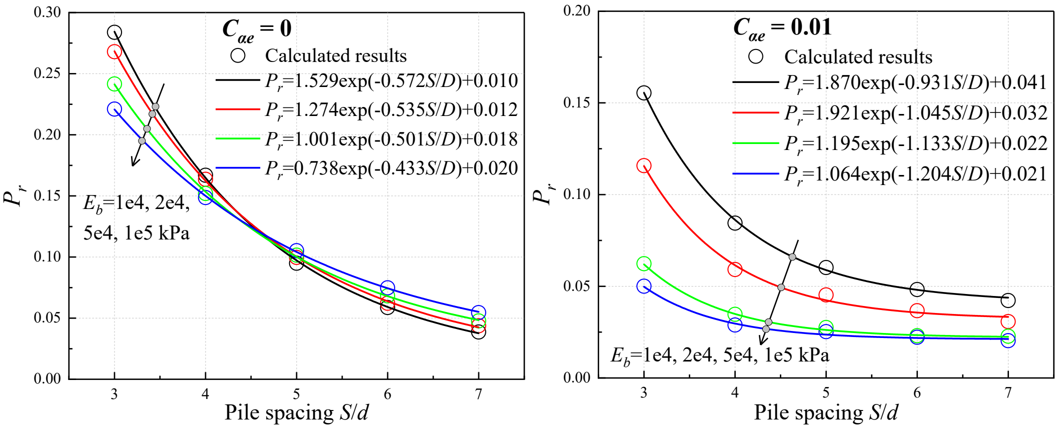

(a) (b)

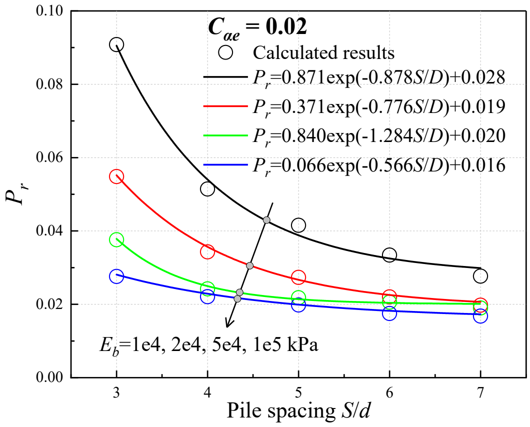

(c)

Figure 4-7 Shielding on dragload for the center pile: (a) $C_{\alpha e}$=0; (b) $C_{\alpha e}$=0.01; (c) $C_{\alpha e}$=0.02

Lee et al. (2002) performed numerical analyses and reported a P_r of approximately 0.3 with a pile spacing of 2.5 *d* and a P_r of 0.15 with a 5.0 *d* pile spacing in a 3×3 pile group. Shen (2008) conducted centrifuge tests with a pile spacing of 3.0 *d* and observed a P_r of approximately 0.14 in a 5-pile group (i.e., one center pile and four sacrificial piles) and 0.23 in a 3×3 pile group. The P_r values calculated in this study generally fall within these ranges. Furthermore, it is important to note that the P_r is influenced by various factors, including pile dimensions, installation methods, pile spacing, surcharge loading, pile configuration, soil conditions (e.g., soil stiffness and creep).

The coefficient $C_{\alpha e}$ significantly influences the pile-soil interaction behavior within pile groups. A higher $C_{\alpha e}$ leads to a lower P_r, primarily attributed to the creep-induced soil settlement. The group effect arises from the stress transfer from the inner soil to the surrounding piles, which constrains the settlement of the inner soil. However, creep increases the relative displacement between the pile and soil, Δs, as illustrated in Figure 4-8. Since the Coulomb friction is employed to simulate the pile-soil interaction, the shaft friction, f_s is proportional to Δs until the threshold displacement, δ is reached. A higher $C_{\alpha e}$ can induce excessive Δs, increasing f_s (NSF) of the center pile and thereby weakening the group effect.

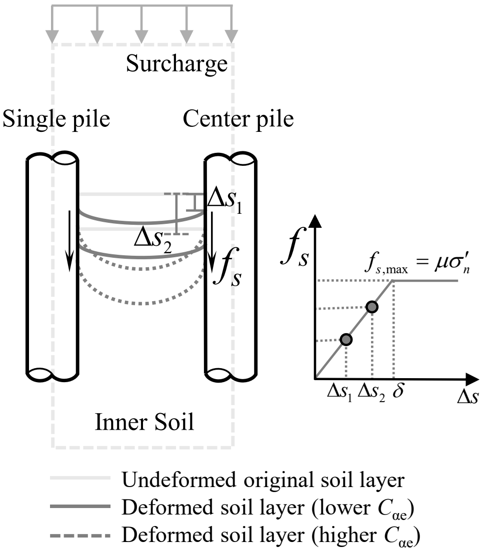

Figure 4-8 Schematic representation of creep-induced settlement for piles within a group (assuming the pile-soil relative displacement, Δ*s* remains below the threshold displacement, *δ*)

4.4.3 Estimation of *β* value

In practice, the developed NSF on the pile shaft can be calculated using either the total stress-based α method or the effective stress-based β method (Johannessen and Bjerrum 1965, Burland 1973) as follows:

$$f_s = \alpha s_u \tag{4-3}$$

$$f_s = \beta \sigma'_v \tag{4-4}$$

where f_s is the shaft friction, s_u is the undrained shear strength of the clay and σ'_v is the effective vertical stress, α and β are the adhesion factor and empirical factor, respectively. In comparison to the α method, the β method is based on the effective stress theory which better aligns with engineering conditions. Since NSF is a long-term issue related to consolidation, it is more reasonable to account for changes in effective stress when estimating shear stress at the pile-soil interface. Therefore, the β method is adopted in this research and the dragload at the NP can be estimated based on the following equation:

$$P_{\text{drag, NP}} = \pi D \int_0^{L_{NP}} \beta \sigma_v' dz \tag{4-5}$$

where L_{NP} and D are the depth of the NP and the pile diameter, respectively. The back-calculated β values for the center pile in the pile group and for the single pile at $C_{\alpha e}$=0.01 are presented in Figure 4-9. Generally, the β values range from 0.16 to 0.20 and increase with pile spacing, stabilizing gradually after S/d=5. When the pile spacing reaches 7 d, the β value approaches that of the single pile, indicating a transition from a better shielding effect to minimal shielding. A similar observation was also reported by Ng et al. (2008), who found β values of 0.13-0.18 for the center pile in a pile group and 0.25 for the single pile. Similarly, Shen (2008) reported β values of 0.18 for center pile in a group and 0.24 for the single pile based on centrifuge tests.

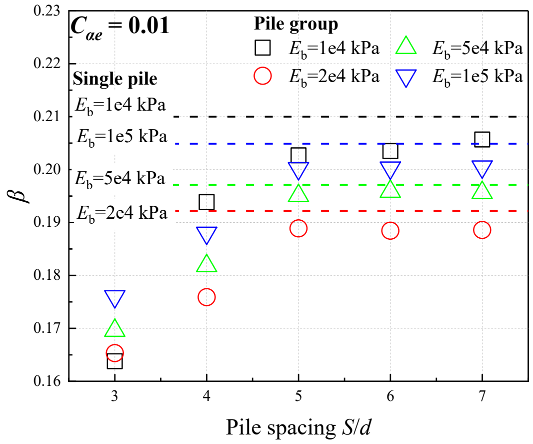

Figure 4-9 Back-calculated β value for the pile group and single pile at $C_{\alpha e}$=0.01

The β value is widely recognized as a critical parameter for estimating the NSF. A summary of β values from the literature, along with those from current study, is presented in Table 4-3. The β value ranges from 0.18 to 0.25 for the soft soil case studies and centrifuge tests (Johannessen and Bjerrum 1965, Burland 1973, Clemente 1981, Indraratna et al. 1992, Leung et al. 2004). NAVFAC (1986) primarily recommended the β method for calculating unit skin friction, depending on soil type: 0.20-0.25 for clay, 0.25-0.35 for silt and 0.35-0.50 for sand. Similarly, Canadian Geotechnical Society (2006) suggested a β value range of 0.20-0.30. The calculated values from the current model generally fall within these ranges.

Table 4-3 Comparison of the β value with results from literature

	β value (single pile)	β value (center pile in pile group)
This study ($C_{\alpha e}$=0.01)	0.21	0.16-0.20
Johannessen and Bjerrum (1965)	0.18-0.23	-
Burland (1973), Indraratna et al. (1992) and Leung et al. (2004)	0.25	-
NAVFAC (1986)	0.20-0.25	-
Lee and Chen (2003)	-	0.23
Canadian Geotechnical Society (2006)	0.20-0.30	-
Ng et al. (2008)	0.25	0.13-0.18
Shen (2008)	0.24	0.18[1]

[1] Back calculated from the centrifuge pile group test

4.4.4 Vertical effective stress distribution

The distribution of vertical effective stress, σ'_v, within the clay layer in the *x*-*y* plane for the pile group analysis (with $C_{\alpha e}$=0.01, E_b=1e4kPa and pile spacing of 3 *d*, 5 *d* and 7 *d*) is depicted in Figure 4-10. For comparison, the σ'_v distribution of a single pile is also plotted. The results indicate that, in the far field away from the pile group, the stress distribution is nearly horizontal, reflecting uniform stress, particularly in the upper clay layer. However, as the stress contours approach the pile group, they become distorted, showing reduced stress at the pile-soil interface. The stress within the pile group is generally lower than outside, a phenomenon known as hang-up effect (Ng et al. 2008). Furthermore, as the pile spacing increases, this hang-up effect weakens and the stress distribution adjacent to the center pile with a pile spacing of 7 *d* becomes similar to that of a single pile, as indicated in Figure 4-10(c) and (d).

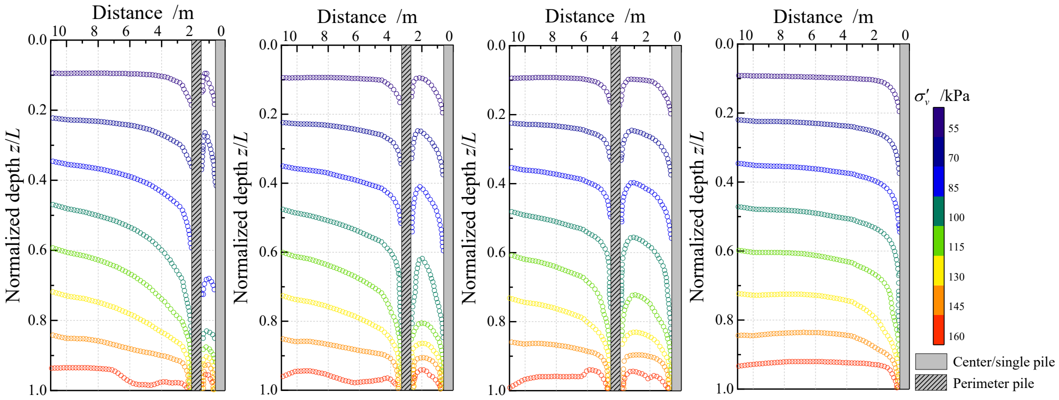

(a) (b) (c) (d)

Figure 4-10 Comparison of vertical effective stress () contours for the pile group analysis ($C_{\alpha e}$=0.01, E_b=1e4kPa) with pile spacings of: (a) 3*d*; (b) 5*d*; (c) 7*d*; and (d) the single pile analysis

The hang-up effect within a pile group subjected to NSF is clearly illustrated with reference to Figure 4-11, where Δs represents the relative displacement between the soil and pile. Each pile in the group generates upward shear stress, τ_3, along the pile-soil interface, leading to a general reduction in both settlement and effective stresses within the soil of the pile group. However, it should be noted that hang-up effects are limited when the pile spacing increases. With wider spacing, the ability of the piles to confine or support the inner soil weakens, reducing the hang-up effect. Consequently, the self-weight of the soil and any external surcharge cannot be fully resisted by the limited upward shear force mobilized along the pile shaft, which is governed by Coulomb friction. As a result, significant soil settlement may occur, accompanied by full pile-soil slippage along the shaft and an increase in NSF, as illustrated in Figure 4-11(b). There exists a critical pile spacing beyond which the mobilized NSF on the center pile becomes equivalent to that of on an isolated single pile.

Recent design codes fail to account for the critical pile spacing in the practical design for pile groups, especially those found on soft soils undergoing substantial settlement. The critical pile spacing is essential for achieving an economic and effective pile group design. It is generally recommended that pile spacing does not exceed 7 *d* to maintain an optimal shielding effect. However, for end-bearing piles and sites with high creep potential, this spacing should be further reduced. It is noted that the critical pile spacing can be influenced by various factors, including pile group configuration, surcharge magnitude, pile head loading, soil properties, end-bearing layer stiffness, creep effects, pile geometry and pile-soil interface behavior. Moreover, the site condition varies from one project to another. Future research is needed to develop a more sophisticated method that considers the coupling effects of all influencing parameters on the critical pile spacing.

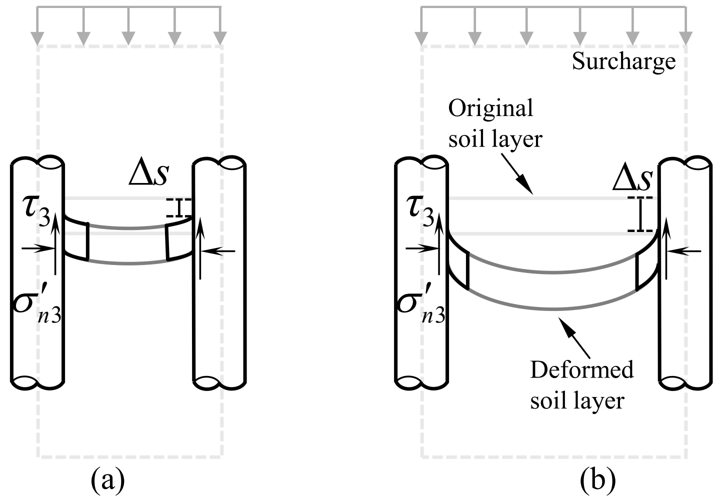

Figure 4-11 Schematic representation of the hang-up effect in the soil within the pile group: (a) small pile spacing; (b) large pile spacing

The calculated σ'_v within the pile group for various pile spacings and depths is plotted in Figure 4-12 for a detailed comparison to investigate the hang-up effect. The σ'_v in the far field, around the single pile, as well as the original σ'_v after the surcharge loading, are also included for reference. It is evident that the use of sacrificial piles results in lower σ'_v compared to a single pile due to the hang-up effect. This effect increases with depth but decreases with pile spacing. The hang-up effect intensifies with depth, reaching its maximum around the NP position. It can be estimated that along the center pile, shielded by sacrificial piles with a 3 *d* pile spacing, the σ'_v is reduced by up to 25% compared to the unprotected single pile. Furthermore, when the pile spacing reaches 7 *d*, the σ'_v becomes similar to that of a single pile, indicating minimal or no hang-up effect at this spacing. From the above effective stress probing regime, it can be concluded that the resulting stress reduction causes a decrease in the NSF along the piles, particularly for the center pile, which is the primary cause of the NSF pile group effect.

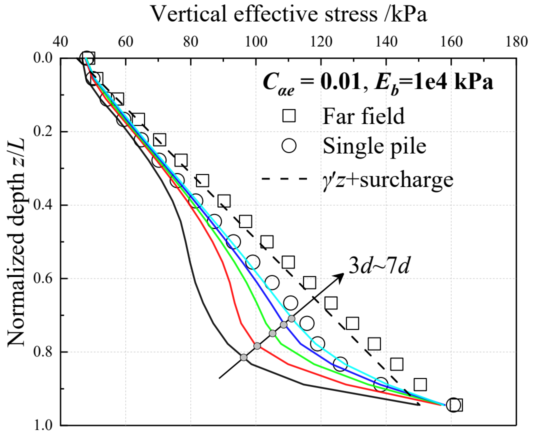

Figure 4-12 Calculated distributions of vertical effective stress for various pile spacings ($C_{\alpha e}$=0.01, E_b=1e4kPa)

4.4.5 Bending moment distribution on the sacrificial piles

It is hypothesized that the reduction in effective stress of soil within a pile group will result in unbalanced stress around the shafts of sacrificial piles. This unbalanced normal stress may induce undesirable effects, such as additional bending moments along the shafts. The distribution of these additional bending moments for piles within the group is collected in Figure 4-13. It is observed that both the corner pile and the perimeter pile experience additional bending moments, while the center pile remains perfectly protected, with no development of bending moments. Compared to the perimeter pile, the corner pile experiences higher bending moments, which can be attributed to the greater unbalanced stress between the exterior and interior of the pile group. The maximum bending moment occurs at a depth of 0.6 *L*. A decreasing trend in the bending moment is observed as increasing of the pile spacing, suggesting that this stress gradient becomes less obvious.

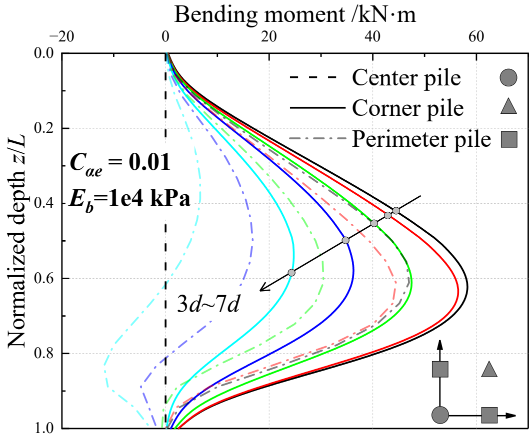

Figure 4-13 Additional bending moment distribution for piles with various pile spacings ($C_{\alpha e}$=0.01, E_b=1e4kPa)

Furthermore, the normalized maximum bending moment for the corner pile is plotted in Figure 4-14, where M represents the maximum bending moment for the corner pile shaft and $M_{\max}$ represents the maximum M calculated from the parametric analysis. The M occurs at a pile spacing of 3d and E_b=1e5 kPa. This maximum bending moment can be effectively reduced by increasing the pile spacing, which shows a generally linear decrease with greater pile spacing. Specifically, the M at a 7d spacing is approximately 60% lower than that at 3d. For a spacing of 3d, an increase in E_b typically results in a higher M. However, for the pile spacings greater than 3d, M becomes less sensitive to changes in E_b. It should be noted that such an additional bending moment can also present significant concerns for piles designed exclusively for axial loads.

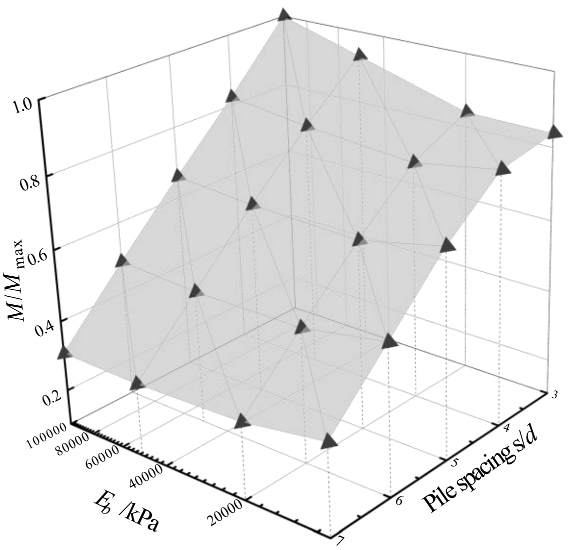

Figure 4-14 Normalized maximum bending moment for the corner pile

4.5 Summary

The pile group constructed in consolidating ground may experience less dragload compared to a single pile. Numerical simulations were performed in this study to provide insights into this issue. Herein, an elasto-viscoplastic model adopting an enhanced time integration algorithm with was successfully implemented into ABAQUS through the user subroutine UMAT. This model was initially employed to simulate and verify a centrifuge test. Subsequently, a parametric analysis was performed with varying pile spacing and end-bearing layer stiffness. The detailed findings and conclusions are as follows:

(1) It is observed that the neutral plane (NP) for the friction pile is located at approximately 0.83 times the pile embedded depth below the soil surface, while for the end-bearing pile, it is near the pile toe. Furthermore, the NP location is not affected by the presence of the sacrificial pile.

(2) Generally, sacrificial piles can be designed to mitigate dragload, with the shielding effect being more pronounced at small pile spacings and less pronounced when the end-bearing layer stiffness has higher stiffness. Furthermore, the group effect is highly dependent on the site-specific creep behavior, becoming less significant under high creep conditions.

(3) The group effect on dragload decays exponentially with the pile spacing. When the pile spacing exceeds 7 *d*, it can be recommended as the maximum distance between the center and sacrificial piles to maintain an optimal shielding effect. However, for end-bearing piles and sites with high creep potential, this critical pile spacing should be reduced.

(4) Compared with the α method, the β method is adopted in this research to estimate the dragload on pile. The β value for the single unprotected pile is 0.21, while for the shielded pile, it ranges from 0.16 to 0.20. Additionally, the β value for the shielded pile increases with pile spacing and is not sensitive to variations in end-bearing layer stiffness.

(5) The reduction in effective stress of soil within a pile group is identified as the primary cause of the NSF pile group effect. However, this unbalanced stress can generate additional bending moments along the shafts, posing significant concerns for piles designed exclusively for axial loads.

CHAPTER 5 PILE PENETRATION EFFECT ON DEVELOPMENT OF NEGATIVE SKIN FRICTION

5.1 Introduction

In this section, a novel hydro-mechanical coupled SNS-PFEM framework is developed to investigate the effect of pile penetration on the development of NSF with consolidation. An elastic viscoplastic model with cutting plane algorithm is applied to account for the time dependency of soft soil. The numerical model is established and verified through a well-documented field case study. A parametric analysis is then conducted to examine the impact of pile penetration rate on soil stress and NSF development. Moreover, current design methods cannot accurately predict the β value or account for its time dependency. An empirical model for time-dependent behavior of the β value is thus proposed and its applicability to other similar cases reported in the literature is verified.

5.2 2D axisymmetric hydro-mechanical coupled SNS-PFEM framework

To account for geometrical nonlinearity, the final equilibrium equation must be formulated under the deformed configuration. The weak form of the porous medium domain Ω bounded by boundary of Γ, expressed in an updated Lagrangian framework, can be represented as follows:

$$\int_{\Omega^{t+\Delta t}} \delta \boldsymbol{e} : \boldsymbol{\sigma}^{t+\Delta t} d\Omega = \int_{\Omega^{t+\Delta t}} \delta \boldsymbol{u} \cdot \boldsymbol{b}^{t+\Delta t} d\Omega + \int_{\Gamma^{t+\Delta t}} \delta \boldsymbol{u} \cdot \bar{\boldsymbol{t}}^{t+\Delta t} d\Gamma \tag{5-1}$$

with

$$\boldsymbol{\sigma}^{t+\Delta t} = \boldsymbol{\sigma}'^{t+\Delta t} + \mathbf{I}p^{t+\Delta t} \tag{5-2}$$

where $\boldsymbol{e} = 1/2\left(\nabla \boldsymbol{u} + \nabla \boldsymbol{u}^T\right)$ is the strain tensor; $\boldsymbol{u}$ is the displacement; $\boldsymbol{\sigma}$ and $\boldsymbol{\sigma}'$ denote the total Cauchy stress tensor and the effective stress tensor; $\delta\boldsymbol{u}$ and $\delta\boldsymbol{\varepsilon}$ are the virtual displacements and virtual strains, respectively; $\boldsymbol{b}$ and $\bar{\boldsymbol{t}}$ are the body force and prescribed boundary traction, respectively*;* p represents the pore pressure; $\mathbf{I}$ is the identity tensor; the superscripts t and Δt are the time labels. It is noted that $\delta\boldsymbol{e}$ is measured on the deformed configuration.

For the fluid phase, the mass conservation equation needs to be considered, and its weak form in the deformed configuration is derived as follows:

$$\int_{\Omega^{t+\Delta t}} \delta p \cdot \dot{e}_v^{t+\Delta t} d\Omega - \int_{\Omega^{t+\Delta t}} \delta \nabla p \cdot \boldsymbol{q}_f^{t+\Delta t} d\Omega = -\int_{\Gamma^{t+\Delta t}} \delta p \cdot \bar{\boldsymbol{q}}_f^{t+\Delta t} d\Gamma \tag{5-3}$$

where $\dot{e}_v$ represents the volumetric strain rate; $\boldsymbol{q}_f$ and $\bar{\boldsymbol{q}}_f$ denote the Darcy velocity of fluid flux and prescribed Darcy velocity of fluid flux.

An iteration method is required to solve the nonlinear equations mentioned above. In this study, the Picard algorithm is employed, chosen over a full Newton-Raphson scheme for solving the nonlinear system. The backward Euler iterative scheme for Eq. (5-1) and (5-3) is expressed as follows:

$$\begin{aligned}&\int_{\Omega^{t+\Delta t}} \delta \boldsymbol{e} : \boldsymbol{D} : \Delta \boldsymbol{e} d\Omega - \int_{\Omega^{t+\Delta t}} \delta e_v \cdot \Delta p d\Omega = \int_{\Omega^{t+\Delta t}} \delta \boldsymbol{u} \cdot \boldsymbol{b}_{[k]}^{t+\Delta t} d\Omega + \int_{\Gamma^{t+\Delta t}} \delta \boldsymbol{u} \cdot \bar{\boldsymbol{t}}_{[k]}^{t+\Delta t} d\Gamma \\ &- \int_{\Omega} \delta \boldsymbol{e} : \boldsymbol{\sigma}'^{t+\Delta t}_{[k]} d\Omega + \int_{\Omega} \delta e_v \cdot p_{[k]}^{t+\Delta t} d\Omega\end{aligned} \tag{5-4}$$

$$\begin{aligned}&\int_{\Omega^{t+\Delta t}} \delta p \cdot \Delta e_v d\Omega - \Delta t \int_{\Omega^{t+\Delta t}} \delta \nabla p \cdot \Delta \boldsymbol{q}_f d\Omega = -\Delta t \int_{\Gamma^{t+\Delta t}} \delta p \cdot \left(\bar{\boldsymbol{q}}_f^{t+\Delta t}\right)_{[k]} d\Gamma \\ &- \int_{\Omega^{t+\Delta t}} \delta p \cdot \left(e_v^{t+\Delta t}\right)_{[k]} d\Omega + \Delta t \int_{\Omega^{t+\Delta t}} \delta \nabla p \cdot \left(\boldsymbol{q}_f^{t+\Delta t}\right)_{[k]} d\Omega\end{aligned} \tag{5-5}$$

where the subscript [k] represents the iteration number. The effective stress can be updated as follows (Fang et al. 2024):

$$\boldsymbol{\sigma}'^{t+\Delta t} = \boldsymbol{Q}\boldsymbol{\sigma}'^{t}\boldsymbol{Q}^{T} + \int_{t}^{t+\Delta t} \boldsymbol{D}_{c}\dot{\boldsymbol{e}}dt \tag{5-6}$$

with

$$\boldsymbol{Q} = \left(\mathbf{I} - \alpha\boldsymbol{w}\right)^{-1}\left(\mathbf{I} + \left(1-\alpha\right)\boldsymbol{w}\right);\ \boldsymbol{w} = \frac{1}{2}\left(\nabla\boldsymbol{u} - \nabla\boldsymbol{u}^{T}\right) \tag{5-7}$$

where $\dot{\boldsymbol{e}}$ is the strain rate; $\boldsymbol{D}_c$ is the material constitutive tensor; It can be shown that the stress transformation in Eq. (5-6) remains objective if $\boldsymbol{Q}$ is orthogonal. The orthogonality of $\boldsymbol{Q}$ is ensured when the strain increment and the spin tensor increment are evaluated with respect to the configuration at the midpoint $t+\Delta t/2$ with $\alpha=0.5$. Essentially, Eq. (5-6) represents the incremental form of the Jaumann stress rate.

Due to the susceptibility of the FEM to mesh distortion in geotechnical large deformation problems, the SNS-PFEM, which stores all historical variables at the nodes and thereby eliminates the need for frequent variable mapping, is employed to discretize Eq. (5-4) and (5-5). The system matrix can then be expressed in the following iterative form:

$$\begin{bmatrix} \boldsymbol{K}^{uu} & -\boldsymbol{K}^{up} \\ -(\boldsymbol{K}^{up})^{T} & -\Delta t\boldsymbol{K}^{pp} \end{bmatrix}\begin{bmatrix} \Delta\boldsymbol{u} \\ \Delta\boldsymbol{p} \end{bmatrix} = \begin{bmatrix} \boldsymbol{r}_{u} \\ -\boldsymbol{r}_{p} \end{bmatrix} \tag{5-8}$$

with

$$\boldsymbol{K}^{uu} = \int_{\Omega^{t+\Delta t}} \tilde{\boldsymbol{B}}_{u}^{T}\boldsymbol{D}\tilde{\boldsymbol{B}}_{u}d\Omega,\ \boldsymbol{K}^{up} = \int_{\Omega^{t+\Delta t}} \tilde{\boldsymbol{B}}_{u}^{T}\boldsymbol{m}\boldsymbol{N}_{p}d\Omega,\ \boldsymbol{K}^{pp} = \int_{\Omega^{t+\Delta t}} \gamma_{f}^{-1}\tilde{\boldsymbol{B}}_{p}^{T}\boldsymbol{k}_{f}\tilde{\boldsymbol{B}}_{p}d\Omega \tag{5-9}$$

$$\boldsymbol{r}_u = \int_{\Omega^{t+\Delta t}} \boldsymbol{N}_u^T \boldsymbol{b}_{[k]}^{t+\Delta t} d\Omega + \int_{\Gamma^{t+\Delta t}} \boldsymbol{N}_u^T \overline{\boldsymbol{t}}_{[k]}^{t+\Delta t} d\Gamma - \int_{\Omega^{t+\Delta t}} \tilde{\boldsymbol{B}}_u^T \tilde{\boldsymbol{\sigma}}_{[k]}^{\prime t+\Delta t} d\Omega + \int_{\Omega^{t+\Delta t}} \tilde{\boldsymbol{B}}_u^T \boldsymbol{m} p_{[k]}^{t+\Delta t} d\Omega \tag{5-10}$$

$$\boldsymbol{r}_p = -\Delta t \int_{\Gamma^{t+\Delta t}} \boldsymbol{N}_p^T \left(\overline{\boldsymbol{q}}_f^{t+\Delta t} \right)_{[k]} d\Gamma + \Delta t \int_{\Omega^{t+\Delta t}} \tilde{\boldsymbol{B}}_p^T \left(\boldsymbol{q}_f^{t+\Delta t} \right)_{[k]} d\Omega - \int_{\Omega^{t+\Delta t}} \boldsymbol{N}_p \left(\varepsilon_v^{t+\Delta t} \right)_{[k]} d\Omega \tag{5-11}$$

with $\boldsymbol{m}$, $\tilde{\boldsymbol{B}}_u$ and $\tilde{\boldsymbol{B}}_p$ defined as:

$$\boldsymbol{m} = [1 \quad 1 \quad 0 \quad 1]^T \tag{5-12}$$

$$\tilde{\boldsymbol{B}}_u = \left[\tilde{\boldsymbol{B}}_u{}^1, \tilde{\boldsymbol{B}}_u{}^2, \cdots \tilde{\boldsymbol{B}}_u{}^I, \cdots \tilde{\boldsymbol{B}}_u{}^n \right]; \ \tilde{\boldsymbol{B}}_u{}^I = \alpha^I \begin{bmatrix} \partial N_I / \partial r & 0 \\ 0 & \partial N_I / \partial z \\ \partial N_I / \partial z & \partial N_I / \partial z \\ N_I / r & 0 \end{bmatrix} \tag{5-13}$$

$$\tilde{\boldsymbol{B}}_p = \left[\tilde{\boldsymbol{B}}_p{}^1, \tilde{\boldsymbol{B}}_p{}^2, \cdots \tilde{\boldsymbol{B}}_p{}^I, \cdots \tilde{\boldsymbol{B}}_p{}^n \right]; \ \tilde{\boldsymbol{B}}_p^I = \alpha^I \begin{bmatrix} \partial N_I / \partial r \\ \partial N_I / \partial z \end{bmatrix} \tag{5-14}$$

where $\boldsymbol{K}^{uu}$ denotes the stiffness of the solid phase; $\boldsymbol{K}^{up}$ the hydro-mechanical coupling matrix; $\boldsymbol{K}^{pp}$ the permeability matrix; $\boldsymbol{r}_u$ the residual traction vectors; $\boldsymbol{r}_p$ the residual flux vectors; $\boldsymbol{k}_f$ is the permeability coefficient; γ_f is the fluid weight per unit volume; the superscript I represents the element I; N is the shape function; α is the stable smoothing parameter. The polynomial pressure projection (PPP) method is employed to eliminate pore pressure instability (White and Borja 2008). Furthermore, the 3-node linear triangular elements are adopted in this framework. The hydro-mechanical coupled contact algorithm, based on the dual Lagrange multiplier method (Fang et al. 2022, 2024b), is used to simulate the soil-structure interaction. The tangential part of the contact algorithm follows Coulomb's law, where the maximum allowable tangential stress, τ, is equal to $\mu\sigma_n'$, where μ is the friction parameter and σ_n' is the effective normal stress.

5.3 Validation on field scale

5.3.1 Bangkok pile load tests

The field-monitored test carried out by Indraratna et al. (1992) is described in detail in Section 3.2.2. However, Chapter 3 focuses on a simplified wished-in-place pile model, rather than addressing the pile penetration method adopted in the field cases. The installation procedure for the pile is presented as follows:

Each instrumented pile was divided into six segments, five segments of 4 m in length each, and one upper segment of 6 m in length. Initially, two 4 m pile segments were connected to form an 8 m length pile segment, which was then installed into the ground at an approximate penetration rate of 1 m/min until the pile tip reached the depth of 8 m. The pile was then left for 8 days before undergoing a pullout test. The pile installation procedure was repeated when the pile tip reached the depths of 12 m, 16 m and 20 m, after intervals of 8 days, 19 days, 30 days, respectively, following the installation of the initial 8 m pile segment. The last 6 m pile segment was connected and driven, bringing a total embedded pile depth of 25 m after 40 days of the initial pile segment installation. Based on this field test, the pile penetration analysis can be conducted and analyzed.

5.3.2 Numerical model

We use the uncoated single pile to validate our model. In the field test, the distance between the coated and uncoated pile is 10 m (25 times the pile diameter), which is sufficient to ignore the pile group effect and boundary effect. Therefore, the penetration of the single pile is simulated as a 2D-axisymmetric problem for simplicity. The pile length L_p is 25 m and the pile diameter D_p is 0.4 m. A curved shape of pile tip is adopted to minimize the effect of sharp corner problems during pile penetration (Abu-Farsakh et al. 2015). The soil domain is extended to a width of 10 m and a length of 40 m. The minimum distance from the pile to the soil boundary is larger than 10 times the pile diameter to avoid the boundary effects (Liang et al. 2021, 2024).

In this analysis, the soil and pile are discretized with the 3-node linear triangular elements. The mesh is denser near the pile and coarser far away from the pile to mitigate the influence of stress concentration and enhance calculation efficiency. A mesh density sensitivity analysis is conducted by varying the smallest element size around the pile from $0.05D_p$ to D_p. The numerical results for element sizes $0.05D_p$ and $0.1D_p$ are essentially identical, indicating that mesh convergence is achieved with an element size $0.1D_p$. Therefore, the typical element size of soil around the pile is set to $0.1D_p$ for subsequent analyses, as illustrated in Figure 5-1.

Except for the contact area between the pile and soil, the left side of the pile and both sides of the soil are constrained horizontally, while the bottom surface of the soil is fixed in the vertical direction. Drainage boundaries are established at the groundwater table and the top of the sand layer. The hydro-mechanical coupled contact algorithm, based on the dual Lagrange multiplier method (Fang et al. 2022, 2024b), is used to simulate the pile-soil interaction. In this model, the exterior surface of the pile is regarded as the master surface and the soil surface as the slave surface. The classic Coulomb friction theory is applied for the pile-soil interface, with a friction parameter

μ of 0.3, estimated by $\mu = \tan(2/3\varphi_c)$, where φ_c is the effective friction angle of soil equal to 25° (Yan et al. 2012).

The behavior of the soil plugging is recognized as one of the main construction effects of open-ended piles installation. However, field records from Indraratna et al. (1992) did not provide detailed information on the soil plug after the pile penetration. Liu et al. (2011) conducted a similar field case study on the soil plug formation after the pile installation and reported a limited soil plug ratio (PLR). The PLR is calculated as PLR = *H/L*, where *H* is the length of soil plug corresponding to an embedded length of pile, *L*. Furthermore, Niazi and Mayne (2013) reported that the additional mobilized shaft friction between the soil plug and the inner pile wall can be considered part of the pile base resistance for the jacked open-ended piles and the outer diameter of the jacked open-ended pile is used for shaft friction calculations. Therefore, a solid pile with a diameter of 0.4 m, rather than a hollow one, is used for simplicity; the equivalent elastic modulus of the solid pile is calculated to maintain the same axial rigidity as the hollow pile (Liu et al. 2012, Yan et al. 2012, Chiou and Wei 2021, Liang et al. 2023). The isotropic linear elastic model is applied to model the pile and bottom sand layer. A solid pile, rather than a hollow one, is used; the equivalent elastic modulus of the solid pile is calculated to maintain the same axial rigidity as the hollow pile. The ANICREEP model, which accounts for the time dependency of soft soil, is used. $C_{\alpha e}$ is the key parameter for the applicability of the elasto-viscoplastic constitutive model in practical engineering. However, this parameter is not reported in the field test. Jin et al. (2019) found $C_{\alpha e}$ to be highly correlated with the physical properties of soft soils, such as void ratio, plasticity index and liquid limit, and proposed a reliable method to predict $C_{\alpha e}$

through evolutionary polynomial regression. This method is used to estimate $C_{\alpha e}$, as shown in Eq. (5-15):

$$\ln(C_{\alpha e}) = \left(0.055\frac{1}{w_L^2 I_p} - 0.107\frac{1}{I_p} + 0.272\left(\frac{w_L}{I_p}\right)^2\right)e - 2.222 \tag{5-15}$$

where e is the void ratio, I_p is the plasticity index and w_L is the liquid limit.

Although the structure of clays in the selected case study was not reported as well, the field soil can generally be estimated as a type of slightly structured soil (Horpibulsuk et al. 2007), making it reasonable to ignore the interparticle bonding and debonding effects in simulations. The other parameters can be obtained either from field measurements or interpretations of field data. The permeability coefficient k is enlarged 4 times from the ground measurement data due to the limitations of drainage conditions on the site and the inhomogeneity of soil (Yan et al. 2012, Chiou and Wei 2021). A complete overview of the model parameters is presented in Table 5-1.

The numerical model for long-term development of NSF considering pile penetration comprises three distinct stages: pile penetration, surcharge loading, and subsequent consolidation. Before pile penetration, a small surcharge of 2 kPa is applied on the top of soil surface to prevent the mean effective stress of the top layer from approaching zero, thereby ensuring the computational convergence at the initial stage of pile penetration. The pile penetration is achieved by imposing a vertical displacement of 0.125 D_p at a rate of 1m/min for each incremental step. Once the pile tip reaches the desired depths (i.e., 8m, 12 m, 16 m and 20 m), consolidation is conducted during the interval without a pullout test, simplifying the process until the pile reaches the target embedded depth of 25 m. The construction of the embankment is represented by a surcharge of 34 kPa on the top of soil surface over 3 days. Following the consolidation stage, the generation of dragload and NSF is observed.

For comparison, a wished-in-place pile-soil interaction 2D-axisymmetric model, which is widely used to simulate the development of the NSF (Lee et al. 2002, Liu et al. 2012, Yan et al. 2012, Sun et al. 2015, Chiou and Wei 2021, Liang et al. 2023), is built. The sketch and mesh details of this model are presented in Figure 5-1.

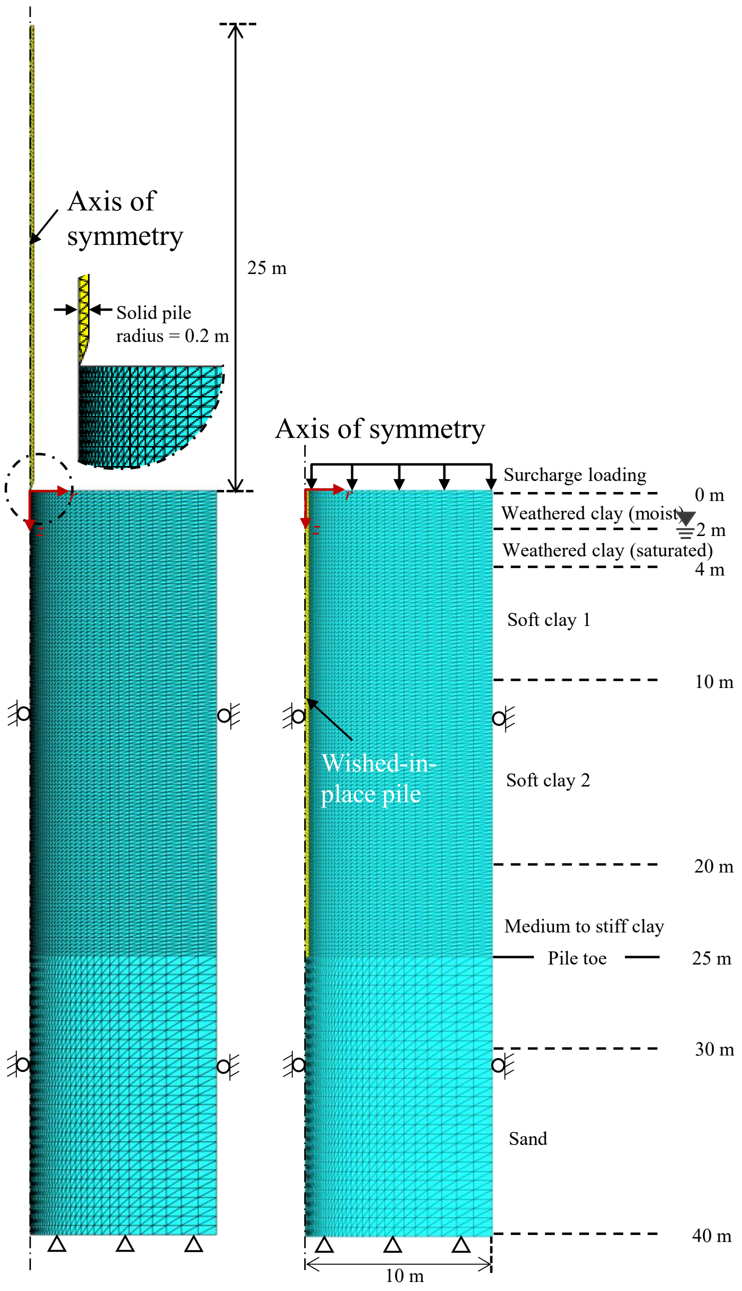

Figure 5-1 Sketch and mesh details of the field verification model with pile penetration (227 elements for pile and 10230 elements for soil) and wished-in-place pile case (250 elements for pile and 10220 elements for soil)

Table 5-1 Summary of parameters for verification case study

Material type	Depth (m)	γ (kN/m^3)^a	κ^b	λ^b	M^b	$e_0{}^a$	k (m/day)^c	OCR^a	$K_0{}^a$	ν^b	$C_{\alpha e}{}^d$	E (kN/m^2)^b
Soil												

Weather clay (moist)	0-2	16.7	0.053	0.182	1.05	1.54	-	2.7	0.7	0.33	0.01	-
Weather clay (saturated)	2-4	16.7	0.053	0.182	1.05	1.54	27×10^{-4}	2.7	0.7	0.33	0.01	-
Soft clay 1	4-10	14.7	0.084	0.514	0.97	2.46	2×10^{-4}	1.2	0.6	0.33	0.021	-
Soft clay 2	10-20	16.7	0.063	0.323	0.98	1.55	1×10^{-4}	1.3	0.6	0.33	0.007	-
Medium to stiff clay	20-30	18.6	0.027	0.116	0.9	1.2	1×10^{-4}	1.8	0.67	0.33	0.004	-
Sand	30-40	19.1	-	-	-	1.2	27×10^{-4}	-	0.45	0.33	-	27440
Pile												
Pile	0-25	14.7	-	-	-	-	-	-	-	0.33	-	30×10^{6}

[a] Obtained from the data interpretation of field measurements reported by Indraratna et al. (1992)
[b] Same parameter values were adopted by Indraratna et al. (1992)
[c] Four times larger than the values reported by Indraratna et al. (1992)
[d] Estimated using Eq. (5-15)

5.3.3 Comparison results

Figure 5-2 compares field-measured and calculated variations in excess porewater pressure with penetration depths at four transducers. During the field test, pore pressure transducers were positioned at depths of 8 m, 12 m, 16 m, and 20 m near the pile. Numerical simulations predict the generation and dissipation of excess porewater pressure following pile penetration to the target depth and subsequent consolidation. Excess porewater pressure increases as the pile tip advances to greater depths, with higher excess porewater pressures dissipating rapidly within a few days.

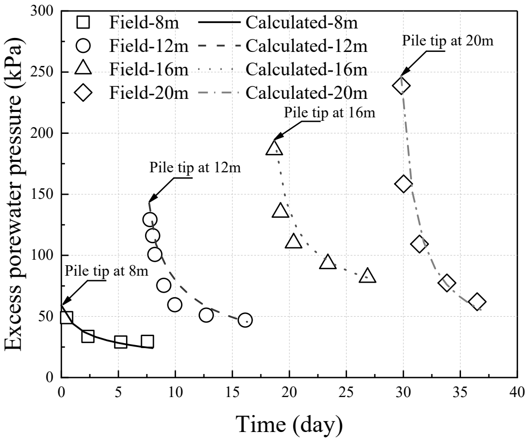

Figure 5-2 Comparison of excess porewater pressure induced by pile penetration at various depths along the pile surface with field measured data

The axial load generated after 265 days of embankment construction is presented in Figure 5-3, alongside field measurement data. Generally, the numerical predictions exhibit a reasonable agreement with the field measurements. Additionally, the calculated axial load of the wished-in-place pile is plotted for comparison. Notably, the calculated results indicate an underestimation of the axial load generation.

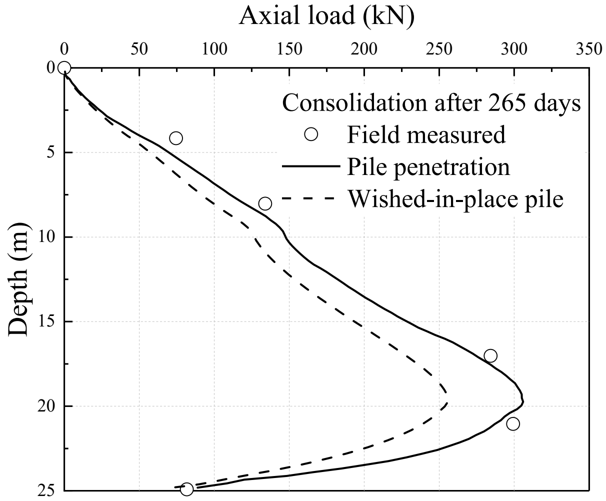

Figure 5-3 Comparison of axial load development with and without pile penetration against field measurement data

Furthermore, Figure 5-4 reveals the variation in unit skin friction along the pile shaft, as interpreted from axial load data and compared with field measurements after 265 days of consolidation following embankment loading. In this figure, NSF and PSF denote the downward and upward friction directions, respectively. The generated NSF, considering pile penetration, generally predicts the trend of the field-measured NSF. However, a discrepancy is observed, with an underestimation of NSF for the wished-in-place pile. This underestimation is attributed to the increase in effective normal stress acting on the pile during penetration, as the soil near the pile is compressed to accommodate the pile volume. Therefore, it is demonstrated that numerically analyzing pile NSF without considering the pile installation process, as in the case of the wished-in-place pile, can yield an underestimation of the NSF.

The results also show a decreasing trend of NSF in the first soft soil layer at a depth of around 8m, which can be attributed to the lower permeability of this layer and the drainage boundary located far away. The dissipation rate of excess porewater pressure is low, which decreases the effective normal stress and results in the lower mobilization of the NSF. Furthermore, the NSF (or PSF) is small near the NP due to the minimal relative displacement, meaning the skin friction is not fully mobilized.

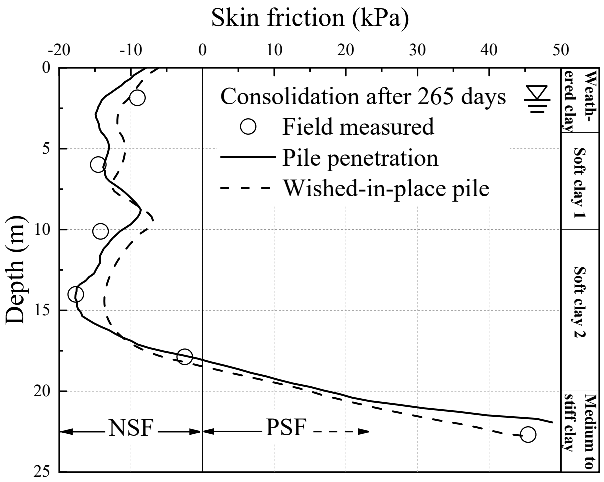

Figure 5-4 Development of skin friction with and without pile penetration

The variation of soil settlement with depth after 265 days of consolidation, as calculated in this model and measured in the field, is compared in Figure 5-5. The measurements were taken 0.25 m away from the pile centerline. The numerical results generally predict soil settlement over time after the application of the surcharge load. Compared to the wished-in-place pile, the soil settlement is slightly underpredicted due to the generation of excess porewater pressure during pile penetration, which delays the consolidation progress.

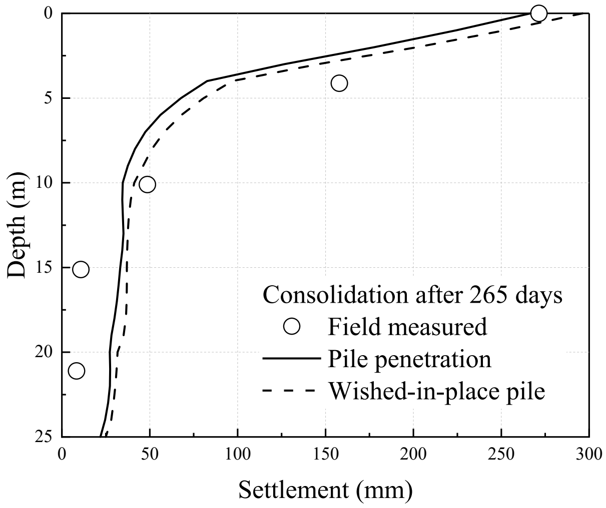

Figure 5-5 Soil settlement profiles with and without pile penetration

5.3.4 Parametric analysis model

Since the numerical model is verified with a well-documented case history, a further extended investigation of the pile installation effect on NSF is pursued by building a simplified single-layer soil numerical model for parametric analysis, as shown in Figure 5-6. Unless otherwise stated, the parameters and analysis framework in the parametric model are the same as those in the aforementioned validation model. The ground water table is located at the ground level. The solid pile, with a diameter of 0.4 m and a length of 20 m, is continuously penetrated into the soil at rates of 0.1 m/min, 1 m/min (benchmark rate) and 10 m/min, respectively, until reaching a depth of 20 m. Table 5-2 summarizes the parameters of the pile and soil layer. After the completion of pile installation, a surcharge with a magnitude of 20 kPa is applied to the top of soil surface, followed by a consolidation procedure. Furthermore, soil nodes at points A, B and C, adjacent to the pile shaft, are selected to analyze the stress changes during pile penetration and consolidation.

Table 5-2 Parameters of soft clay and pile in parametric analysis model

Material type	Depth (m)	γ (kN/m^3)	κ	λ	M	e_0	k ($\times 10^{-4}$ m/day)	OCR	K_0	v	$C_{\alpha e}$	E (kN/m^2)
Soil												
Soft clay	0-30	15	0.063	0.323	0.97	1.5	5.5	1	0.6	0.3	0.005	-
Pile												
Pile	0-20	14.7	-	-	-	-				0.3	-	30×10^6

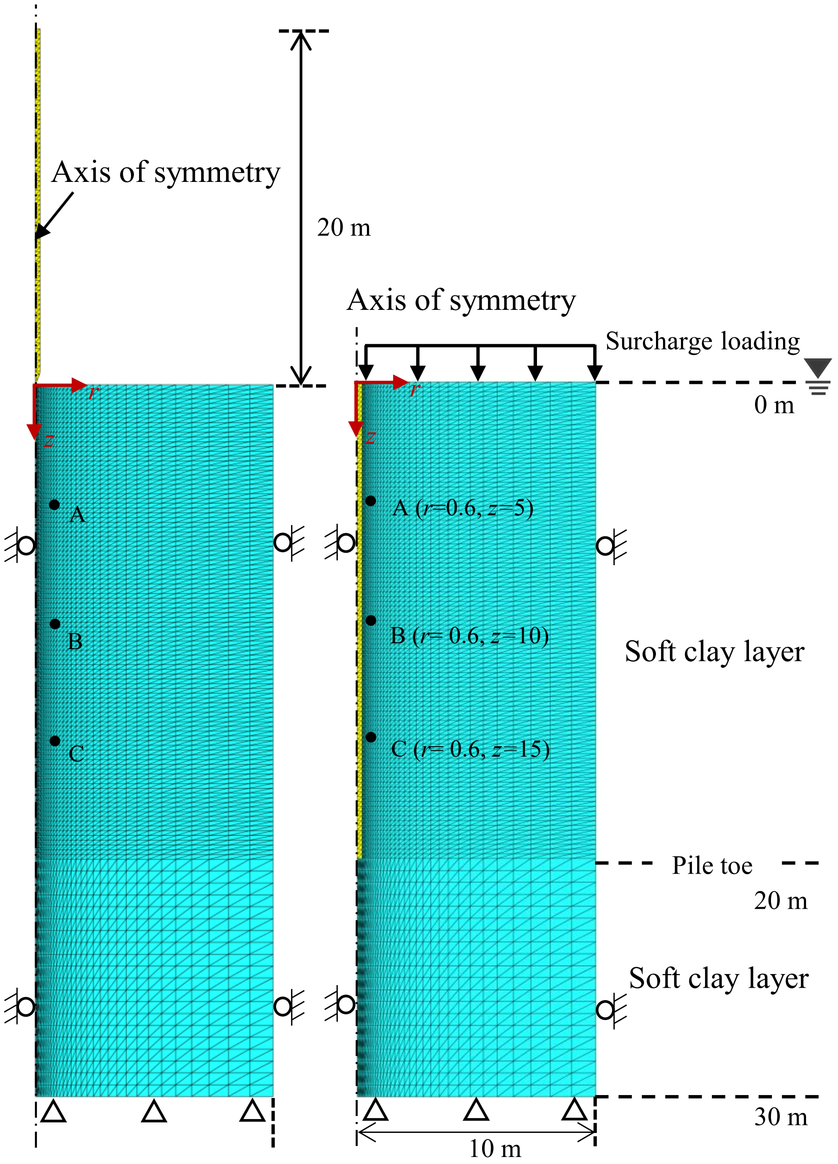

Figure 5-6 Sketch and mesh detail of the parametrical model with pile penetration (197 elements for pile and 7920 elements for soil) and wished-in-place pile (200 elements for pile and 7880 elements for soil)

5.4 Penetration effects on development of negative skin friction

Based on the preceding discussion, Figure 5-7 schematically illustrates the evolution of stress in a soil element adjacent to the pile shaft during pile penetration and after surcharge loading. Throughout these stages, the soil adjacent to the pile shaft is subject to compression and shear, leading to the development of excess porewater pressure u and changes in effective normal (radial) stress σ_n'. The generation of NSF is observed following surcharge loading. Further detailed discussion and comparison are provided below.

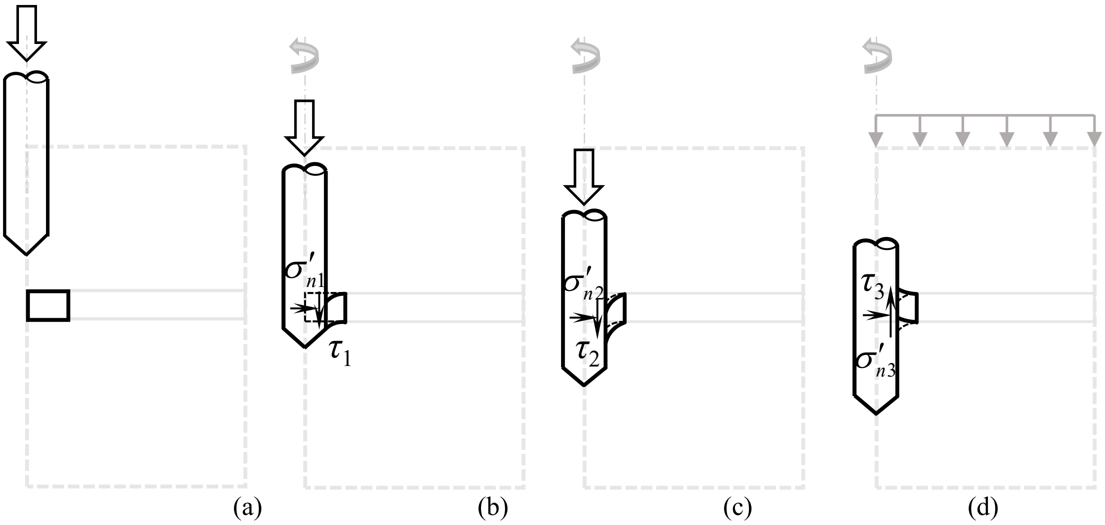

Figure 5-7 Simulation stages of the numerical model: (a) initial stage: pile tip approaches the soil element; (b) stage 1: pile tip passes through the soil element; (c) stage 2: continued shearing until the pile tip reaches the target depth; (d)

stage 3: consolidation after applying surcharge loading (assuming the soil element is above the neutral plane)

5.4.1 Evolution of stresses during pile penetration

5.4.1.1 Effective normal (radial) stress and stress path

The evolution of normalized σ'_n / p'_0 with normalized penetration depth p_d/L during pile penetration for soil nodes A, B and C is shown in Figure 5-8, where p'_0 is the mean effective stress at nodes B before pile penetration, p_d is the penetration depth and L is the pile length. A slightly decreasing and then increasing trend in σ'_n is observed as the pile tip approaches the probe soil nodes, reaching a peak after the pile tip has fully passed through, which is also termed the end of cavity expansion. Cavity expansion refers to the formation of a cylindrical space within the ground to accommodate the pile as the pile tip displaces the surrounding soil. This process concludes when the cavity radius equals the pile radius, marking the end of stage 2, as indicated in Figure 5-7(b). As soon as the pile passes observation nodes, there is a sharp decrease in σ'_n. This phenomenon is referred to as the *h*/*R* effect by Bond and Jardine (1991), where *h* is the depth of the pile tip and *R* is the pile radius. The *h*/*R* effect can be attributed to the soil unloading after pile toe has passed, as the pile penetration process involves a stress controlled boundary at the pile tip, but a displacement controlled boundary along the pile shaft (de Chaunac and Holeyman 2018). σ'_n stabilizes gradually as pile penetration proceeds.

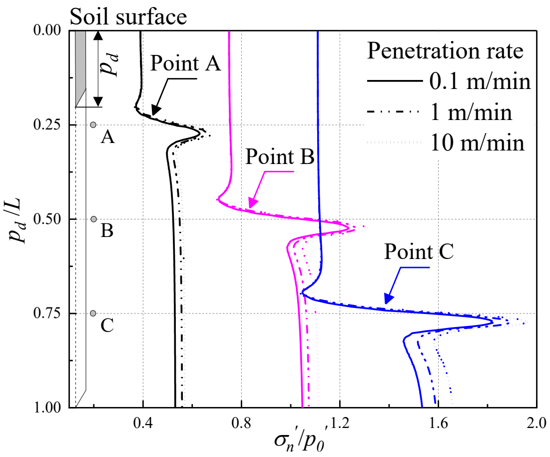

Figure 5-8 Evolution of normalized effective normal (radial) stress during pile penetration for points A, B and C

Generally, the soil element adjacent to the pile first unloads in the radial direction, then loads to a high compressive radial stress, and unloads again, eventually stabilizing from the initial stage to stage 2. With increasing soil depth, there is a drastic change in σ_n' as the pile tip penetrates, reaching a higher residual value of σ_n'. Furthermore, as the penetration rate increases, higher peak and residual σ_n' are observed, especially under higher initial stress state. The generation of σ_n' after the pile tip reaches desired depth with different penetration rates is compared in detail in Figure 5-9.

Figure 5-10 shows the normalized stress path recorded at point B during pile penetration at various rates. Initially, as the pile tip is distant from point B, there is a slight decrease in deviatoric stress q due to soil creep. As the pile tip approaches point B, the stress path follows an increase in q and a slight decrease in effective mean stress p' towards the critical state line. This stage indicates undrained shear at point B, despite the pile tip remaining above this point in the soil. Due to the generation of u with continued shearing, an inflection point appears in p-q space, followed by a continuous degradation of both volumetric and deviatoric stress until the end of cavity expansion.

After cavity expansion, q gradually decreases, indicating an unloading procedure until the end of pile installation. It is observed that at higher penetration rates, the stress path is closer to the critical state line (CSL). At a penetration rate of 10 m/min, the stress path crosses the CSL, follows a loop, and then remains below the CSL. Additionally, higher penetration rates result in higher values of p' and q at the end of pile installation, which can be regarded as rate dependency of soft soil.

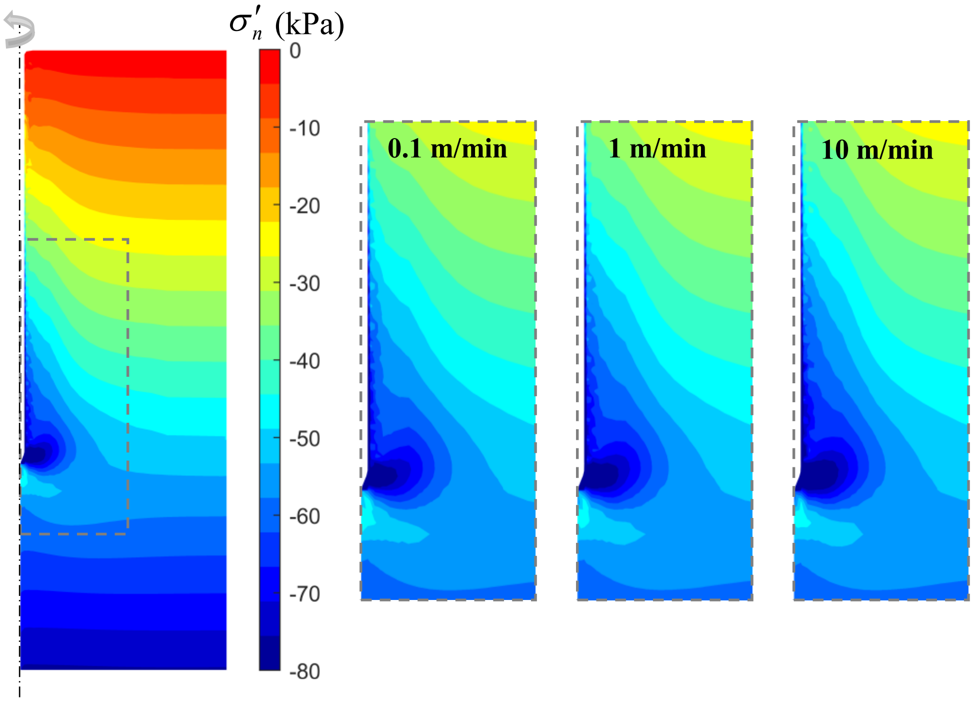

(a) (b)

Figure 5-9 Effect of penetration rate on development of normal (radial) stress after pile penetration: (a) benchmark penetration rate (1 m/min); (b) enlarged

areas for penetration rates of 0.1 m/min, 1 m/min and 10 m/min (negative value represents compressive)

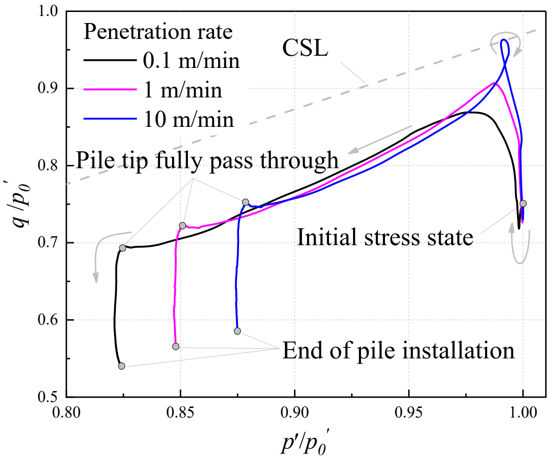

Figure 5-10 Normalized stress path recorded at point B during pile penetration with various penetration rate

5.4.1.2 Excess porewater pressure

The variation of normalized u / p_0' for soil nodes A, B, and C with penetration depth is depicted in Figure 5-11. It is observed that u becomes negative as the pile tip reaches the probe node, which can be attributed to the radial unloading indicated in Figure 5-8. Higher negative u values are observed with increasing depth due to a higher degree of unloading. The magnitude of u increases to its maximum positive value immediately after the completion of cavity expansion. However, once the pile passes that location, u decays rapidly before plateauing at residual values significantly smaller than peak values. The peaking of positive and negative u is more pronounced at greater depths. A similar trend was observed in a field-driven pile test in clay by Roy et al. (1981).

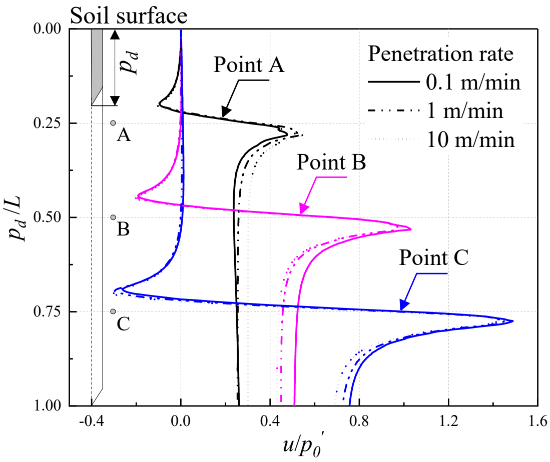

Figure 5-11 Generation of normalized excess porewater pressure during pile penetration

The generation of u after the pile tip reaches the desired depth at various rates is depicted in Figure 5-12. The maximum u occurs around the pile tip, while a negative u zone is observed at a certain depth below the pile tip. Additionally, a thin layer of suction zone is observed adjacent to the pile shaft above the pile shoulder (cone/cylinder transition). This suction response is caused by the pile tip forcing the soil outward, generating suction to retain the soil in contact with the pile shaft, as described by Chow et al. (2014).

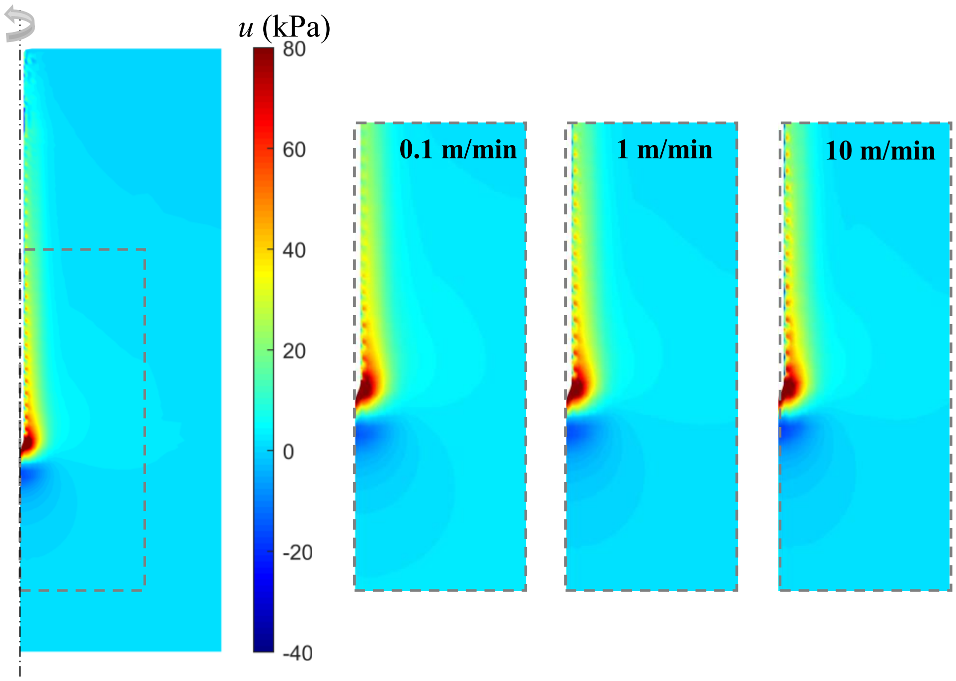

(a) (b)

Figure 5-12 Effect of penetration rate on development of excess porewater pressure after pile penetration: (a) the benchmark penetration rate (1 m/min); (b) enlarged areas for penetration rates of 0.1 m/min, 1 m/min and 10 m/min

5.4.2 Evolution of stresses after surcharge loading

5.4.2.1 Effective normal (radial) and vertical stress

The variation of normalized σ'_n / p'_0 with consolidation for both cases is plotted in Figure 5-13. Similar to the development of u, after several days of consolidation, the discrepancy between various penetration rates yields nearly identical σ'_n around 50 days of consolidation. After primary consolidation, the incremental value of σ'_n for the wished-in-place pile case is larger than that of the pile penetration case. However, the latter case shows a higher value of σ'_n throughout the consolidation stage.

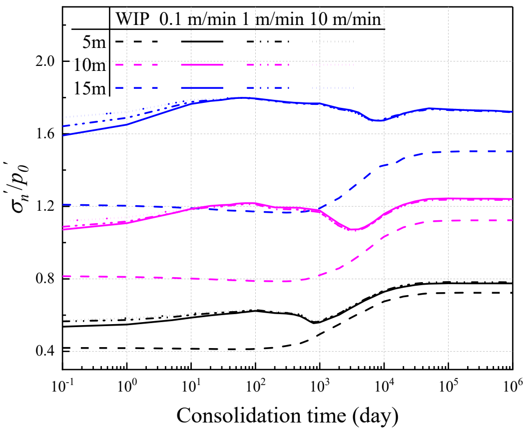

Figure 5-13 Evolution of normalized effective normal (radial) stress with consolidation for points A, B and C in pile penetration case with various penetration rates and wished-in-place (WIP) pile case

Figure 5-14 illustrates the variation of normalized σ_v' / p_0' for the selected nodes during consolidation. In the wished-in-place pile case, there is initially a gradual decrease in σ_v' which may due to the increase in u caused by the initial pile soil interaction. The lower incremental value of σ_v' from the onset to the end of primary consolidation with depth can be attributed to the higher magnitude of the NSF along the pile as depth increases. As u dissipates further, σ_v' exhibits an increasing trend and eventually stabilizes. In the pile penetration case, σ_v' continuously increases until u is fully dissipated, albeit with a lower increasing rate due to Mandel-Cryer. Since the soil adjacent to the pile is severely distorted by the penetration process, a lower σ_v' is observed throughout the consolidation period compared to the wished-in-place pile case, with this effect becoming more evident with depth. Additionally, the rate effect on σ_v' is pronounced at the beginning of consolidation but diminishes after approximately 1000 days.

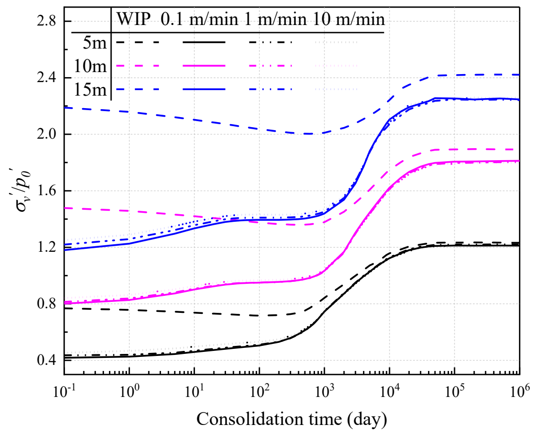

Figure 5-14 Evolution of normalized effective vertical stress with consolidation at points A, B and C for pile penetration case with different penetration rates and wished-in-place (WIP) pile case

5.4.2.2 Excess porewater pressure

The change in normalized u / p_0' after 20 kPa of embankment loading over consolidation time for points A, B and C at different soil depths for both pile penetration case and wished-in-place pile case is plotted in Figure 5-15. In the case of the wished-in-place pile case, an initial increasing trend in u is observed during the early stages of consolidation, with the incremental magnitude of the change in u becoming more pronounced with increasing soil depth. Additionally, the time to reach peak u increases with soil depth. This phenomenon, known as the Mandel-Cryer effect, was first observed in experiments on the consolidation of spherical soil samples by Gibson et al. (1963). As consolidation begins, the center region of the soil becomes effectively stiffer than the soil region near the drainage boundary, generating additional stress in the center region of soil, where u continues to increase initially before starting to dissipate. Furthermore, another factor that can induce this anomalous increase in u is the creep of soil (Yin et al. 1994, Zhu and Yin 2001). At the onset of consolidation, the increasing rate in u induced by plastic volumetric strain on account of creep is higher than the rate of decrease in u due to dissipation, resulting in an overall increasing trend of u.

In the case of pile penetration, although a higher penetration rate results in increased values of u, these discrepancies disappear after approximately 50 days of consolidation. With further consolidation over around 800 days, the generated u for the pile penetration case coincides with that of the wished-in-place pile case until total dissipation. The Mandel-Cryer effect is also evident in the deeply buried soil. After 50000 days of consolidation, u nearly dissipates to zero, indicating the end of primary consolidation and the time can be regarded as T_{eopc}.

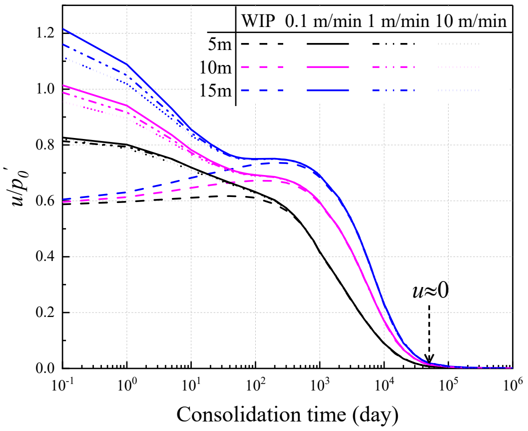

Figure 5-15 Evolution of normalized excess porewater pressure during consolidation at points A, B and C for pile penetration case with varying penetration rates and wished-in-place (WIP) pile case

Figure 5-16 illustrates the normalized stress path recorded at point B during consolidation at various rates. Generally, the stress paths of all three cases follow a similar developmental trend. p' shows a continuous increase until the end of primary consolidation due to the dissipation of excess porewater pressure. At the commencement of consolidation, a reduction in q is observed which can be attributed to the higher rate of increase in σ_n' compared to σ_v'. The value of q reaches its minimum and subsequently increases and the stress paths for the three cases become identical after about 1000 days of consolidation.

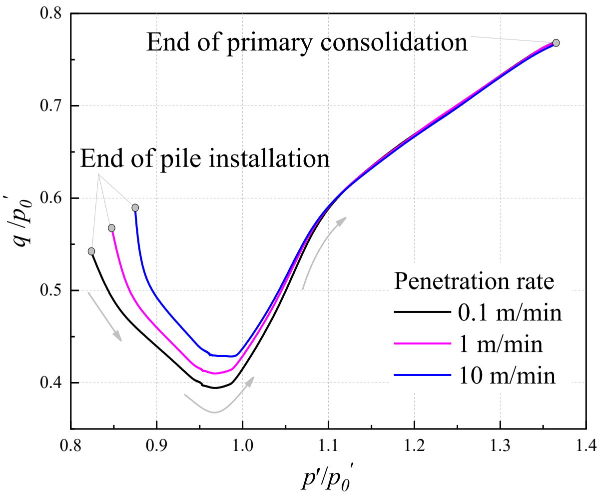

Figure 5-16 Normalized stress path recorded at point B during consolidation with various penetration rates

5.4.3 Development of NSF during consolidation

The development of normalized dragload P/P_{pene} and skin friction f/f_{pene} along the pile with dimensionless time $T=t/T_{\mathrm{eopc}}$ is investigated, and the results are presented in Figure 5-17. Here, P and f represent the mobilized dragload and skin friction, respectively, while P_{pene} and f_{pene} denote the maximum dragload and NSF at the end of primary consolidation for the pile penetration case. The variables t and T_{eopc} indicate the consolidation time and the time to reach primary consolidation, respectively. The period $0 \leq T \leq 1$ denotes the primary consolidation and $T>1$ indicates the secondary compression. As expected, with increasing consolidation time, both dragload and NSF continue to increase, with higher dragload observed in the pile penetration case. The fully mobilized NSF reveals an approximately linear variation with depth. The NP position shows a sharp downward movement at the initial stage of consolidation for both cases, where the NP position describes the depth where soil and pile settle equally, which is also the location where the maximum dragload is generated along the pile. Compared to the pile penetration case, the wished-in-place pile case shows a lower NP position.

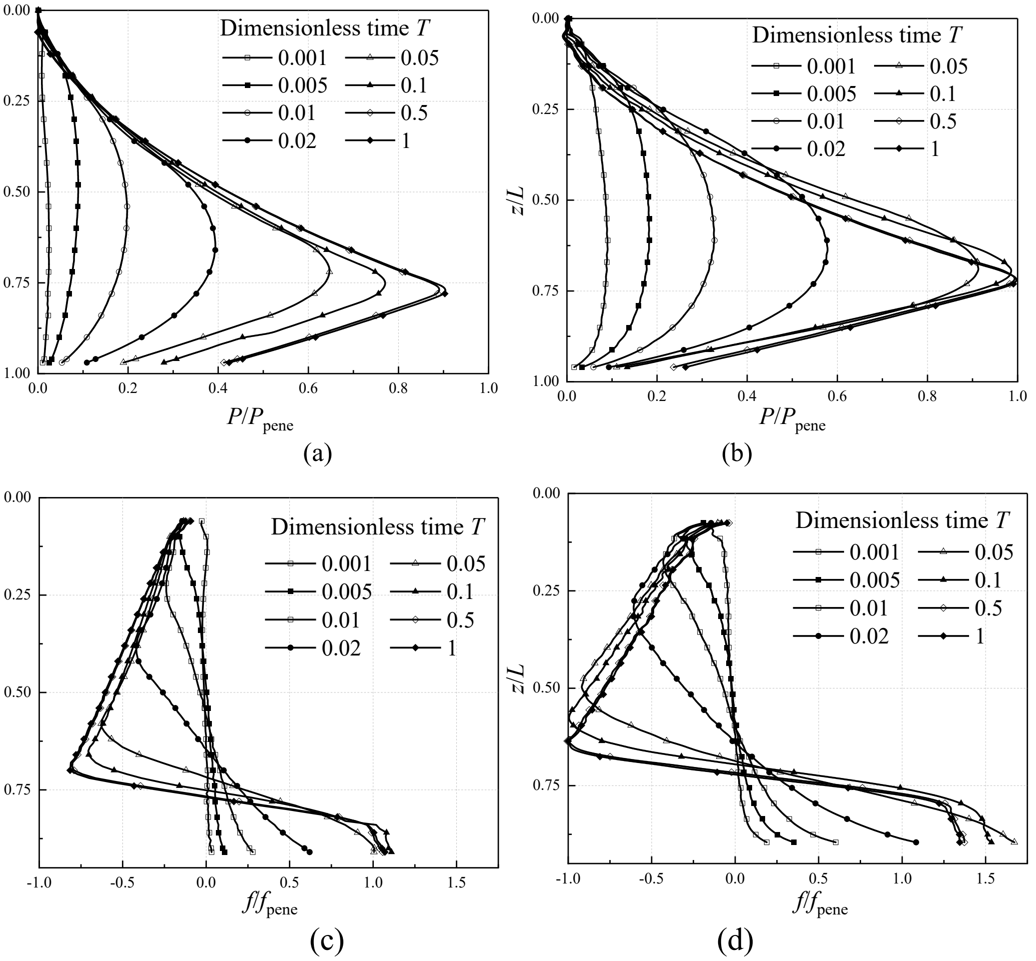

(a) (b)

(c) (d)

Figure 5-17 Distribution of dragload with time: (a) wished-in-place pile case; (b) pile penetration case at 1 m/min rate; and negative skin friction: (c) wished-in-

place pile case; (d) pile penetration case at 1 m/min rate (the negative value of f/f_{pene} represents NSF and the positive value represents PSF)

For comparison, the development of normalized maximum dragload along the pile $P_{\mathrm{max}}/P_{\mathrm{pene}}$ with T is depicted in Figure 5-18. For the wished-in-place pile case, there is an initially stable stage with little increase in dragload, followed by an abrupt increase in P_{max} during the middle stage of consolidation until reaching P_{WIP}. It is also observed that there is a slight increase in P_{max} due to ongoing settlement caused by creep after primary consolidation. For the pile penetration case, there is a steady upward trend, which then sharply increases until approaching 10% degree of primary consolidation. After that, P_{max} reaches a steady value during and after primary consolidation stage. For the higher penetration rate, P_{max} is higher at the commencement of consolidation, but generally remains the same over time. It should be noted that the wished-in-place pile case can underestimate the dragload as well as the NSF throughout the entire consolidation period, showing only 90% of P_{pene} and 70% of f_{pene} at T_{eopc}. This underestimation could be mainly attributed to the neglect of pile penetration, which causes the increase of σ_n', as shown in Figure 5-13.

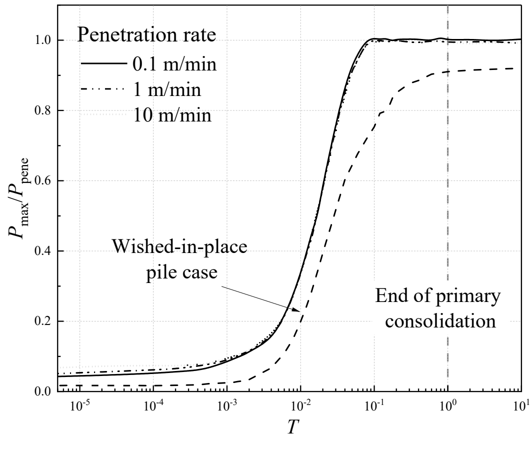

Figure 5-18 Evolution of maximum dragload during consolidation

5.4.4 Empirical model for estimating *β*

In practice, the effective stress related *β* method (Johannessen and Bjerrum 1965, Burland 1973) can be used to calculate the skin friction along the pile as follows:

$$f_s = \beta \sigma_v' \tag{5-16}$$

where f_s is the shaft friction and σ_v' is the effective vertical stress. The dragload at the NP can be calculated based on the following equation:

$$P_{\mathrm{drag,\ NP}} = \pi D \int_0^{L_{NP}} f_s dz \tag{5-17}$$

where L_{NP} and D are the depth of the NP and the pile diameter, respectively. Therefore, the value of *β* during consolidation periods in this study can be back-calculated as shown in Figure 5-19. Similar to the development trend of P_{max}, the *β* value shows a sharp increase before gradually stabilizing, reaching a final value of 0.29 for the pile penetration case and 0.23 for the wished-in-place pile case. For T=0.1, there is a slight decrease in the *β* value for the pile penetration case, which can be attributed to the downward movement of the NP and the fully mobilized NSF under this degree of consolidation.

The reference values for *β*, as obtained from various regional design codes, are also summarized in Figure 5-19. NAVFAC (1986) recommends that the *β* value varies based on the type of soil: 0.2-0.25 for clay, 0.25-0.35 for silt, 0.35-0.5 for sand. CGS (2006) suggests applying a *β* value ranging from 0.2 to 0.3. Hong Kong's foundation code (BD 2017) provides an empirical value of 0.25 in the absence of a more accurate assessment. It can be seen that the constant *β* value provided by these design codes overestimates the dragload at the early stage of consolidation, as also reported by Ng et al. (2008). The β value of the pile penetration at the end of primary consolidation falls within the range specified by NAVFAC, but the other two methods yield the underestimated results. This finding suggests that these methods are both uneconomical and conservative. More importantly, the time-dependent behavior of the β value is ignored in all these design methods.

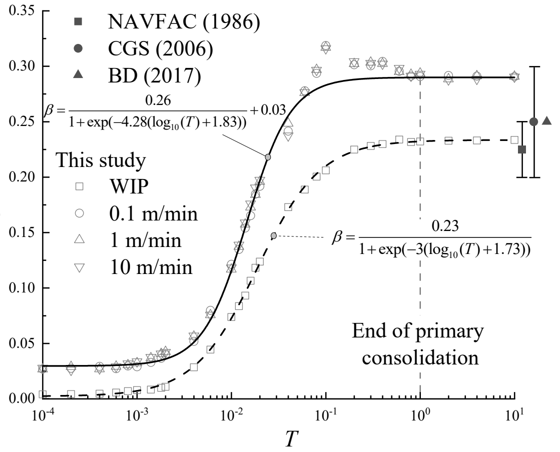

Figure 5-19 Variation in β with consolidation degree with or without pile penetration

To address this issue, an empirical formula involving the time-dependent behavior of β with consolidation is proposed as follows:

$$\beta = \frac{(\beta_{\mathrm{eopc}} - \beta_{\mathrm{ini}})}{1+\exp(-A(\log_{10}(T)+B))} + \beta_{\mathrm{ini}} \tag{5-18}$$

where β_{ini} and β_{eopc} are the β values at the initial stage of consolidation and at the end of primary consolidation, respectively. A and B are the fitting parameters with practical significance as follows. A corresponds to the rate of variation of β, where a higher A results in a faster increase in β. B is related to the time required to reach half the value of $\beta_{\mathrm{ini}} + \beta_{\mathrm{eopc}}$.

Figure 5-19 reveals the fitting results and parameters from the proposed time-dependent β model. This proposed empirical model effectively predicts the development of β values for both the pile penetration and wished-in-place pile cases. The higher value of β_{ini} and β_{eopc} for the pile penetration case indicate an underestimation of β values for wished-in-place pile case, as previously discussed. Additionally, the higher values of A and B suggest a greater variation rate for β and a shorter time required to reach both the half value of $\beta_{\mathrm{ini}} + \beta_{\mathrm{eopc}}$ and β_{eopc} compared to the wished-in-place pile case.

This proposed empirical model can also be applied to other conditions, as shown in Figure 5-20. The data in this figure are derived from previous reports covering various site conditions, as detailed in Table 5-3. The fitting parameters and correlation coefficient R^2 are also listed in Table 5-3, indicating that the proposed empirical model reliably captures the development of β over time. The predicted β_{eopc} ranges from approximately 0.28 to 0.3, which aligns with the recommended value by NAVFAC (1986), except for a value of 0.18 observed with the bitumen-coated pile. β_{ini} can be estimated with various pile installation methods. Higher values of parameter A are observed in the studies from Leung et al. (2004) and Ng et al. (2008). This phenomenon may be attributed to optimal drainage conditions, where double drainage boundaries are implemented, and only a single layer of high permeable clay is utilized. Additionally, comparable B values are observed in the studies by Leung et al. (1991), Indraratna et al. (1992) as well as in the numerical simulations conducted in this study, within their respective sub-group test. These separate tests, performed in the same field but on different piles, indicate that this parameter is site-specific. Generally, these fitting parameters are influenced by site conditions, including surcharge load, pile head loading, consolidation properties, end bearing layer characteristics, creep effects, pile size, and pile-soil interface friction and pile installation method. Furthermore, site conditions vary between different projects.

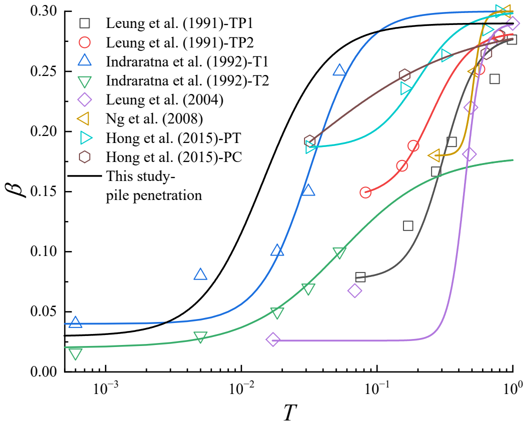

Figure 5-20 Applicability of the adopted empirical model to other engineering conditions

However, the broad applicability of this empirical model is limited due to the scarcity of relevant datasets, especially those spanning multiple years of monitoring. Nevertheless, this empirical model provides a framework for incorporating the time-dependency of β in the design method. Initially, an appropriate β_{eopc} value is determined based on the soil type on site. Subsequently, the parameters A and B can be established according to site conditions. Finally, β_{ini} can be estimated based on the pile installation method. Further experimental work is needed to correlate A and B with in situ conditions, which will be the next step for the authors.

Table 5-3 Applicability of the adopted empirical model

Data source	Fitting parameter					Field condition			
	β_{Eopc}	β_{ini}	A	B	R^2	Pile	Soil	Surcharge (kPa)	Note

This study	0.29	0.03	4.28	1.83	0.99	PHC pile	Soft clay	20	Pile penetration simulation
This study	0.23	0	3	1.73	0.99	PHC pile	Soft clay	20	Wished-in-place pile simulation
Leung et al. (1991)-TP1	0.28	0.077	8	0.51	0.95	Driven PHC pile	Grey soft marine clay to sandy clay	-	-
Leung et al. (1991)-TP2	0.283	0.145	7	0.6	0.96	Driven PHC pile	Grey soft marine clay to sandy clay	-	-
Indraratna et al. (1992)-T1	0.3	0.04	5.3	1.49	0.93	Driven PHC pile	Soft clay	34	-
Indraratna et al. (1992)-T2	0.18	0.02	2.92	1.27	0.99	Driven PHC pile	Soft clay	34	Bitumen coated
Leung et al. (2004)	0.29	0.026	15.98	0.35	0.96	Jacked aluminum tube pile	Kaolin clay to sand	70	Centrifuge test
Ng et al. (2008)	0.3	0.18	28.34	0.29	0.99	Bored aluminum tube pile	Speswhite China clay	45	Centrifuge test
Hong et al. (2015)-PT	0.3	0.186	6	0.7	0.96	Bored pile	Soft clay to clayey gravel	40	-
Hong et al. (2015)-PC	0.29	0.09	1.78	1.51	0.98	Bored pile	Soft clay to clayey gravel	40	-

5.5 Summary

In this chapter, a 2D axisymmetric novel hydro-mechanical coupled SNS-PFEM framework has been developed to investigate the effect of pile penetration on the development of NSF during consolidation. An elasto-viscoplastic model with an enhanced time integration algorithm was applied in this framework. The numerical model was initially developed to simulate a field-observed case for verification. Soil stress evolution and NSF generation were examined at various penetration rates. The detailed findings and conclusions are as follows:

(1) Numerically analyzing NSF while neglecting the pile installation process, as in the case of the wished-in-place pile, can unsafely result in a 10% underestimation of the dragload magnitude compared to scenarios that account for pile penetration. This underestimation is mainly attributed to the increase in effective normal stress acting on

the pile during penetration, as the soil near the pile is compressed to accommodate the pile volume.

(2) Higher penetration rates lead to increased values of p' and q, along with a reduced magnitude of excess porewater pressure in the soil along the pile at the end of installation. The penetration rate primarily affects the NSF and dragload primarily during the initial stage of consolidation. As consolidation progresses, NSF and dragload equalize to nearly the same magnitude across different penetration rates.

(3) The β value recommended by certain technical design methods fails to accurately reflect its true magnitude or account for its time dependency. Therefore, a new empirical formula for time-dependent β value with four controlling parameters related to the field cases is proposed and has been successfully applied to other field cases.

CHAPTER 6 CONCLUSIONS AND FUTURE WORK

6.1 Conclusions

In this dissertation, preliminary investigations are conducted to identify the creep effect on the NSF and NP development and to improve the existing design methods. An elasto-viscoplastic model with an enhanced time integration algorithm is successfully implemented into the finite element package ABAQUS. The 2D axisymmetric model for a single pile and 3D quarter model for a pile group are developed and validated through model tests. Additionally, a novel stable node-based smoothed particle finite element method (SNS-PFEM) framework is introduced to investigate the pile penetration effect on NSF development. The key contributions and conclusions of this dissertation are summarized as follows:

6.1.1 Creep effect on NSF development on single pile

(1) Soft soil creep significantly influents NSF development, leading to higher dragload as well as an increased β value. This effect arises because greater soil settlement increases the relative displacement between the soil and pile, further mobilizing the NSF.

(2) The increased creep coefficient can generate additional excess porewater pressure, extending the time needed for primary consolidation. Furthermore, this excess porewater pressure may delay dragload development due to the reduction of the effective stress at the pile-soil interface.

(3) The NP position shows a sharp initial decrease during consolidation before stabilizing. A higher creep effect induces greater downward movement of the NP and reduces the time required for stabilization. Furthermore, the existing empirical formula neither predicts the NP position well nor accounts for its time dependency. A time-dependent exponential model is presented and applied to predict the variation of NP position.

6.1.2 Creep effect on group effect

(1) The shielding piles can be designed to reduce the dragload, a phenomenon known as the group effect. The group effect is prominent with small pile spacings but diminishes as the end-bearing layer stiffness increases. The creep effect can significantly influence the group effect, which becomes less significant under high creep conditions.

(2) The results of the parametric studies indicate that when the pile spacing is beyond 7 times the diameter of the sacrificial piles, the group effect can be neglected. However, for end-bearing piles and sites with high creep potential, this critical pile spacing should be reduced.

(3) Compared to the α method, the β method better aligns with engineering conditions and can be adopted to estimate the dragload on pile. The value of β is 0.21 for a single pile and ranges from 0.16 to 0.20 for the center pile within a group. Furthermore, the β values are observed to increase with pile spacing and are not sensitive to variations in end-bearing layer stiffness.

(4) The lower effective stress of soil is observed within a pile group compared to outside the group, which is identified as the primary cause of the NSF pile group effect.

However, this unbalanced stress can generate additional bending moments along the shafts, posing significant concerns for piles designed exclusively for axial loads.

6.1.3 Pile penetration effect on NSF development

(1) Numerical analysis of NSF while neglecting the pile installation process, as in the case of the wished-in-place pile, can underestimate the dragload magnitude compared to scenarios that account for pile penetration. This discrepancy occurs due to the adjacent soil experiences severe distortion and is subjected to large normal stress and shear stress during pile penetration.

(2) Higher penetration rate results in a lower magnitude of excess porewater pressure as well as increased mean effective stress and deviatoric stress. The pile penetration rate influences dragload during the initial stage of consolidation, while has no influence after full consolidation of soil

(3) A new empirical formula for time-dependent β value is proposed to address the limitations of recent technical design methods, which fail to accurately reflect its true magnitude or account for its time dependency. The proposed empirical method has been successfully applied to field data, demonstrating its engineering applicability.

6.2 Suggestion for future research

Due to limitations in existing research strategies and processes, certain aspects are not addressed in this dissertation. Recommendations for future work are as follows:

(1) While empirical methods for the time-dependent β value and NP position have been proposed, the fitting parameters in these empirical methods are dependent on the field conditions, including soil properties (e.g., consolidation coefficient, creep

coefficient, thickness of the compressible layer), pile conditions (e.g., pile geometry, installation method) and external loading (e.g., pile head loading, surcharge loading). Further numerical analysis, considering multiple influencing factors, is required to obtain extensive data for correlating the fitting parameters with in-situ conditions.

(2) In addition to the pile toe located at the top of the clay or the sand layer, other conditions should also be considered, such as pile toe founded on or within a rock socket (especially the widely used rock-socketed piles in Hong Kong). Furthermore, a micromechanical rock–pile interface model has been proposed and successfully implemented into the FEM by the author (Liang et al. 2024). Further research dedicated to rock-socketed piles subjected to NSF would be valuable for accurately evaluating the axial bearing capacity of these piles, as illustrated in Figure 6-1.

(3) The 2D large deformation FE framework needs to be further extended to 3D to investigate the pile installation effect on pile group NSF development. The pile installation sequence and time intervals between piles may influence soft soil consolidation, effective stress distribution as well as the dragload development.

(4) There remains a considerable lack of field studies examining NSF on pile groups due to the prohibitively high costs and complexity involved. To further investigate the group effect on dragload, future field tests or centrifuge tests on pile groups should measure variations in pore pressures, effective stresses in the vicinity of the pile group and mobilized dragload, comparing them to those observed for a single pile at the same site.

(5) It is noteworthy that except for the adoption of the classic β method to evaluate the NSF, the piezocone penetration test (CPTu) with its advantages of simplicity, fast

and relative cost-effectiveness has the potential to estimate the NSF development. The CPTu provides continuous measurements of cone tip resistance (q_c), sleeve friction (f_s) and penetration pore pressure (u) with penetration depth, allowing empirical methods to be developed that correlate these field measured values with NSF magnitude. Further field tests are needed in the future to address this research gap.

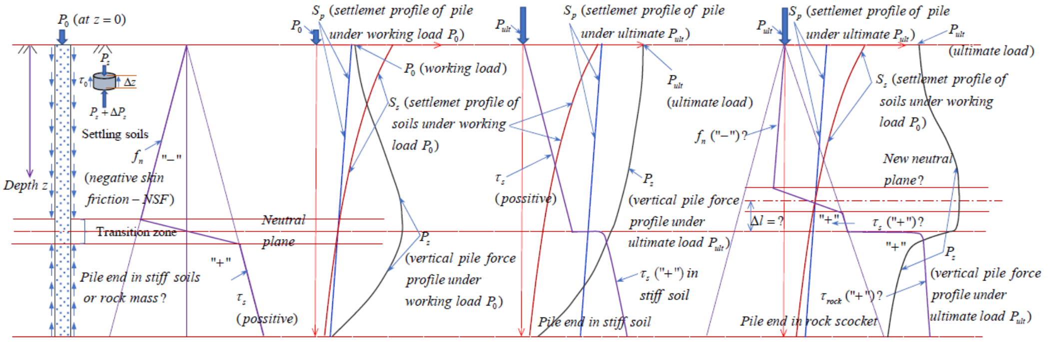

(a) Pile subject to NSF

(b) Distribution of shaft resistance

(c) Settlement profiles of pile (S_p) and soils (S_s) and vertical force profile of pile (P_z) under P_0

(d) NSF is reversed from "−" to "+" ($f_n \Rightarrow \tau_s$) if $S_p > S_s$ and P_z (profile) under P_{ult}

(e) NSF is partially reduced and reversed from "−" to "+", if $S_p > S_s$, τ_{rock} in rock scocket, and P_z (profile) under P_{ult}

Figure 6-1 Development of NSF on a pile all in soils or through soils into a rock socket

REFERENCES

Abu-Farsakh, M., Rosti, F., and Souri, A. 2015. Evaluating pile installation and subsequent thixotropic and consolidation effects on setup by numerical simulation for full-scale pile load tests. Canadian Geotechnical Journal, **52**(11): 1734–1746. doi:10.1139/cgj-2014-0470.

AIJ (Architectural Institute of Japan). 2001. Recommendations for designing of building foundations. [In Japanese.].

Alonso, E.E., Josa, A., and Ledesma, A. 1984. Negative skin friction on piles: a simplified analysis and prediction procedure. Géotechnique, **34**(3): 341–357.

Baligh, M.M. 1985. Strain Path Method. Journal of Geotechnical Engineering, **111**(9): 1108–1136. doi:10.1061/(ASCE)0733-9410(1985)111:9(1108).

Basu, P., Prezzi, M., Salgado, R., and Chakraborty, T. 2014. Shaft Resistance and Setup Factors for Piles Jacked in Clay. Journal of Geotechnical and Geoenvironmental Engineering, **140**(3): 04013026. doi:10.1061/(ASCE)GT.1943-5606.0001018.

BD (Buildings Department Technical Committee of Hong Kong). 2017. Code of practice for foundations 2017 of Hong Kong.

Bjerin, L. 1977. Dragloads on long concrete piles. Swedish Geotechnical Institute Report, **2**: 62.

Bjerrum, L., Johannessen, I.J., and Eide, O. 1969. Reduction of negative skin friction on steel piles to rock.

Bond, A.J., and Jardine, R.J. 1991. Effects of installing displacement piles in a high OCR clay. Géotechnique, **41**(3): 341–363. doi:10.1680/geot.1991.41.3.341.

Bowles, J.E. 1997. Foundation analysis and design.

Bozozuk, M. 1981. Bearing capacity of pile preloaded by downdrag.

Briaud, J.-L. 1997. Bitumen Selection for Reduction of Downdrag on Piles. Journal of Geotechnical and Geoenvironmental Engineering, **123**(12): 1127–1134. doi:10.1061/(ASCE)1090-0241(1997)123:12(1127).

Burland, J. 1973. Shaft friction of piles in clay--a simple fundamental approach. **6**(3): 30–38.

Canadian Geotechnical Society. 2006. Canadian Foundation Engineering Manual (Fourth edition).

Cao, J., Audibert, J.M.E., Al-Khafaji, Z., Phillips, R., and Popescu, R. 2002. Penetration resistance of suction caissons in clay. *In* ISOPE International Ocean and Polar Engineering Conference.

Cao, W.-P., Chen, Y.-M., and Wolfe, W.E. 2014. New load transfer hyperbolic model for pile-soil interface and negative skin friction on single piles embedded in soft soils. International Journal of Geomechanics, **14**(1): 92–100.

Casagrande, A. 1936. The determination of the preconsolidation load and its practical significance.

de Chaunac, H., and Holeyman, A. 2018. Numerical analysis of the set-up around the shaft of a closed-ended pile driven in clay. Géotechnique, **68**(4): 332–344. doi:10.1680/jgeot.16.P.229.

Chen, R.P., Zhou, W.H., and Chen, Y.M. 2009. Influences of soil consolidation and pile load on the development of negative skin friction of a pile. Computers and Geotechnics, **36**(8): 1265–1271.

Chen, Z.-J., Feng, W.-Q., and Yin, J.-H. 2021. A new simplified method for calculating short-term and long-term consolidation settlements of multi-layered soils considering creep limit. Computers and Geotechnics, **138**: 104324.

Chiou, J.S., and Wei, W.T. 2021. Numerical investigation of pile-head load effects on the negative skin friction development of a single pile in consolidating ground. Acta Geotechnica, **16**(6): 1867–1878.

Chow, S.H., O'loughlin, C.D., and Randolph, M.F. 2014. Soil strength estimation and pore pressure dissipation for free-fall piezocone in soft clay. Géotechnique, **64**(10): 817–827. doi:10.1680/geot.14.P.107.

Chow, Y.K., Chin, J.T., and Lee, S.L. 1990. Negative skin friction on pile groups. International Journal for Numerical and Analytical Methods in Geomechanics, **14**(2): 75–91. doi:10.1002/nag.1610140202.

Clemente, F.M. 1981. Downdrag on bitumen coated piles in a warm climate. *In* Proceedings of the 10th international conference on soil mechanics and foundation engineering, Stockholm.

Comodromos, E.M., and Bareka, S.V. 2005. Evaluation of negative skin friction effects in pile foundations using 3D nonlinear analysis. Computers and Geotechnics, **32**(3): 210–221.

Dassault Systèmes. 2020. ABAQUS analysis user's manual version 2020.

Davisson, M.T. 1993. Negative skin friction in piles and design decisions.

Endo, M.A., Minou, A., Kawasaki, I., and Shibata, T. 1969. Negative skin friction acting on steel piles in clay.

Ergun, M.U., and Sönmez, D. 1995. Negative skin friction from surface settlement measurements in model group tests. Canadian Geotechnical Journal, **32**(6): 1075–1079. doi:10.1139/t95-105.

Fang, H.-C., Yin, Z.-Y., Peng, M.-Z., and Zhang, D.-L. 2023. Improved SNS-PFEM framework with dual mortar method to model geotechnical large deformation contact problems. Computer Methods in Applied Mechanics and Engineering, **412**: 116091. doi:10.1016/j.cma.2023.116091.

Fang, H.-C., Yin, Z.-Y., Zhang, D.-L., and Cao, L.-Q. 2024a. A hydro-mechanical coupled contact method for two-phase geotechnical large deformation problems within the SNS-PFEM framework. Computer Methods in Applied Mechanics and Engineering, **420**: 116743. doi:10.1016/j.cma.2023.116743.

Fang, H.-C., Yin, Z.-Y., Zhang, D.-L., and Fang, Q. 2024b. Unified framework for geotechnical cross-contact problems with interfacial fluid flow. International Journal of Mechanical Sciences, **269**: 109047. doi:10.1016/j.ijmecsci.2024.109047.

Fang, H.-C., Zhang, D.-L., Fang, Q., Cao, L.-Q., and Wen, M. 2022. An efficient patch-to-patch method for coupling independent finite element subdomains with intersecting interfaces. Computer Methods in Applied Mechanics and Engineering, **388**: 114209. doi:10.1016/j.cma.2021.114209.

Fellenius, B.H. 1972. Down-drag on piles in clay due to negative skin friction. CANADIAN GEOTECHNICAL JOURNAL, **9**(4): 323–337. doi:10.1139/t72-037.

Fellenius, B.H. 1989. Unified design of piles and pile groups. Transportation Research Record, **1169**: 75–82.

Fellenius, B.H. 1998. Recent advances in the design of piles for axial loads, dragloads, downdrag, and settlement. *In* Proceedings of a Seminar by American Society of Civil Engineers, ASCE, and Port of New York and New Jersey.

Fellenius, B.H. 2006. Results from long-term measurement in piles of drag load and downdrag. Canadian Geotechnical Journal, **43**(4): 409–430. doi:10.1139/t06-009.

Feng, W.-Q. 2016. Experimental study and constitutive modelling of the time-dependent stress-strain behavior of soils.

GEOTECHNICAL ENGINEERING OFFICE Civil Engineering and Development Department The Government of the Hong Kong. 2006. Foundation Design and Construction in Hong Kong.

Gibson, R.E., Knight, K., and Taylor, P. 1963. A critical experiments to examine theories of three-dimensional consolidation.

Hansbo, S. 1994. Foundation engineering.

HKIE. 2017. Code of practice for foundations.

Ho, K.K.S., and Mak, S.H. 1994. Long-term monitoring of negative skin friction in driven piles in reclaimed land. *In* Proceedings of the Fifth International Conference on Piling and Deep Foundations.

Hong, Y., Ng, C.W.W., Chen, Y.M., Wang, L.Z., and Chan, V.S.Y. 2015. Field study of downdrag and dragload of bored piles in consolidating ground. J Perform Constructed Facil, **4015050**.

Horpibulsuk, S., Shibuya, S., Fuenkajorn, K., and Katkan, W. 2007. Assessment of engineering properties of Bangkok clay. CANADIAN GEOTECHNICAL JOURNAL, **44**(2): 173–187.

Hu, Y., and Randolph, M.F. 1998. A practical numerical approach for large deformation problems in soil. International Journal for Numerical and Analytical Methods in Geomechanics, **22**(5): 327–350. doi:10.1002/(SICI)1096-9853(199805)22:5<327::AID-NAG920>3.0.CO;2-X.

Indraratna, B., Balasubramaniam, A.S., Phamvan, P., and Wong, Y.K. 1992. Development of negative skin friction on driven piles in soft Bangkok clay. CANADIAN GEOTECHNICAL JOURNAL, **29**(3): 393–404. doi:10.1139/t92-044.

Inoue, Y. 1977. Settlement of building due to pile downdrag. Proc. 9th ICSMFE, Tokyo, Japan, 1977, **1**: 561–564.

Jacob, F., and Kenneth, L.C. 1996. Construction Failure.

Jeong, S., Lee, J., and Lee, C.J. 2004. Slip effect at the pile–soil interface on dragload. Computers and Geotechnics, **31**(2): 115–126.

Jiang, L., and Lin, H. 2010. Integrated analysis of SAR interferometric and geological data for investigating long-term reclamation settlement of Chek Lap Kok Airport, Hong Kong. Engineering Geology, **110**(3–4): 77–92.

Jin, Y.-F., Yin, Z.-Y., Zhou, W.-H., Yin, J.-H., and Shao, J.-F. 2019. A single-objective EPR based model for creep index of soft clays considering L2 regularization. Engineering Geology, **248**: 242–255. doi:10.1016/j.enggeo.2018.12.006.

Jin, Y.-F., Yin, Z.-Y., Zhou, X.-W., and Liu, F.-T. 2021. A stable node-based smoothed PFEM for solving geotechnical large deformation 2D problems. Computer Methods in Applied Mechanics and Engineering, **387**: 114179. doi:10.1016/j.cma.2021.114179.

Johannessen, I.J., and Bjerrum, L. 1965. Measurement of the compression of a steel pile to rock due to settlement of the surrounding clay.

Katona, M.G. 1984. Evaluation of viscoplastic cap model. Journal of Geotechnical Engineering, **110**(8): 1106–1125.

Keenan, G.H., and Bozozuk, M. 1985. Downdrag on a three-pile group of pipe piles. *In* International conference on soil mechanics and foundation engineering. 11.

Koerner, R.M., and Mukhopadhyay, C. 1972. Behavior of negative skin friction on model piles in medium plasticity silt. Highway Research Record, **405**: 34–44.

Kog, Y.C. 1987. A case study of downdrag and axial load on timber piles in layered soil. *In* Proc. 5th International Geotechnical Seminar on Case Histories in Soft Clay, 1987.

Kog, Y.C. 1990. Downdrag and axial load on piles. Ground Engineering, **23**(3).

Lam, S.Y., Ng, C.W., Leung, C.F., and Chan, S.H. 2009. Centrifuge and numerical modeling of axial load effects on piles in consolidating ground. CANADIAN GEOTECHNICAL JOURNAL, **46**(1): 10–24.

Lam, S.Y., Ng, C.W.W., and Poulos, H.G. 2013. Shielding Piles from Downdrag in Consolidating Ground. Journal of Geotechnical and Geoenvironmental Engineering, **139**(6): 956–968. doi:10.1061/(asce)gt.1943-5606.0000764.

Lee, C.-J. 2001. The influence of negative skin friction on piles and in pile groups.

Lee, C.J., Bolton, M.D., and Al-Tabbaa, A. 2002. Numerical modelling of group effects on the distribution of dragloads in pile foundations. Géotechnique, **52**(5): 325–335. doi:10.1680/geot.2002.52.5.325.

Lee, C.-J., and Chen, C.R. 2003. Negative Skin Friction on Piles Due to Lowering of Groundwater Table. Journal of the Southeast Asian Geotechnical Society, **34**.

Lee, C.J., Chen, H.T., and Wang, W.H. 1998. Negative skin friction on a pile due to excessive groundwater withdrawal. *In* Proc. Centrifuge 98. eds. Kimura, Kusakabe & Takemura.

Lee, C.J., and Ng, C.W.W. 2004. Development of Downdrag on Piles and Pile Groups in Consolidating Soil. Journal of Geotechnical and Geoenvironmental Engineering, **130**(9): 905–914. doi:10.1061/(ASCE)1090-0241(2004)130:9(905).

Leung, C.F., Liao, B.K., Chow, Y.K., Shen, R.F., and Kog, Y.C. 2004. Behavior of Pile Subject to Negative Skin Friction and Axial Load. Soils and Foundations, **44**(6): 17–26. doi:10.3208/sandf.44.6_17.

Leung, C.F., Radhakrishnan, R., and Tan, S.-A. 1991. Performance of precast driven piles in marine clay. J. Geotech. Eng., **117**(4): 637–657.

Liang, R., Yin, Z.-Y., Yin, J.-H., and Wu, P.-C. 2023. Numerical analysis of time-dependent negative skin friction on pile in soft soils. Computers and Geotechnics, **155**: 105218. doi:10.1016/j.compgeo.2022.105218.

Liang, R., Yin, Z.-Y., Yin, J.-H., Wu, P.-C., and Chen, Z.-J. 2024. An enhanced micromechanical rock–pile interface model with application to rock-socketed pile modeling. International Journal for Numerical and Analytical Methods in Geomechanics, **48**(11): 2971–2995. doi:10.1002/nag.3759.

Liang, R., Yuan, Y., Fu, D.-F., and Liu, R. 2021. Cyclic response of monopile-supported offshore wind turbines under wind and wave loading in sand. Marine Georesources & Geotechnology, **39**(10): 1230–1243. doi:10.1080/1064119X.2020.1821848.

Little, J.A. 1994. Downdrag on piles: review and recent experimentation. *In* Vertical and Horizontal Deformations of Foundations and Embankments.

Liu, J.-Y., Gao, H.-M., and Liu, H.-L. 2012. Finite element analyses of negative skin friction on a single pile. Acta Geotechnica, **7**(3): 239–252.

Milner, R.P. 1957. Discussion on foundation of structures. *In* Proceeding 4th ICSMFE, Session 6.

Ministry of Housing and Urban-Rural Development of the People’s Republic of China. 2008. Technical code for building pile foundations. [In Chinese.].

Monforte, L., Arroyo, M., Carbonell, J.M., and Gens, A. 2017. Numerical simulation of undrained insertion problems in geotechnical engineering with the Particle Finite Element Method (PFEM). Computers and Geotechnics, **82**: 144–156. doi:10.1016/j.compgeo.2016.08.013.

NAVFAC. 1986. FOUNDATIONS AND EARTH STRUCTURES.

Nazem, M., Sheng, D., and Carter, J.P. 2006. Stress integration and mesh refinement for large deformation in geomechanics. International Journal for Numerical Methods in Engineering, **65**(7): 1002–1027. doi:10.1002/nme.1470.

Ng, C.W., Poulos, H.G., Chan, V.S., Lam, S.S., and Chan, G.C. 2008. Effects of tip location and shielding on piles in consolidating ground. Journal of Geotechnical and Geoenvironmental Engineering, **134**(9): 1245–1260. doi:10.1061/(ASCE)1090-0241(2008)134:9(1245).

Okabe, T. 1977. Large negative friction and friction-free pile methods. Proc. 9th Int. Conf. on SMFE., **1**: 679–682.

Poulos, H.G. 1997. Piles subjected to negative friction: A procedure for design. Geotechnical Engineering, **28**: 23–44.

Premchitt, J., Gray, I., and Ho, K.K.S. 1994. Skin Friction on Piles at the New Public Works Central Laboratory.

Randolph, M.F. 2003. Science and empiricism in pile foundation design. Géotechnique, **53**(10): 847–875. doi:10.1680/geot.2003.53.10.847.

Randolph, M.F., Carter, J.P., and Wroth, C.P. 1979. Driven piles in clay—the effects of installation and subsequent consolidation. Géotechnique, **29**(4): 361–393. doi:10.1680/geot.1979.29.4.361.

Roy, M., Blanchet, R., Tavenas, F., and Rochelle, P.L. 1981. Behaviour of a sensitive clay during pile driving. Canadian Geotechnical Journal, **18**(1): 67–85. doi:10.1139/t81-007.

Sagaseta, C., Whittle, A.J., and Santagata, M. 1997. Deformation analysis of shallow penetration in clay. International Journal for Numerical and Analytical Methods in Geomechanics, **21**(10): 687–719. doi:10.1002/(SICI)1096-9853(199710)21:10<687::AID-NAG897>3.0.CO;2-3.

Shen, R. 2008. Negative skin friction on single piles and pile groups.

Shibata, T., Sekiguchi, H., and Yukitomo, H. 1982. Model test and analysis of negative friction acting on piles. Soils and Foundations, **22**(2): 29–39. doi:https://doi.org/10.3208/sandf1972.22.2_29.

Sloan, S.W. 1987. Substepping schemes for the numerical integration of elastoplastic stress–strain relations. International Journal for Numerical Methods in Engineering, **24**(5): 893–911. doi:10.1002/nme.1620240505.

Su, D., Gao, Z., Yan, W., and Pang, X. 2020. A Systematic Experimental Study on the Group Effect of Dragloads in Pile Foundations. KSCE Journal of Civil Engineering, **24**(7): 2038–2048. doi:10.1007/s12205-020-1459-2.

Sun, T.K., Yan, W.M., and Su, D. 2015. Fully coupled consolidation analysis of shear strength mobilization and dragload of a pile subject to negative skin friction. International Journal of Geomechanics, **15**(3): 04014057.

Terzaghi, K., and Peck, R.B. 1948. SOIL MECHANICS IN ENGINEERING PRACTICE: SCOUR AND SCOUR PREVENTION AT BOUNDARIES.

Thomas, J., Fahey, M., and Jewell, R. 1998. Pile down-drag due to surface loading. *In* Pile down-drag due to surface loading.

Walker, L.K. 1973. Dragdown on coated and uncoated piles. *In* Proc. 8th International Conference on Soil Mechanics and Foundation Engineering, ICSMFE.

Wang, D., Bienen, B., Nazem, M., Tian, Y.H., Zheng, J.B., Pucker, T., and Randolph, M.F. 2015. Large deformation finite element analyses in geotechnical engineering. Computers and Geotechnics, **65**: 104–114. doi:10.1016/j.compgeo.2014.12.005.

Wang, Z.-Y., Jin, Y.-F., Yin, Z.-Y., and Wang, Y.-Z. 2022. A novel coupled NS-PFEM with stable nodal integration and polynomial pressure projection for geotechnical problems. International Journal for Numerical and Analytical Methods in Geomechanics, **46**(13): 2535–2560. doi:10.1002/nag.3417.

Whittle, A.J., and Sutabutr, T. 1999. Prediction of Pile Setup in Clay. Transportation Research Record: Journal of the Transportation Research Board, **1663**(1): 33–40. doi:10.3141/1663-05.

Wu, P.-C., Feng, W.-Q., and Yin, J.-H. 2020. Numerical study of creep effects on settlements and load transfer mechanisms of soft soil improved by deep cement mixed soil columns under embankment load. Geotextiles and Geomembranes, **48**(3): 331–348. doi:https://doi.org/10.1016/j.geotexmem.2019.12.005.

Yan, W.M., Sun, T.K., and Tham, L.G. 2012. Coupled-consolidation modeling of a pile in consolidating ground. Journal of Geotechnical and Geoenvironmental Engineering, **138**(7): 789–798. doi:10.1061/(ASCE)GT.1943-5606.0000651.

Yen, T.-L., Lin, H., Chin, C.-T., and Wang, R.F. 1989. Interpretation of instrumented driven steel pipe piles. *In* Foundation engineering: Current principles and practices.

Yin, J.-H., and Graham, J. 1994. Equivalent times and one-dimensional elastic viscoplastic modelling of time-dependent stress–strain behaviour of clays. CANADIAN GEOTECHNICAL JOURNAL, **31**(1): 42–52.

Yin, J.-H., Graham, J., Clark, J.I., and Gao, L. 1994. Modelling unanticipated pore-water pressures in soft clays. CANADIAN GEOTECHNICAL JOURNAL, **31**(5): 773–778.

Yin, J.-H., and Zhu, J.-G. 1999. Elastic viscoplastic consolidation modelling and interpretation of pore-water pressure responses in clay underneath Tarsiut Island. CANADIAN GEOTECHNICAL JOURNAL, **36**(4): 708–717.

Yin, Z.-Y., Karstunen, M., Chang, C.S., Koskinen, M., and Lojander, M. 2011. Modeling time-dependent behavior of soft sensitive clay. Journal of Geotechnical and Geoenvironmental Engineering, **137**(11): 1103–1113.

Yin, Z.-Y., Li, J., Jin, Y.-F., and Liu, F.-Y. 2019. Estimation of robustness of time integration algorithms for elasto-viscoplastic modeling of soils. International Journal of Geomechanics, **19**(2): 04018197.

Yu, H.-S. 2000. Cavity Expansion Methods in Geomechanics.

Zeevaert, L. 1959. Reduction of point bearing capacity of piles because of negative friction. *In* Proceedings of the First Pan-American Conference on Soil Mechanics and Foundation Engineering.

Zeevaert, L. 1972. Foundation engineering for difficult subsoil conditions.

Zhang, X.-W., Liu, X.-Y., Chang, Z.-X., Liu, Z.-H., Yu, D.-M., and Li, Y. 2022. Time Dependence of Neutral Plane Position in a PHC-Supported Soft Subgrade. Journal of Geotechnical and Geoenvironmental Engineering, **148**(2): 05021016.

Zhao, Z.-F., Ye, S.-H., Zhu, Y.-P., Tao, H., and Chen, C.-L. 2022. Scale model test study on negative skin friction of piles considering the collapsibility of loess. Acta Geotechnica, **17**(2): 601–611.

Zhu, J.-G., and Yin, J.-H. 2001. Deformation and Pore-Water Pressure Responses of Elastic Viscoplastic Soil. Journal of Engineering Mechanics, **127**(9): 899–908. doi:10.1061/(ASCE)0733-9399(2001)127:9(899).